SENSITIVITY ANALYSIS AND TOPOLOGY OPTIMIZATION IN PLASMONICS

by

Zhou Zeng

A Thesis

Submitted to the Faculty of Purdue University

In Partial Fulfillment of the Requirements for the degree of

Master of Science in Mechanical Engineering

School of Mechanical Engineering

West Lafayette, Indiana

August 2019

THE PURDUE UNIVERSITY GRADUATE SCHOOL
STATEMENT OF COMMITTEE APPROVAL

Dr. Xianfan Xu, Chair
School of Mechanical Engineering

Dr. Liang Pan
School of Mechanical Engineering

Dr. Alexander Kildishev
School of Computer & Electrical Engineering

Approved by:

Dr. Jay P. Gore
Head of the Graduate Program

To my family and friends.

ACKNOWLEDGMENTS

This work cannot be done without the support of many people. First of all, I would like to express my sincere gratitude to my advisor, Prof. Xianfan Xu, for his patience and guidance throughout my research career. The many risky choices I have made put me through lots of difficult times, but also led me to this accomplishment today. I could not have survived these hardships without the encouragement and understanding from Prof. Xu. I am also grateful to Prof. Pan and Prof. Jiao for serving on my advisory committee. I owe special thanks to Prof. Kildishev for agreeing to serve on my exam committee in the last minute.

I have greatly enjoyed the working environment at Birck Nanotechnology center. I would like to thank Anurup for his help and teachings in the NSOM experiments. Shouyuan has been a mentor-like friend who guides me to explore the world of research. I have been enjoying having civil discourse with him and am very grateful for his help on both professional and personal levels. I want to thank Prabhu for his patience in listening to my disorganized lecturing. I thank Emroz for giving me valuable advice on my defense presentation and other stuff. I thank Mauricio for showing great interests in my research. I also want to thank Paul for his occasional witty comments. They really lighten up the mood. I want to give my sincere appreciation to other group members: Vasu, Hakan and Akanksha.

Finally, I would like to thank my parents, for their unconditional love, support and encouragement all the time. There are of course many others to list, friends, roommates, collogues. Thanks to you all!

TABLE OF CONTENTS

LIST OF TABLES

LIST OF FIGURES

ABSTRACT

Author: Zeng, Zhou. MS
Institution: Purdue University
Degree Received: August 2019
Title: Sensitivity Analysis and Topology Optimization in Plasmonics.
Committee Chair: Xianfan Xu

The rapid development of topology optimization in photonics has greatly expanded the number of photonic structures with extraordinary performance. The optimization is usually solved by using a gradient-based optimization algorithm, where gradients are evaluated by the adjoint sensitivity analysis. While the adjoint sensitivity analysis has been demonstrated to provide reliable gradients for designs of dielectrics, there has not been too much success in plasmonics. The difficulty of obtaining accurate field solutions near sharp edges and corners in plasmonic structures, and the strong field enhancement jointly increase the numerical error of gradients, leading to failure of convergence for any gradient-based algorithm.

We present a new method of calculating accurate sensitivity with the FDTD method by direct differentiation of the time-marching system in frequency domain. This new method supports general frequency-domain objective functions, does not relay on implementation details of the FDTD method, works with general isotropic materials and can be easily incorporated into both level-set-based and density-based topology optimizations. The method is demonstrated to have superior accuracy compared to the traditional continuous sensitivity. Next, we present a framework to carry out density-based topology optimization using our new sensitivity formula. We use the non-linear material interpolation to counter the rough landscape of plasmonics, adopt the filtering-and-projection regularization to ensure manufacturability and perform the optimization with a continuation scheme to improve convergence.

We give two examples involving reconstruction of near fields of plasmonic structures to illustrate the robustness of the sensitivity formula and the optimization framework. In the end, we apply our method to generate a rectangular temperature profile in the recording medium of the HAMR system.

1. INTRODUCTION

Topology optimization is a computational tool that can be used for the systematic design of photonic crystals, waveguides, resonators, filters and plasmonic structures [1]. Before its widespread use in designing photonic structures. it was first used in mechanical structural design [2] and became available in many structural simulation software (ANSYS, COMSOL). In general, there are three types of optimizations related to photonics and structural design. The first one, size optimization, finds the optimal design by changing the size variables, such as the slot distance of a bowtie antenna, for a fixed geometry. The shape optimization is mainly performed by modifying predetermined boundaries to achieve the optimal designs. It poses constraints on the connectivity and order of the device geometry. For example, we can approximate a 2D device geometry using points of a polygon and modify their positions. The last one, topology optimization, assumes no topological constraint on the geometry and searches for the optimal shape. While the size optimization and shape optimization are most frequently used in designing simple device where the underlying principles are reachable through intuition, the topology optimization is suited for generating non-intuitive designs for complex problems.

This thesis starts from an analysis on the Maxwell's equations, the mathematical formula for photonics, and focuses on the derivations of the methods used in topology optimization. We recognize and explain the difficulty of applying topology optimization to plasmonics involving strong subwavelength field enhancement and offer a robust solution. Topology optimization in plasmonics has only been reported in recent years and is almost exclusively used with the Finite Element Method (FEM) or the Boundary Element Method (BEM). The solution we present offers the chance to carry out topology optimization with the Finite-Difference Time-Domain (FDTD) [3] method and enables the use of a great number of techniques in structural topology optimization.

1.1 Topology Optimization in Photonics

The types of topology optimization generally fall into two categories: eigenvalue problems and deterministic problems [4]. Their differences are illustrated in Fig. 1.1.

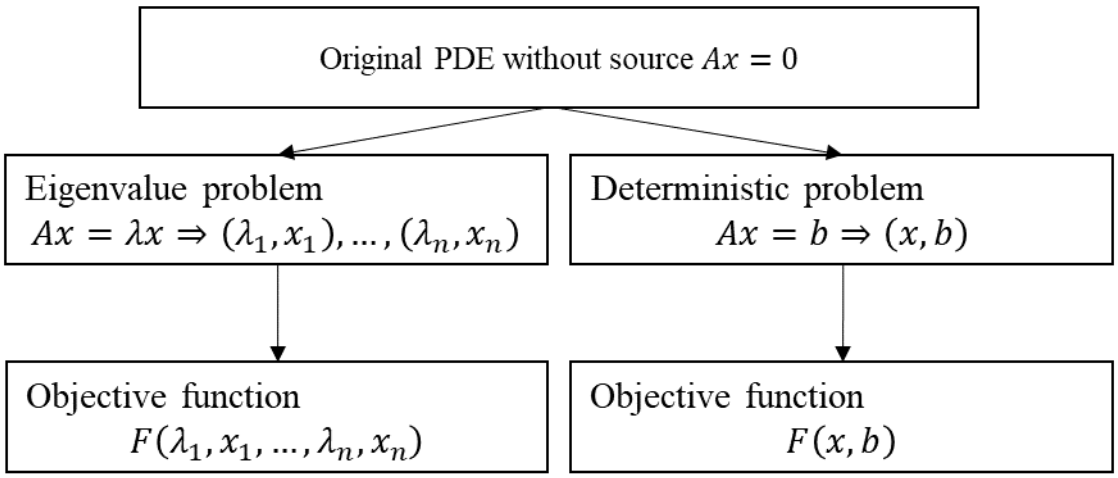

Fig. 1.1 Differences between deterministic problems and eigenvalue problems. The Partial Differential Equation (PDE) is deemed as an operator operation $Ax = b$ where A is the system operator, x is the field variable and b is the source term. In deterministic problems, the objective function depends on field variables. In eigenvalue problems, it depends on eigenvalues and/or eigenfunctions.

In eigenvalue problems, quantities relevant to modes of the system are considered. One notable example is the maximization of band gaps in photonic crystals [5] where the objective function is the gap between two eigenvalues. On the other hand, the deterministic problems aim to optimize quantities calculated from the response of some electromagnetic sources. For example, transmission loss of a 90^0 bend in a two-dimensional photonic crystal waveguide is made less than 0.3% using topology optimization [6]. Although the two types of problems are quite different in their formulations, they only differ in sensitivity analysis and many techniques can be applied to both types. We focus on deterministic problems as they incorporate the use of adjoint sensitivity analysis which is the other focus of this thesis. We also restrain ourselves to single frequency optimization, i.e., optimizing quantities calculated from a single wavelength. For problems involving multiple frequencies, the same methods can be employed multiple times to these

frequencies, at the cost of increasing run time. For more information on multiple frequency optimization, refer to [7][8][9].

A typical topology optimization in photonics problem is constructed with an objective function depending on the electromagnetic fields $(\mathbf{E}, \mathbf{H})$, design parameter ρ describing the structure in use and a couple of constraints including the Maxwell's equations and boundary conditions. To put it in a general mathematical form, consider the following optimization problem

$$\min_{\rho} F(\mathbf{E}, \mathbf{H}) \qquad 1\text{-}1$$

$$\text{subject to: } \begin{pmatrix} -i\omega\varepsilon & \boldsymbol{\nabla}\times \\ \boldsymbol{\nabla}\times & i\omega\mu \end{pmatrix} \begin{pmatrix} \mathbf{E} \\ \mathbf{H} \end{pmatrix} = \begin{pmatrix} \mathbf{J} \\ -\mathbf{M} \end{pmatrix}$$

$$\text{some boundary conditions}$$

$$\varepsilon = \varepsilon(\rho)$$

$$\mu = \mu(\rho)$$

$$\text{some other constraints on } \rho$$

At first, it is not obvious how the problem can be solved. The genetic algorithm is one of the global optimization algorithms [10], does not necessarily require the gradient information and is easy to implement. A genetic algorithm was successfully applied to design a planar silica spot-size converter as a fiber-to-ridge waveguide connection [11]. A waveguide-to-fiber coupling efficiency improvement exceeding 2 dB per converter is shown. If gradients are provided, local (convex) optimization algorithms can be deployed to find the optimal value within the neighborhood of an initial candidate. When problem is convex [12], local optimization algorithms are guaranteed to find the global optima. Although in practice most optimization problems are non-convex, some considerable improvement is still expected through local optimization. For instance, solar absorption enhancement of 30% resulting from a topology optimized surface texturing is reported in [13]. More recently, a computationally generated waveguide design was demonstrated to reduce the self-heating of the near-field transducer by 50% in a heat-assisted magnetic recording system [14]. Global optimization is generally orders of magnitude more computationally expensive than local optimization, which prevents its use in extremely large scale problems. We turn our attention to local optimization algorithms not only because they are less computationally expensive but also they are conceptually more interesting. Moreover, regularization techniques can be introduced to

reduce the non-convexity of the optimization problem. To emphasize the use of gradient, we will use the term gradient-based optimization instead of local optimization from now on.

1.2 The Adjoint Sensitivity

To facilitate the use of gradient-based topology optimization, gradient information must be accessible. However, the dependence of the objective function on the design parameter ρ is implicitly specified through the constraints imposed by boundary conditions and the Maxwell's equations, resulting in no explicit differentiation of the objective function. This is where the adjoint sensitivity analysis bridges the gap. The adjoint sensitivity analysis evaluates gradients with respect to all the design parameters using only two EM analysis regardless of the number of parameters [15]. It should be noticed that sensitivities and gradients are two fundamentally equivalent terms in topology optimization but have different meanings in other areas. They will be used interchangeably since there is no danger of confusion here in the topology optimization community. The early use of adjoint sensitivity was introduced in optimal control theory [16]. Fundamentally, the adjoint sensitivity is a methodology to calculate gradient information for non-linear objective functions of PDE-constrained design variables. By solving an extra adjoint version of the original PDE, the gradient can be calculated. Two forms of adjoint sensitivities are broadly used. Favored by Sigmund and Bendose [17], the discrete (numerical) adjoint sensitivity is obtained by differentiation of the discretized model of the original PDE with respect to the design variables. In the case of Finite Element Method, the following discretized optimization problem is considered

$$\begin{aligned} &\min_{\rho} F(x,\rho) \\ \text{subject to:}\quad &\mathbf{K}(\rho)x = b \\ &\text{some other constraints on } \rho \end{aligned} \qquad \text{1-2}$$

where matrix $\mathbf{K}(\rho)$ is the discretized representation of the original PDE, x are the discretized field vectors and b is the discretized current source vector. The sensitivity of the objective function with respect to the ith design variable ρ_i is given by the chain rule

$$\frac{dF}{d\rho_i} = \left(\frac{\partial F}{\partial x}\right)^T \frac{dx}{d\rho_i} + \frac{\partial F}{\partial \rho_i} \tag{1-3}$$

and the adjoint equation is given by

$$\mathbf{K}(\rho)^T x_a = \frac{\partial F}{\partial x} \tag{1-4}$$

where the superscript ^{T} denotes transpose of matrix. The sensitivity can be computed as:

$$\frac{dF}{d\rho} = -x_a^T \frac{\partial \mathbf{K}}{\partial \rho_i} x + \frac{\partial F}{\partial \rho_i} \tag{1-5}$$

On the other hand, the continuous (variational) adjoint sensitivity analysis starts with the original PDE and boundary conditions (or its equivalent variational form), then derives the adjoint PDE and adjoint boundary conditions with which the continuous sensitivity can be computed [18]. Translating the continuous sensitivity to gradients with respect to design variables is done afterwards using numerical methods. Fig. 1.2 illustrates differences between the continuous adjoint sensitivity analysis and the discrete adjoint sensitivity analysis.

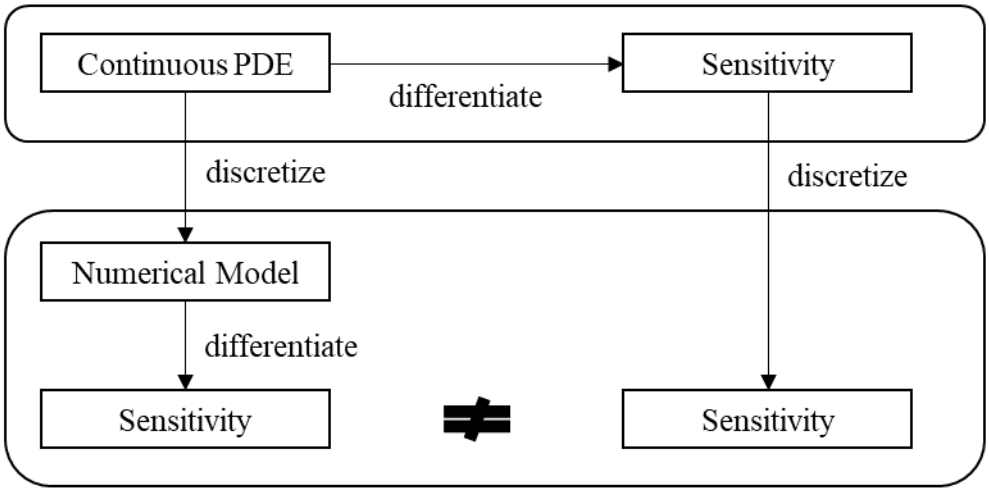

Fig. 1.2. Discrete (numerical) adjoint sensitivity compared with continuous (variational) adjoint sensitivity. The two are generally not equal. Especially in plasmonic structures, they exhibit a huge difference.

In most wave propagation problems, the adjoint system is the same as the original system. For lossless homogeneous boundary conditions [4] including the Perfect Electric Conductor (PEC), Perfect Magnetic Conductor (PMC) and the Bloch periodic condition, the adjoint boundary conditions end up being the same as the original. For the permittivity and permeability that are symmetric tensors the adjoint Maxwell's equations are also the same as the original. We will focus on the usage of the adjoint sensitivity analysis in open region problems and derive formulas for both discrete and continuous adjoint sensitivity analysis where the FDTD method [3] is the numerical model of the PDE.

For many years. the topology optimization has been primarily applied to design dielectric structures including photonic crystals [5][7][6], optical cloaks [19][20][21], solar cells [13], etc. However, there are very few about plasmonics. This is because the difficulty of obtaining accurate field solutions near sharp edges and corners [22] in plasmonic structures prohibits an accurate evaluation of sensitivity. Since it is at the material boundaries where the sensitivity is the highest, the continuous gradient is unreliable, inconsistent with the discrete gradient and leads to failure of convergence for gradient-based optimization algorithms. Especially in the FDTD method where material boundaries are approximated with staircasing geometry, field enhancement in the near-

zone of metal-dielectric interface cannot be accurately captured. To our knowledge, there are only two original methods of using the FDTD method in optimizing plasmonic structures until today [23][24][25]. Nevertheless, the FDTD method has been extensively used in simulating plasmonic structure. So, there is no reason the FDTD method should be abandoned in topology optimization of plasmonics. The difficulty of obtaining reliable and consistent sensitivity can be eliminated if the discrete adjoint sensitivity analysis is used to provide gradients for the optimization process instead of the continuous one because it represents the exact gradient of the underlying numerical model. Discrete matrix representation of the system is directly accessible with frequency domain solvers like FEM or BEM and enables easy implementation of discrete adjoint sensitivity analysis. However, the FDTD method does not have a discrete matrix representation in frequency domain.

The adjoint variable method (AVM) proposed in [9] considers the time marching scheme in the FDTD method as a dynamic system and uses time traversal to simulate the adjoint system. It was shown that this method works reasonably well in both dielectrics [15] and plasmonics [25]. However, even though the adjoint equation can be solved without modifying the existing FDTD solver, the approach only works on permittivity, depends on implementation of dispersion and only works with simple time-domain objective functions. Perhaps these are the reasons why the AVM has not been widely used in topology optimization. The bubble method [14] was also applied in design of plasmonic apertures/antennas. However, it is still a continuous sensitivity formula and does not have rigid theorical foundation. We propose a frequency domain sensitivity analysis by transforming the discrete time marching dynamic system of the FDTD method into frequency domain using discrete-time Fourier transform (DTFT) [26]. The frequency domain transform technique in obtaining sensitivity was previously demonstrated in 2D plasmonic structures but exploits the transmission line modeling (TLM) instead of the FDTD method [24]. Our approach is highly compatible with existing FDTD software (Meep, Lumerical, etc.) since almost all interesting quantities are calculated using DTFT; it is implemented in 3D model; it is independent of numerical implementation of dispersion if proper time step is chosen. Although the presented derivations are based on an open region problem, the method can be readily extended to problems with lossless homogeneous boundary conditions.

1.3 Geometry Parameterization

Two major approaches have been used to parameterize the geometry, i.e., to define an explicit dependence of ε, μ on the design parameters ρ in Equation 1-1: either use a level-set approach or a density approach. In the level-set approach, geometry is parameterized by a smooth level-set function ϕ which defines the material domain Ω, the void domain $\overline{\Omega}^c$ and the material interface $\partial\Omega$ as

$$\begin{cases} \phi(x) > c \Leftrightarrow x \in \Omega \\ \phi(x) = c \Leftrightarrow x \in \partial\Omega \\ \phi(x) < c \Leftrightarrow x \in \overline{\Omega}^c \end{cases} \quad \text{1-6}$$

where c is a constant (usually $c = 0$). An example is illustrated in Fig. 1.3. The level-set function ϕ is usually defined as the sum of the basis function ϕ_i

$$\phi(x) = \sum_i \phi_i(x, s_i) \quad \text{1-7}$$

where s_i the ith design parameter. The level-set approach is closely related to shape optimization in the sense that both allow altering boundaries. Different from shape optimization, the level-set approach allows topological changes, i.e., new holes can merge and new connections can be formed [27]. However, the forming of new holes is done in a separate step using topological derivatives [28].

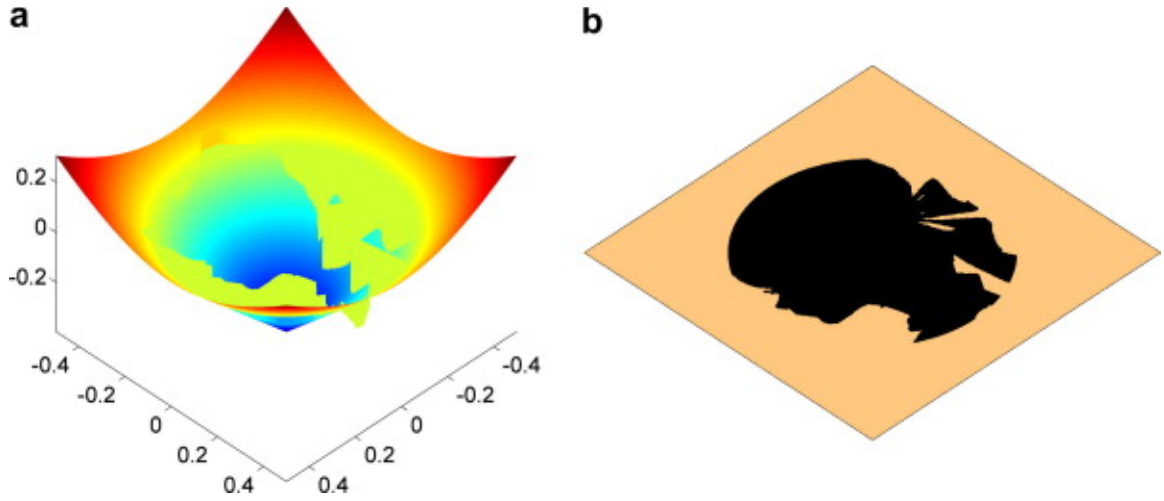

Fig. 1.3. Level-set approach for a 2D geometry. The 2D geometry is a section of the level-set function. Reprinted from [29] with the permission of Elsevier.

To move towards a device design, ϕ is then evolved either through an equation of motion (such as the Hamilton-Jacobi [30]) or via gradients with respect to design variables using mathematical programming techniques [27], causing it to settle at local optima [31]. The level-set method is highly compatible with FEM and BEM. since mesh can be generated to conform the boundary. Most topology optimization in plasmonics is done in this way for its high accuracy in capturing localized fields [22][32][29]. However, the drawbacks of the level set approach are the restriction of the geometry that only can evolve from existing boundaries and the inability to generate new holes at point surrounded by solid material [17]. Even though the use of topology derivatives can mitigate these drawbacks, it is usually done in a separate step of the optimization procedure, affecting the convergence of the optimization process. For a comprehensive review on the level-set approach in topology optimization, refer to [27].

The density approach, on the other hand, parameterizes the geometry using a density paramter ρ. For example

$$\varepsilon(x,\rho) = \varepsilon_1\rho(x) + \varepsilon_2\big(1-\rho(x)\big), \qquad \rho \in [0,1] \tag{1-8}$$

where ε_1 is the permittivity for the material domain and ε_2 is the permittivity for the void domain (usually $\varepsilon_2 = \varepsilon_0$). Under a specific numerical model of the Maxwell's equations, each node (line segment, pixel or voxel) is assigned a density parameter and the problem of finding the optimal design amounts to determining the value of ρ for each node. One drawback of the density approach is that gray transition regions where ρ takes intermediate values can occur in the final optimal structure. Such gray transition regions do not represent any realistic geometry and might lead to inadmissible device design. For a comprehensive review on density approach, refer to [33].

In either level-set or density approach, the adjoint sensitivity analysis can provide gradient information for the optimization process. Both discrete and continuous sensitivity analysis are easily applied to density-based optimization while the level-set can only accept the continuous sensitivity most of the time except when density-based geometric mapping is employed [27]. We will give a brief review on adjoint sensitivity applied to level-set method, but the focus is on the density approach as it is highly compatible with cartesian grids in the FDTD method.

1.4 Regularization

Even when the gradient is absolutely correct, the ill-posedness of the optimization problem in Equation 1-1 may still cause the optimization to converge to a local minimum with poor performance. The ill-posedness can cause: (1) mesh dependence, (2) gray transition regions, (3) poor manufacturability and (4) non-uniqueness of the solution. Mesh dependency can be observed by refining the design domain for a design obtained with a coarse mesh and running the optimization on the refined mesh [33]. The issue of gray transition regions is discussed in the previous section and only exists in density approach. Poor manufacturability of the optimized structure as a result of extremely small geometry features prevents realistic application of the design. For instance, the design can have element holes or material islands that are neither manufacturable nor make physical sense [1]. Although seemingly innocent, the non-uniqueness of

the solution can sometimes lead to poor convergence [34]. Regularization can be used to mitigate these problems by restricting the solution space. We will focus on techniques used in the density approach. However, it should be noted that many methods can also be applied to the level-set approach.

Inspired by image processing, density filtering methods have been successful in ensuring manufacturability and mesh independence [35]. Viewing the discretized density parameter ρ as a 3D image, we can reassign each density value ρ_i as a weighted sum of its neighbors:

$$\hat{\rho}_i = \frac{\sum_{j \in N_i} w_{ij} A_j \rho_j}{\sum_{j \in N_i} w_{ij} A_j} \tag{1-9}$$

where the A_j is the area of the jth element and the weighting function is given by:

$$w_{ij} = R - \left\| \boldsymbol{x}_i - \boldsymbol{x}_j \right\| \tag{1-10}$$

This introduces a length scale R into the design problem, i.e., no features like holes or solid bridges will be smaller than R [1]. Alternatively, the filter can be applied to the sensitivity [36]:

$$\frac{\partial F}{\partial \hat{\rho}_i} = \frac{\sum_{j \in N_i} w_{ij} \frac{\partial F}{\partial \rho_i}}{\sum_{j \in N_i} w_{ij}} \tag{1-11}$$

The main idea of sensitivity filter is to base design updates on filtered sensitivities instead of real sensitivities. Obviously, this is potentially risky since a wrong descent direction might be taken. The penalization approach adds an artificial penalization term to the objective function to ensure crisp, mesh-independent 0-1 design. For example [37],

$$\hat{F} = F + \alpha \int_{\Omega} \rho(1-\rho) dV \tag{1-12}$$

where $\hat{F}$ is new objective function and α controls the weight of the penalization term favoring a density value of either 0 or 1. For a comprehensive review on regularization in density approach, refer to [33]. As we will see, regularization is necessary in topology optimization in plasmonics for the objective function is highly sensitive to material variation. Such high sensitivities result in high non-convexity of the problem and cause premature convergence to a local optimum.

1.5 Implementation

Since the goal is to illustrate the robustness of the discrete adjoint sensitivity formula of FDTD method discussed, the density-based topology optimization is used along with several standard regularization techniques [38] and the non-linear material interpolation scheme [39]. We end up writing our own FDTD solver because we need to control what interpolation scheme goes into the algorithm and to access each individual field component in the Yee lattice. The part involving optimization is written in Python using the Scipy and Numpy libraries [40]. The optimization is solved using the Method of Moving Asymptotes [41] (MMA) and a Python interface [42] of MMA is adopted in our code.

1.6 Organization of Chapters

The rest of the thesis generally follows the contents of the introduction.

Chapter 2 presents a detailed derivation of adjoint sensitivity starting from the symmetry property of Maxwell's equations – the Lorentz Reciprocity – followed by a mathematical interpretation – the adjoint operator – from a function analytic point of view. Using language from the adjoint operator theory, the classical continuous adjoint sensitivity analysis is discussed. Afterwards, it re-iterates the difficulty of obtaining accurate sensitivity in plasmonics, which serves as the motive for the next section – discrete adjoint sensitivity with FDTD – providing a discrete sensitivity formula for scalar permittivity and permeability. Two examples and numerical implementation are given in the end.

Chapter 3 reviews the two different ways to represent geometry, the level-set function and density function, with a focus on the latter. Consequences of the ill-posedness of the topology optimization

problems are discussed, including poor manufacturability, gray transition regions and non-smooth convergence, followed by an introduction of regularization techniques that cope with the ill-posedness. The so-called standard method [38] is given a detailed elucidation and ends up being implemented.

Chapter 4 carries out the topology optimization on two plasmonic structures, one with localized fields and one without localized fields, to demonstrate the possibility of using topology optimization to construct field patterns.

In Chapter 5, the topology optimization is applied to the design of a coupled thermal-electromagnetic system, the heat-assisted magnetic recording system. An inverse thermal problem is instigated followed by solving an inverse electromagnetic problem using topology optimization, in which the same procedures from Chapter 4 are followed.

2. ADJOINT SENSITIVITY ANALYSIS

Gradient-based optimization has long history of success in finding local optima because of its deterministic nature. To facilitate such powerful tool, which is almost available as libraries in all scientific programming languages (fminunc in MATLAB, scipy.optimize in Python, etc.), the gradient must be provided. This Chapter describes gradient derivations for the Maxwell's equations from the continuous perspective and the discrete perspective and introduces the adjoint sensitivity analysis. The adjoint sensitivity analysis evaluates the sensitivities with respect to all the design parameters using only two EM analysis regardless of the number of parameters [15]. Gradient-based non-linear optimization algorithms, such as the mothod of moving asymptotes [41] (MMA), limited memory BFGS [43] (L-BFGS-B), can be initiated to optimize a user-defined objective function with these provided sensitivities.

For a single variable function with analytical form, gradient is nothing more than the derivative with respect to the variable. For multiple variables, the gradient comes into play. But for infinite ly many variables, the gradient is often disguised as a function. Discussion of infinitely many variables is the starting point of functional analysis [44] and is inevitable if we want to talk about sensitivity of Maxwell's equations. We shall not dive into the abstraction of functionals, but some generalizations of adjoint sensitivity analysis rely on jargons borrowed from this field. Hence the goal is to present the material to audience with nodding acquaintance of basic functional analysis and still provide information enough for to initiate one's own sensitivity analysis.

Sensitivity analysis provides information on how much the behavior of the system changes if the input is altered by a small amount. The input can either be currents or geometric information of the system and the output is usually a measure of some performance. For instance, the transmission of a waveguide depends on the waveguide geometry. Here geometry is described by permittivity distribution and transmission is calculated as the ratio of transmitted power over the incident power. If we understand how the transmission changes by altering the geometry, we may very well come up with a waveguide design that maximizes the transmission. In this chapter, we address sensitivity

of changing geometry of objects in an electromagnetic system and derivate gradients with which a user-defined objective function can be optimized.

This chapter also addresses the difficulty of obtaining accurate sensitivity in plasmonics. In order to perform topology optimization, a solver of direct electromagnetic problem is required. The solver should be accurate enough to yield acceptable sensitivity. This is particularly compelling if we are interested in the accurate evaluation of electric field in the near zone of a plasmonic particle [32]. Since the FDTD method [3] is widely used in plasmonic structure simulation, we present a new discrete-based method in conjunction with the FDTD method to yield numerically accurate sensitivity. We give theoretical proofs that the error is very small with a fine time step. We argue that this can serve as framework of sensitivity analysis for any type of topology optimization in electromagnetics when the FDTD method is used as the direct solver.

2.1 The Lorentz Reciprocity

Before introducing the abstract adjoint operator theory, we will look at its alternative and more intuitive form – the Lorentz reciprocity – which is an important concept in antennas because it produced implications when we reverse the role of transmitting antennas and receiving antennas. Loosely, it states that the relationship between an oscillating current and the resulting electric field is unchanged if one interchanges the points where the current is placed and where the field is measured.

A formal derivation of the Lorentz reciprocity begins by considering a volume containing two sets of sources in an unbounded region, $\mathbf{J}_1$ and $\mathbf{J}_2$, which produced fields $(\mathbf{E}_1, \mathbf{H}_1)$ and $(\mathbf{E}_2, \mathbf{H}_2)$ respectively, as shown in Fig. 2.1.

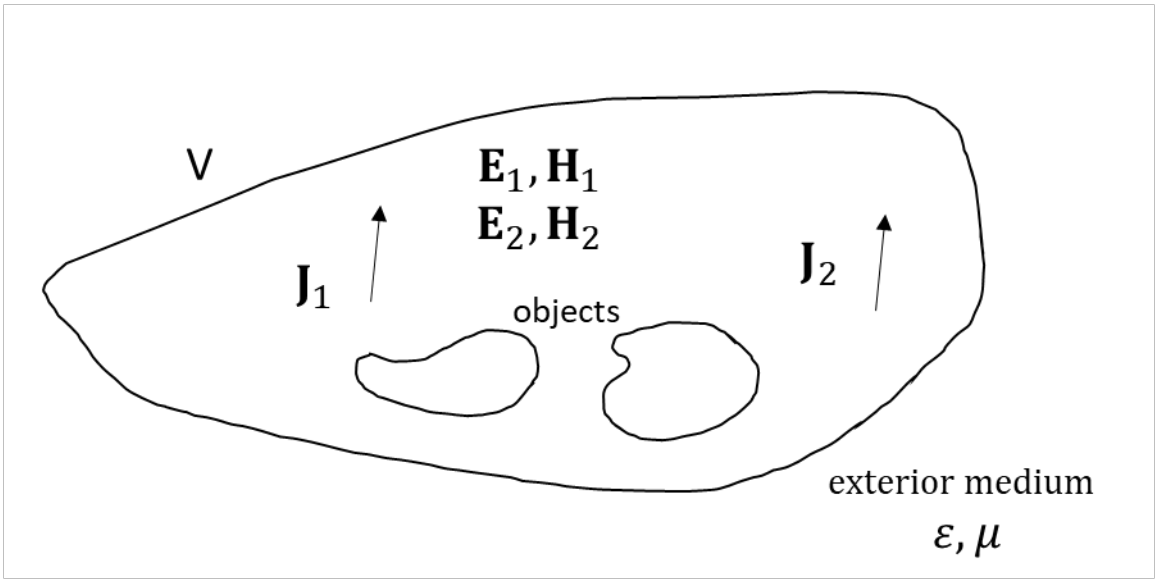

Fig. 2.1 Two sets of sources in an unbounded region with a uniform background medium and and an inhomogenous region of interest V. This is a typical set-up for wave propagation problem. Two sources are assumed to be compactly supported in the region V.

Consider the quantity $\boldsymbol{\nabla} \cdot (\mathbf{E}_1 \times \mathbf{H}_2 - \mathbf{E}_2 \times \mathbf{H}_1)$ which is expandable using a vector identity as

$$(\boldsymbol{\nabla} \times \mathbf{E}_1) \cdot \mathbf{H}_2 - (\boldsymbol{\nabla} \times \mathbf{H}_2) \cdot \mathbf{E}_1 - (\boldsymbol{\nabla} \times \mathbf{E}_2) \cdot \mathbf{H}_1 + (\boldsymbol{\nabla} \times \mathbf{H}_1) \cdot \mathbf{E}_2 \qquad 2\text{-}1$$

According to Maxwell's curl equations assuming sinusoidal time dependence $e^{i\omega t}$

$$\boldsymbol{\nabla} \times \mathbf{E}_1 = -i\omega\mu\mathbf{H}_1 - \mathbf{M}_1 \qquad 2\text{-}2$$
$$\boldsymbol{\nabla} \times \mathbf{H}_1 = i\omega\varepsilon\mathbf{E}_1 + \mathbf{J}_1 \qquad 2\text{-}3$$
$$\boldsymbol{\nabla} \times \mathbf{E}_2 = -i\omega\mu\mathbf{H}_2 - \mathbf{M}_2 \qquad 2\text{-}4$$
$$\boldsymbol{\nabla} \times \mathbf{H}_2 = i\omega\varepsilon\mathbf{E}_2 + \mathbf{J}_2 \qquad 2\text{-}5$$

Therefore,

$$\begin{aligned} \boldsymbol{\nabla} \cdot (\mathbf{E}_1 \times \mathbf{H}_2 - \mathbf{E}_2 \times \mathbf{H}_1) &= -(-i\omega\mu\mathbf{H}_2 - \mathbf{M}_2) \cdot \mathbf{H}_1 + (i\omega\varepsilon\mathbf{E}_1 + \mathbf{J}_1) \cdot \mathbf{E}_2 \\ &\quad +(-i\omega\mu\mathbf{H}_1 - \mathbf{M}_1) \cdot \mathbf{H}_2 - (i\omega\varepsilon\mathbf{E}_2 + \mathbf{J}_2) \cdot \mathbf{E}_1 \\ &= \mathbf{J}_1 \cdot \mathbf{E}_2 - \mathbf{M}_1 \cdot \mathbf{H}_2 - (\mathbf{J}_2 \cdot \mathbf{E}_1 - \mathbf{M}_2 \cdot \mathbf{H}_1) \end{aligned} \qquad 2\text{-}6$$

Integrating the divergence over the volume of interest gives

$$\iiint_V \nabla \cdot (\mathbf{E}_1 \times \mathbf{H}_2 - \mathbf{E}_2 \times \mathbf{H}_1) dV = \iiint_V \big(\mathbf{J}_1 \cdot \mathbf{E}_2 - \mathbf{M}_1 \cdot \mathbf{H}_2 - (\mathbf{J}_2 \cdot \mathbf{E}_1 - \mathbf{M}_2 \cdot \mathbf{H}_1)\big) dV \tag{2-7}$$

and applying the Divergence theorem to the left-hand side yields

$$\iint_{\partial V} (\mathbf{E}_1 \times \mathbf{H}_2 - \mathbf{E}_2 \times \mathbf{H}_1) \cdot dS = \iiint_V \big(\mathbf{J}_1 \cdot \mathbf{E}_2 - \mathbf{M}_1 \cdot \mathbf{H}_2 - (\mathbf{J}_2 \cdot \mathbf{E}_1 - \mathbf{M}_2 \cdot \mathbf{H}_1)\big) dV \tag{2-8}$$

We now claim that the left-hand side is zero when the volume of interest V encloses all sources and objects. Notice that for electric fields and magnetic fields observed at a large distance from the sources, $\mathbf{E}$ and $\mathbf{H}$ are related through

$$\mathbf{H} = \frac{\hat{r} \times \mathbf{E}}{\eta} \tag{2-9}$$

where η is the background impedance. Assuming the volume of interest is a large ball B_r of radius r centered at the sources and using the above relation, the integrand on the left-hand side of Equation 2-8 can be rewritten as

$$\iint_{\partial B_r} \left(\mathbf{E}_1 \times \frac{\hat{r} \times \mathbf{E}_2}{\eta} - \mathbf{E}_2 \times \frac{\hat{r} \times \mathbf{E}_1}{\eta}\right) \cdot \hat{r} dS = \iint_{\partial B_r} \left(\mathbf{E}_1 \cdot \frac{\mathbf{E}_2}{\eta} - \mathbf{E}_2 \cdot \frac{\mathbf{E}_1}{\eta}\right) dS = 0 \tag{2-10}$$

Hence

$$\iiint_{B_r} (\mathbf{J}_1 \cdot \mathbf{E}_2 - \mathbf{M}_1 \cdot \mathbf{H}_2) dV = \iiint_{B_r} (\mathbf{J}_2 \cdot \mathbf{E}_1 - \mathbf{M}_2 \cdot \mathbf{H}_1) dV \tag{2-11}$$

Now supposing the volume of interest V is any volume enclosing all sources and objects, we subtract it from a large ball centered around the sources and use the subtracted volume in Equation 2-8

$$\begin{aligned}&\iiint_{B_r-V} \boldsymbol{\nabla}\cdot(\mathbf{E}_1\times\mathbf{H}_2-\mathbf{E}_2\times\mathbf{H}_1)dV\\&=\iiint_{B_r-V}\left(\mathbf{J}_1\cdot\mathbf{E}_2-\mathbf{M}_1\cdot\mathbf{H}_2-(\mathbf{J}_2\cdot\mathbf{E}_1-\mathbf{M}_2\cdot\mathbf{H}_1)\right)dV\end{aligned} \tag{2-12}$$

Noticing that there are no sources in the volume $B_r - V$ which implies the right-hand side of the above equation is 0, we invoke the Divergence theorem again to the left-hand side

$$\iint_{\partial B_r}(\mathbf{E}_1\times\mathbf{H}_2-\mathbf{E}_2\times\mathbf{H}_1)\cdot dS-\iint_{\partial V}(\mathbf{E}_1\times\mathbf{H}_2-\mathbf{E}_2\times\mathbf{H}_1)\cdot dS=0 \tag{2-13}$$

Combining Equations 2-13 and 2-10 yields

$$\iint_{\partial V}(\mathbf{E}_1\times\mathbf{H}_2-\mathbf{E}_2\times\mathbf{H}_1)\cdot dS=0 \tag{2-14}$$

This indicates the left-hand side of Equation 2-8 is always 0 no matter what volume of interest is chosen as long as it encloses all sources and objects. At last, we arrive at a more general version of Equation 2-11

$$\iiint_V(\mathbf{J}_1\cdot\mathbf{E}_2-\mathbf{M}_1\cdot\mathbf{H}_2)dV=\iiint_V(\mathbf{J}_2\cdot\mathbf{E}_1-\mathbf{M}_2\cdot\mathbf{H}_1)dV \tag{2-15}$$

which is valid for any volume V enclosing all sources and objects. This is the Lorentz Reciprocity for linear isotropic materials. One immediate consequence of the Lorentz Reciprocity is that fields of dipole sources are symmetric. Considering two dipole sources $\mathbf{J}_1=\mathbf{A}_1\delta(\boldsymbol{r}-\boldsymbol{r}_1)$ and $\mathbf{J}_2=\mathbf{A}_2\delta(\boldsymbol{r}-\boldsymbol{r}_2)$, Equation 2-15 implies that

$$\mathbf{A}_1 \cdot \mathbf{E}_2(\boldsymbol{r}_1) = \mathbf{A}_2 \cdot \mathbf{E}_1(\boldsymbol{r}_2) \tag{2-16}$$

This relation is illustrated in Fig. 2.2.

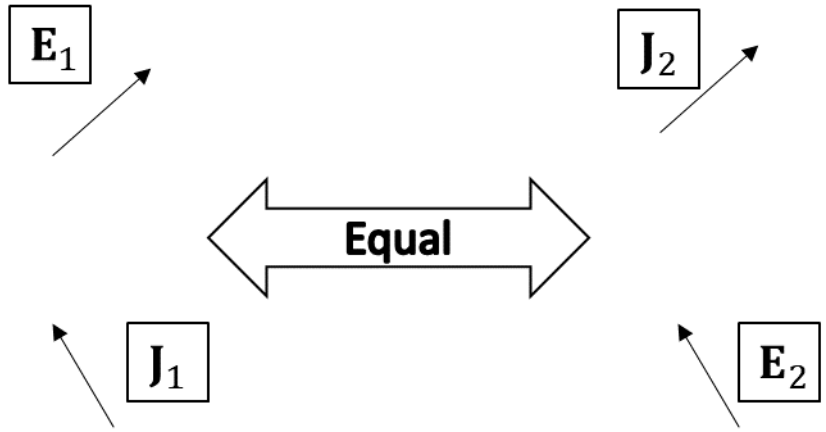

Fig. 2.2 Symmetry of fields and sources. Measuring electric field $\mathbf{E}_1$ along direction $\mathbf{A}_2$ is equivalent to measuring electric field $\mathbf{E}_2$ along direction $\mathbf{A}_1$.

The more general relation is the symmetry of Green's function. We obtain electric fields by using the convolution product of Green's function and sources

$$\mathbf{E}_2(\boldsymbol{r}_1) = \iiint_V \mathbf{G}(\boldsymbol{r}_1, \boldsymbol{r}) \cdot \mathbf{J}_2(\boldsymbol{r}) dV = \mathbf{G}(\boldsymbol{r}_1, \boldsymbol{r}_2) \cdot \mathbf{A}_2 \tag{2-17}$$

$$\mathbf{E}_1(\boldsymbol{r}_2) = \iiint_V \mathbf{G}(\boldsymbol{r}_2, \boldsymbol{r}) \cdot \mathbf{J}_1(\boldsymbol{r}) dV = \mathbf{G}(\boldsymbol{r}_2, \boldsymbol{r}_1) \cdot \mathbf{A}_1 \tag{2-18}$$

and combine Equations 2-16, 2-17 and 2-18

$$\mathbf{A}_1 \cdot \mathbf{G}(\boldsymbol{r}_1, \boldsymbol{r}_2) \cdot \mathbf{A}_2 = \mathbf{A}_2 \cdot \mathbf{G}(\boldsymbol{r}_2, \boldsymbol{r}_1) \cdot \mathbf{A}_1 \tag{2-19}$$

Since $\mathbf{A}_1$ and $\mathbf{A}_2$ are arbitrary, the symmetry of Green's function must be satisfied

$$\mathbf{G}(\boldsymbol{r}_1, \boldsymbol{r}_2) = \mathbf{G}^{\mathrm{T}}(\boldsymbol{r}_2, \boldsymbol{r}_1) \tag{2-20}$$

It should be noted that Equation 2-20 is equivalent to the Lorentz Reciprocity – there is a way to derive the Lorentz Reciprocity assuming the symmetry of Green's function.

The Lorentz Reciprocity does not generally hold for anisotropic materials. One notable example is magneto-optic material where ε is Hermitian, i.e.

$$\varepsilon^T = \bar{\varepsilon} \tag{2-21}$$

in which case Equation 2-6 no longer holds. To satisfy Equation 2-6, the following term must cancel

$$i\omega(\varepsilon\mathbf{E}_1 \cdot \mathbf{E}_2 - \varepsilon\mathbf{E}_2 \cdot \mathbf{E}_1) = 0 \tag{2-22}$$

For Hermitian ε the above term does not cancel while for symmetric ε the above term can still be cancelled. Therefore, the Lorentz Reciprocity only holds for materials with symmetric permittivity and permeability. Although the derivations start with an open region problem, the Reciprocity theorem also holds for bounded region problem if lossless homogeneous boundary conditions are imposed. For example,

$$\vec{n} \times \mathbf{E} = \mathbf{0} \text{ or } \vec{n} \times \mathbf{H} = \mathbf{0} \text{ at boundary} \tag{2-23}$$

Generalizations of the Lorentz Reciprocity [45] can be made following the footsteps of the above discussion, however, at the price of verbosity and tangling equations. A new perspective into this relation, in an algebraic form, is much simpler to deal with and provides even deeper insights.

2.2 The Adjoint Operator

We will assume that the reader is familiar with basic definitions of Hilbert space. For a brief introduction to Hilbert space, refer to Chapters 1,2 of [46]. To start with, we rewrite Maxwell's equations in an operator form:

$$\begin{pmatrix} -i\omega\varepsilon & \boldsymbol{\nabla}\times \\ \boldsymbol{\nabla}\times & i\omega\mu \end{pmatrix}\begin{pmatrix} \mathbf{E} \\ \mathbf{H} \end{pmatrix} = \begin{pmatrix} \mathbf{J} \\ -\mathbf{M} \end{pmatrix} \tag{2-24}$$

The two divergence equations are removed since they are not independent and wave propagation does not concern static charges. We investigate an open region problem with an infinite domain $\Omega = \mathbb{R}^3$. Inner product is assigned to be the integral of fields over the domain

$$\left\langle \begin{matrix} \mathbf{E_1} \\ \mathbf{H_1} \end{matrix} \middle| \begin{matrix} \mathbf{E_2} \\ \mathbf{H_2} \end{matrix} \right\rangle = \int_\Omega \mathbf{E}_1 \cdot \bar{\mathbf{E}}_2 \, d\Omega + \int_\Omega \mathbf{H}_1 \cdot \bar{\mathbf{H}}_2 \, d\Omega \tag{2-25}$$

Notice that the inner product might be ill-formed. Considering a plane-wave in the form $\mathbf{E}_1 = \mathbf{E_0} e^{-ik\cdot r}$, we write down the inner product of the plane-wave with itself and immediately notice that it explodes

$$\langle \mathbf{E}_1 | \mathbf{E}_1 \rangle = \int_\Omega |\mathbf{E_0}|^2 \, d\Omega = \infty \tag{2-26}$$

Such difficulty exists because the sources originate from infinitely far and do not satisfy the Sommerfeld radiation boundary condition [4]

$$\lim_{|\boldsymbol{r}|\to\infty} |\boldsymbol{r}| \left[\boldsymbol{\nabla} \times \begin{pmatrix} \mathbf{E} \\ \mathbf{H} \end{pmatrix} + \mathrm{j}k_0 \hat{r} \times \begin{pmatrix} \mathbf{E} \\ \mathbf{H} \end{pmatrix} \right] = 0 \tag{2-27}$$

The electromagnetic equivalence principle [47], commonly known as Huygens's principle, compactifies incident sources into finite current sources. The usage of the equivalence principle in simulation of scattering problem is called total-field/scattered-field (TF/SF) formulation [3]. In the TF/SF formulation, the whole domain is bisected into a compact region with total fields and an

infinite region with only scattered fields (Fig. 2.3). Using the electromagnetic field equivalence principle, we assign fictitious currents to a surface enclosing the scatters to generate an arbitrary incident wave. Fields inside the surface are total fields while fields outside are scattered fields.

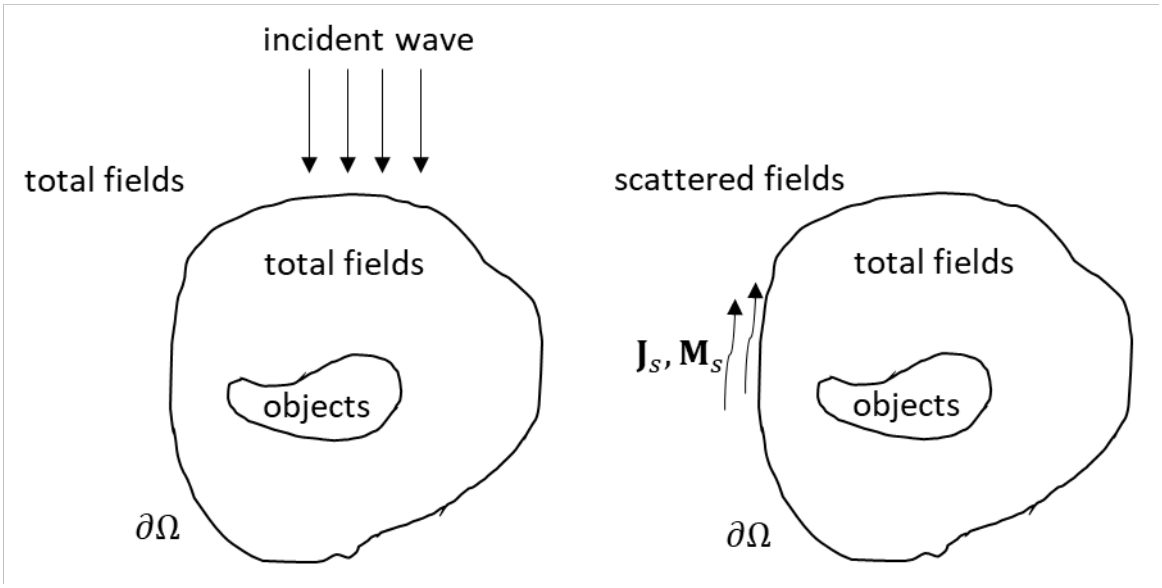

Fig. 2.3 Illustration of the electromagnetic field equivalence principle for electromagnetic wave scattering by a target in an unbounded region. Assigning the fictitious currents on the surface creates the same effect as an incident wave inside the volume Ω and scattered fields outside the volume.

The fictitious currents are given by

$$\mathbf{J}_s(\partial\Omega) = \hat{n} \times \mathbf{H}_{inc} \quad \text{2-28}$$

$$\mathbf{M}_s(\partial\Omega) = -\hat{n} \times \mathbf{E}_{\text{inc}} \quad \text{2-29}$$

In this way, currents are within a compact region and by Sommerfeld radiation condition the fields must vanish at infinity in a square-integrable way [48]. As a result, the solutions of Maxwell's equations belong to the space of square-integrable functions, the $L^2(\mathbb{R}^3)$ space, which is a Hilbert space [49]. We now introduce the definition of an operator: An operator **T** on a (complex) Hilbert space **H** is a linear map between the space and itself which satisfies:

$$\mathbf{T}(x+y) = \mathbf{T}x + \mathbf{T}y, \qquad \forall x, y \in \mathbf{H} \tag{2-30}$$
$$\mathbf{T}(ax) = a\mathbf{T}(x), \qquad \forall x \in \mathbf{H} \text{ and } \forall a \in \mathbb{C} \tag{2-31}$$
$$\mathbf{T}(x) \in \mathbf{H}, \qquad \forall x \in \mathbf{H} \tag{2-32}$$

Apparently, the Maxwell's equations are exactly an operator operation $\mathbf{\Lambda} x = b$ where

$$\mathbf{\Lambda} = \begin{pmatrix} -i\omega\varepsilon & \boldsymbol{\nabla}\times \\ \boldsymbol{\nabla}\times & i\omega\mu \end{pmatrix} \tag{2-33}$$

is the operator and

$$x = \begin{pmatrix} \mathbf{E} \\ \mathbf{H} \end{pmatrix}, \quad b = \begin{pmatrix} \mathbf{J} \\ -\mathbf{M} \end{pmatrix} \tag{2-34}$$

both belong to $L^2(\mathbb{R}^3)$. What is not obvious is that the Maxwell operator has an inverse. In fact, the inverse is exactly the convolution between Green's functions and sources

$$\begin{pmatrix} \mathbf{E} \\ \mathbf{H} \end{pmatrix} = \begin{pmatrix} \mathbf{G}_{11} * \mathbf{J} - \mathbf{G}_{12} * \mathbf{M} \\ \mathbf{G}_{21} * \mathbf{J} - \mathbf{G}_{22} * \mathbf{M} \end{pmatrix} = \begin{pmatrix} \mathbf{G}_{11} * & \mathbf{G}_{12} * \\ \mathbf{G}_{21} * & \mathbf{G}_{22} * \end{pmatrix} \begin{pmatrix} \mathbf{J} \\ -\mathbf{M} \end{pmatrix} \tag{2-35}$$

where $*$ specifies a convolution[1] between the Green's function and currents. $\mathbf{G}_{11}$ is exactly the Green's function used in Equation 2-20. Using the notation in Equations 2-33 and 2-34 and rewriting the Lorentz Reciprocity in Equation 2-15, we have

$$\left\langle \begin{matrix} \mathbf{E_1} \\ \mathbf{H_1} \end{matrix} \middle| \begin{matrix} \mathbf{J_2} \\ -\mathbf{M_2} \end{matrix} \right\rangle = \left\langle \begin{matrix} \mathbf{E_2} \\ \mathbf{H_2} \end{matrix} \middle| \begin{matrix} \mathbf{J_1} \\ -\mathbf{M_1} \end{matrix} \right\rangle \Leftrightarrow \langle x_1 | \overline{\mathbf{\Lambda} x_2} \rangle = \langle x_2 | \overline{\mathbf{\Lambda} x_1} \rangle = \langle \mathbf{\Lambda} x_1 | \overline{x_2} \rangle \tag{2-36}$$

Now we associate with each operator on a Hilbert space $\mathbf{H}$ its adjoint, another operator on the same Hilbert space denoted by $\mathbf{T}^\dagger$, which satisfies the following

$$\langle \mathbf{T}x | y \rangle = \langle x | \mathbf{T}^\dagger y \rangle, \qquad \forall x, y \in \mathbf{H} \tag{2-37}$$

[1] $*$ denotes convolution in the thesis

A classic example of Hilbert space is a finite dimensional vector space: here each operator is a matrix and its adjoint is exactly the conjugate transpose of itself. It turns out the adjoint of Maxwell's operator is also the conjugate transpose of itself

$$\mathbf{\Lambda}^{\dagger} = \begin{pmatrix} i\omega\bar{\varepsilon}^{T} & \boldsymbol{\nabla}\times \\ \boldsymbol{\nabla}\times & -i\omega\bar{\mu}^{T} \end{pmatrix} \tag{2-38}$$

Assuming symmetric permittivity and permeability, we have

$$\mathbf{\Lambda}^{\dagger} = \begin{pmatrix} i\omega\bar{\varepsilon} & \boldsymbol{\nabla}\times \\ \boldsymbol{\nabla}\times & -i\omega\bar{\mu} \end{pmatrix} = \bar{\mathbf{\Lambda}} \tag{2-39}$$

Combining the above Equation with the definition of adjoint operator in Equation 2-37 gives

$$\langle \mathbf{\Lambda} x_1 | \overline{x_2} \rangle = \langle x_1 | \mathbf{\Lambda}^{\dagger} \overline{x_2} \rangle = \langle x_1 | \bar{\mathbf{\Lambda}} \overline{x_2} \rangle = \langle x_1 | \overline{\mathbf{\Lambda} x_2} \rangle \tag{2-40}$$

which is exactly the Lorentz Reciprocity re-introduced in Equation 2-36. For Hermitian permittivity and permeability, we have

$$\mathbf{\Lambda}^{\dagger} = \begin{pmatrix} i\omega\varepsilon & \boldsymbol{\nabla}\times \\ \boldsymbol{\nabla}\times & -i\omega\mu \end{pmatrix} = -\mathbf{\Lambda} \tag{2-41}$$

Combining with the definition of adjoint operator in Equation 2-37 yields

$$\begin{aligned} &\langle \mathbf{\Lambda} x_1 | x_2 \rangle = \langle x_1 | \mathbf{\Lambda}^{\dagger} x_2 \rangle = \langle x_1 | -\mathbf{\Lambda} x_2 \rangle \\ &\Rightarrow \langle \mathbf{\Lambda} x_1 | x_2 \rangle + \langle x_1 | \mathbf{\Lambda} x_2 \rangle = 0 \end{aligned} \tag{2-42}$$

which is expandable as

$$\iiint_V (\mathbf{J}_1 \cdot \overline{\mathbf{E}_2} - \mathbf{M}_1 \cdot \overline{\mathbf{H}_2}) dV = \iiint_V (-\overline{\mathbf{J}_2} \cdot \mathbf{E}_1 + \overline{\mathbf{M}_2} \cdot \mathbf{H}_1) dV \tag{2-43}$$

In conclusion, the generalized Reciprocity theorem is a direct corollary from the property that the adjoint operator being equivalent to the transpose conjugate in Maxwell's equations. The notion of adjoint operator will play a vital part in determining sensitivity of the Maxwell's equation. The connection between the sensitivity and the adjoint of Maxwell's equation enables one to run only two simulations to determine derivatives of an objective function over hundreds of thousands of variables. This will be discussed in the next two sections.

Notice that the adjoint Maxwell operator produced another system with $\varepsilon^{\dagger} = -\bar{\varepsilon}^{T}$ and $\mu^{\dagger} = -\bar{\mu}^{T}$ where $\varepsilon^{\dagger}$ and $\mu^{\dagger}$ are permittivity and permeability for the adjoint system. At first glance, the adjoint flips signs of real part of permittivity and permeability and leaves imaginary part unchanged. This is equivalent to changing dielectrics to metals and metals to dielectrics, which is shown in Fig. 2.4.

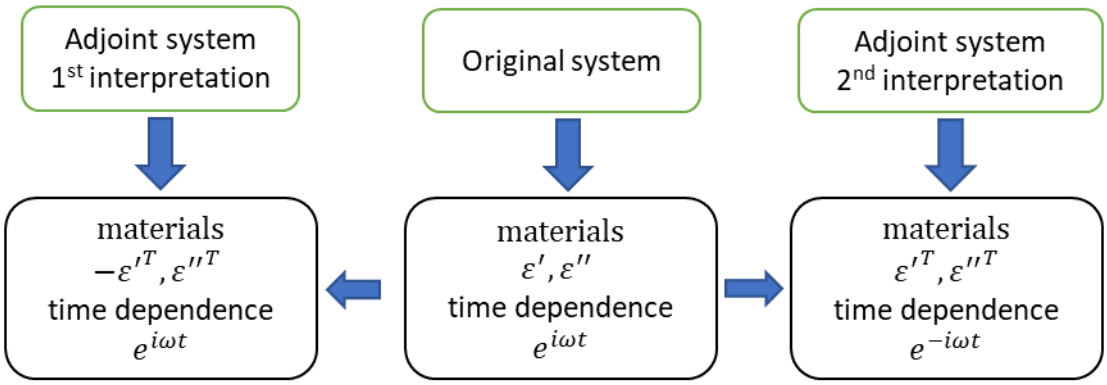

Fig. 2.4 Physical interpretations of the adjoint of Maxwell equations: taking the adjoint switches roles of dielectrics and metals by flipping the real part of the permittivity; or merely transposes the permittivity tensor assuming the complement time dependence. The same happens to permeability as well.

In a typical adjoint optimization algorithm, the adjoint simulation is required. However, flipping real part of permittivity and permeability is not an easy task in simulation and thus complicates the following numerical implementation. A surprisingly straightforward alternative is to look at the

Maxwell's equation using the complement sinusoidal dependence $e^{-i\omega t}$, in which case the Maxwell's equations are formulated as below

$$\begin{pmatrix} i\omega\varepsilon & \nabla\times \\ \nabla\times & -i\omega\mu \end{pmatrix}\begin{pmatrix} \mathbf{E} \\ \mathbf{H} \end{pmatrix} = \begin{pmatrix} \mathbf{J} \\ -\mathbf{M} \end{pmatrix} \quad 2\text{-}44$$

As a result, we can write down the adjoint operator in Equation 2-38 with $\varepsilon^{\dagger} = \bar{\varepsilon}^{T}$ and $\mu^{\dagger} = \bar{\mu}^{T}$. In fact, apart from transposing the tensor matrix, it doesn't change material property at all because changing sinusoidal dependence and taking conjugate cancels each other. In other words, $\varepsilon = \varepsilon' - i\varepsilon''$ in $e^{i\omega t}$ convention is equivalent to $\varepsilon = \varepsilon' + i\varepsilon''$ in $e^{-i\omega t}$ dependence, which is exactly equivalent to taking conjugate of the material properties. Because taking double conjugates equals no operations, the adjoint system is the same as the original system except with transposed permittivity and permeability tensors. In general, transposing material properties is an easy task in simulation.

It should be noted that in general the adjoint of an operator may not be the conjugate transpose of itself when boundary conditions are not homogeneous or lossless. There is an equivalent notion of adjoint boundary condition which is rarely considered in wave propagation problems. For a general treatment of adjoint system of Maxwell's equations, refer to [45]. The discussion of adjoint system of time-domain Maxwell's equations can also be made precise in a similar fashion. We shall dispense with the discussion of time-domain as the focus is in frequency-domain.

2.3 Continuous Sensitivity Analysis

To date, most of the sensitivity analysis in literature is based on the original partial differential equations and a computer implementation is built with a numerical integration and interpolation scheme to translate continuous equations into discrete ones. The continuous sensitivity analysis has the advantage of being straightforward and independent of solver types which allows one to construct the optimization upon a well-established Maxwell's equations simulator (Lumerical FDTD, MEEP FDTD, HFSS FEM). However, careful convergence study must be carried out before the optimization and it is becoming particularly difficult when plasmonic structures are

involved. We will discuss the three difficulties in plasmonic structure optimization at the end of this section.

The most common design variable for topology optimization is the geometry of components, i.e., searching for the best shape that minimizes the objective function. The sensitivity analysis can tell whether the objective function would increase or decrease when changing the geometry by a small amount. We shall start with an intuitive and simple example and then derive a generalization form with the provided abstraction from previous section. The following example follows the procedures described in [50]. Suppose an incident plane wave is coming towards a region in which we can modify geometry (Fig. 2.5). The permittivity and permeability are assumed to be scalars. The objective is to maximize the electric intensity at some point $\boldsymbol{r_0}$, i.e., to maximize $F = 0.5|\mathbf{E}(\boldsymbol{r}_0)|^2$.

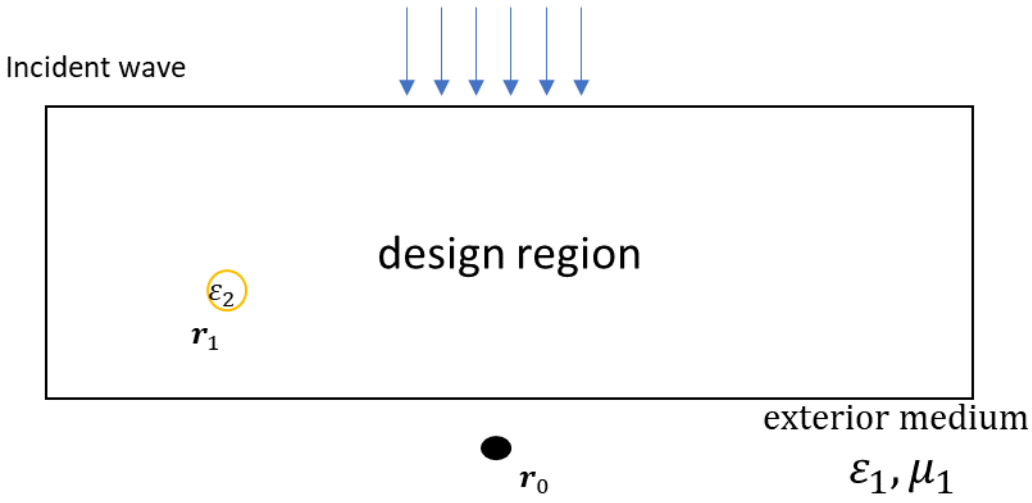

Fig. 2.5 The simple setup. An incident wave is coming towards the design region within which we can tweak the geometry of objects inside. The goal is to maximize field intensity at the point $\boldsymbol{r}_0$ below the design region. A small inclusion with dielectric constant ε_2 introduces a small perturbation to the fields similar to that of a dipole source.

Suppose we introduce a small perturbation to the geometry by placing a small inclusion with dielectric constant ε_2 and volume dV at some point $\boldsymbol{r}_1$. Although general perturbation to the system causes non-linear effects to the objective function, if the perturbation is small enough, we

could linearize the effects. We denote the original electric fields by $\mathbf{E}_{\text{old}}$ and the perturbed electric fields by $\mathbf{E}_{\text{pert}}$. Their difference is denoted by $\delta\mathbf{E} = \mathbf{E}_{\text{pert}} - \mathbf{E}_{\text{old}}$. Assuming the perturbation is small, we can linearize the change in the objective function

$$\begin{aligned}\delta F &= 0.5\left|\mathbf{E}_{\text{pert}}(\boldsymbol{r}_0)\right|^2 - 0.5|\mathbf{E}_{\text{old}}(\boldsymbol{r}_0)|^2 \\ &= \text{Re}\left(\overline{\mathbf{E}_{\text{old}}}(\boldsymbol{r}_0)\cdot\delta\mathbf{E}(\boldsymbol{r}_0)\right)\end{aligned} \tag{2-45}$$

The new inclusion acts as a dipole scatterer in the presence of incident field [51]. Relating the electric field in the sphere in the sea of ε_1 by the Clausius-Mossoti factor, we have the induced dipole current given by

$$\mathbf{J} \cong A(\varepsilon_1, \varepsilon_2)dV\mathbf{E}_{\text{old}}(\boldsymbol{r}_1)\delta(\boldsymbol{r} - \boldsymbol{r}_1) \tag{2-46}$$

where $A(\varepsilon_1, \varepsilon_2) = \frac{3(\varepsilon_2 - \varepsilon_1)}{\varepsilon_2/\varepsilon_1 + 2}$. The delta function is given to emphasize that the current is a point source. This dipole current in turn induced the current difference $\delta\mathbf{E}$. At this point, a brute-force optimization is the obvious candidate: from an initial geometry, test a separate inclusion at every possible $\boldsymbol{r}_1$. Calculate δF for each inclusion and pick the inclusion with the largest δF. Iterate through the same process on the updated geometry until a certain convergence criterion is reached. This method is illustrated in Fig. 2.6. Even in the simplest situation, there are hundreds of places to test inclusion and thus hundreds of simulations are needed in order to go through 1 iteration. This is clearly unrealistic.

This is where the Lorentz Reciprocity enters. Recall that in Equation 2-17 the electric field induced by arbitrary current is equivalent to the convolution between the current and the Green's function

$$\delta\mathbf{E}(\boldsymbol{r}_0) = \iiint_V \mathbf{G}(\boldsymbol{r}_0, \boldsymbol{r})\cdot\mathbf{J}(\boldsymbol{r}) = \mathbf{G}(\boldsymbol{r}_0, \boldsymbol{r_1})\cdot\mathbf{E}_{\text{old}}(\boldsymbol{r}_1)A(\varepsilon_1, \varepsilon_2)dV \tag{2-47}$$

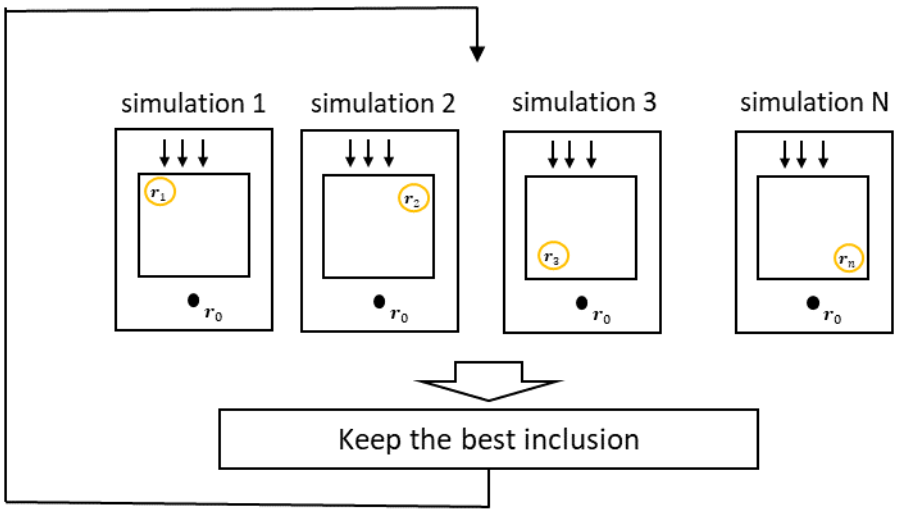

Fig. 2.6 A brute-force optimization method. In each iteration, run simulation for the same number of times as the number of inclusions to determine which inclusion makes the best improvement in the objective function and keep that one.

Substituting the new form into Equation 2-45 and utilizing the Lorentz Reciprocity from Equation 2-19 gives

$$\begin{aligned}\delta F &= \mathrm{Re}\left(\overline{\mathbf{E}_{\mathrm{old}}}(\boldsymbol{r}_0)\cdot\delta\mathbf{E}(\boldsymbol{r}_0)\right)\\ &= \mathrm{Re}\left(A(\varepsilon_1,\varepsilon_2)dV\overline{\mathbf{E}_{\mathrm{old}}}(\boldsymbol{r}_0)\cdot\mathbf{G}(\boldsymbol{r}_0,\boldsymbol{r}_1)\cdot\mathbf{E}_{\mathrm{old}}(\boldsymbol{r}_1)\right)\\ &= \mathrm{Re}\left(A(\varepsilon_1,\varepsilon_2)dV\mathbf{E}_{\mathrm{old}}(\boldsymbol{r}_1)\cdot\mathbf{G}(\boldsymbol{r}_1,\boldsymbol{r}_0)\cdot\overline{\mathbf{E}_{\mathrm{old}}}(\boldsymbol{r}_0)\right)\end{aligned} \tag{2-48}$$

Notice that the last two terms in Equation 2-48, $\mathbf{G}(\boldsymbol{r}_1,\boldsymbol{r}_0)\cdot\overline{\mathbf{E}_{\mathrm{old}}}(\boldsymbol{r}_0)$, are exactly the fields of a dipole driven with amplitude $\overline{\mathbf{E}_{\mathrm{old}}}(\boldsymbol{r}_0)$ at $\boldsymbol{r}_0$ radiating to $\boldsymbol{r}_1$. If we define the adjoint electric field as

$$\mathbf{E}_{\mathrm{a}}(\boldsymbol{r}) = \mathbf{G}(\boldsymbol{r},\boldsymbol{r}_0)\cdot\overline{\mathbf{E}_{\mathrm{old}}}(\boldsymbol{r}_0) \tag{2-49}$$

then we arrive at a simple formula for the variation in the objective function

$$\delta F = \mathrm{Re}\left(\frac{3(\varepsilon_2-\varepsilon_1)}{\varepsilon_2/\varepsilon_1+2}\,dV\mathbf{E}_{\mathrm{old}}(\boldsymbol{r}_1)\cdot\mathbf{E}_{\mathrm{a}}(\boldsymbol{r}_1)\right) \tag{2-50}$$

As a result, exactly one simulation is needed to calculate the adjoint electric field and then by Equation 2-50 we can get δF at everywhere. A new adjoint based optimization is illustrated in Fig. 2.7. First, start with an initial geometry, and simulate the electric field of the structure with incident source. Calculate $\overline{\mathbf{E}_{\mathrm{old}}}(\boldsymbol{r}_0)$ and place a dipole with the same amplitude in the adjoint simulation without the incident source. This second simulation gives the adjoint electric field, with which we can calculate the variation of the objective function for each separate inclusion by Equation 2-50. Now pick the inclusion with the largest δF and update the geometry. Iterate through the same process again on the updated geometry until some convergence criterion is reached. The new adjoint-based method is clearly much less computational than the brute-force method. After all, it only requires two simulation in each iteration.

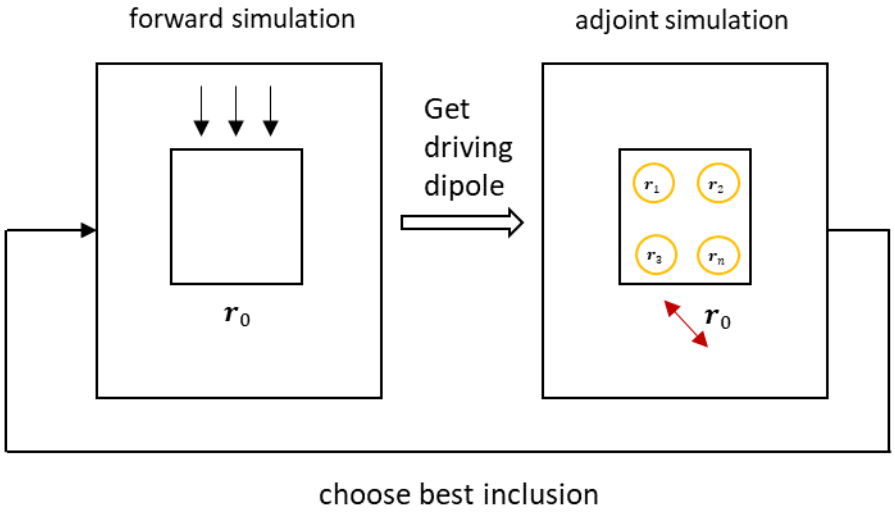

Fig. 2.7 The adjoint optimization approach. First run a forward simulation to get amplitudes of the driving dipole in adjoint simulation. Then run an adjoint simulation and measure electric fields at points of inclusion. Calculate objective function change according to Equation 2-50 for each inclusion and keep the best inclusion.

The example given above is far from any realistic application. A generalization can be derived using the language from previous section. Let's denote the objective function by $F = F(\mathbf{E}) \in \mathbb{R}$. To make sure gradients exist, the objective function is assumed to be differentiable relative to the fields. Differentiable functions like $f = x^2 - xy + z$ have gradient given by $\nabla f = (2x -$

$y, -x, 1)$. But what is the gradient of F which depends on functions instead of variables? The answer to this is another function! A generalized notion of derivative relative to the function is given by the Fréchet derivative which is a derivative defined on Banach spaces [44]. It was already shown that the solution space of Maxwell's equations is indeed a Hilbert space which is Banach by definition. The official definition of Fréchet derivative [52] in Banach space follows:

Let V be a complex Banach space and a function $F: V \to \mathbb{C}$ is called Fréchet differentiable at $x \in V$ if there exists a bounded linear operator $DF_x: V \to \mathbb{C}$ such that

$$\lim_{\|h\| \to 0} \frac{\|F(x+h) - F(x) - DF_x(h)\|}{\|h\|} = 0 \tag{2-51}$$

where we write $DF_x(h)$ to emphasize that the derivative has dependence on x and takes h as the argument. We call DF_x the first order Fréchet derivative. Similarly, we also have second order Fréchet derivative given by

$$\lim_{\|h\| \to 0} \frac{\left\| F(x+h) - F(x) - DF_x(h) - \frac{1}{2} D^2 F_x(h,h) \right\|}{\|h\|^2} = 0 \tag{2-52}$$

where $D^2 F_x$ is a bilinear form. If we replace V with $\mathbb{C}$, then Equation 2-51 becomes the usual notion of complex-valued function being analytical at point x. As a result, a first order approximation of the variation of the objective function F is given by

$$\delta F = F(\mathbf{E} + \delta\mathbf{E}) - F(\mathbf{E}) = DF_{\mathbf{E}}(\delta\mathbf{E}) \tag{2-53}$$

The Fréchet derivative of the objective function for the simple example is given by

$$\begin{aligned} DF_{\mathbf{E}}(\delta\mathbf{E}) &= \mathrm{Re}\left(\bar{\mathbf{E}}(\boldsymbol{r}_0) \cdot \delta\mathbf{E}(\boldsymbol{r}_0)\right) \\ &= \mathrm{Re}\left(\iint \delta\mathbf{E}(\boldsymbol{r}) \cdot \bar{\mathbf{E}}(\boldsymbol{r}) \delta(\boldsymbol{r} - \boldsymbol{r}_0) \right) = \mathrm{Re}\left(\langle \delta\mathbf{E}(\boldsymbol{r}) | \mathbf{E}(\mathbf{r}) \delta(\boldsymbol{r} - \boldsymbol{r}_0) \rangle \right) \end{aligned} \tag{2-54}$$

We denote the second term inside the inner product as

$$\frac{\delta F}{\delta \mathbf{E}} = \mathbf{E}(\mathbf{r})\delta(\boldsymbol{r} - \boldsymbol{r}_0) \tag{2-55}$$

Similarly, if $F = 0.5|\mathbf{H}(\mathbf{r}_0)|^2$ depends on $\mathbf{H}$, we also have

$$\frac{\delta F}{\delta \mathbf{H}} = \mathbf{H}(\mathbf{r})\delta(\boldsymbol{r} - \boldsymbol{r}_0) \tag{2-56}$$

These two functions, $\frac{\delta F}{\delta \mathbf{E}}$ and $\frac{\delta F}{\delta \mathbf{H}}$, are called the gradients of F. Another example is the Poynting flux: $F = \mathrm{Re}\left(\iint_{\partial\Omega} (\mathbf{E} \times \bar{\mathbf{H}}) \cdot \hat{n} dS \right)$. In this case, the Fréchet derivative is given by

$$\begin{aligned} DF_{\mathbf{E},\mathbf{H}}(\delta\mathbf{E}, \delta\mathbf{H}) &= \mathrm{Re}\left(\iint_{\partial\Omega} (\delta\mathbf{E} \times \bar{\mathbf{H}}) \cdot \hat{n} dS + \iint_{\partial\Omega} (\bar{\mathbf{E}} \times \delta\mathbf{H}) \cdot \hat{n} dS \right) \\ &= \mathrm{Re}\left(\iint_{\partial\Omega} \delta\mathbf{E} \cdot (\hat{n} \times \bar{\mathbf{H}}) dS + \iint_{\partial\Omega} (\bar{\mathbf{E}} \times \hat{n}) \cdot \delta\mathbf{H} dS \right) \\ &= \mathrm{Re}(\langle \delta\mathbf{E} | \hat{n} \times \mathbf{H}\, \partial\Omega \rangle + \langle \delta\mathbf{H} | \mathbf{E} \times \hat{n} \partial\Omega \rangle) \end{aligned} \tag{2-57}$$

Similarly, the two gradients are given by

$$\frac{\delta F}{\delta \mathbf{E}} = \hat{n} \times \mathbf{H}\, \partial\Omega \tag{2-58}$$

$$\frac{\delta F}{\delta \mathbf{H}} = \mathbf{E} \times \hat{n}\, \partial\Omega \tag{2-59}$$

It should be noted that in the above equations $\partial\Omega$ is a 2-dimensional surface measure. Loosely, it is a delta function for a surface and its action is reveled through integration: for any continuous function $f(\boldsymbol{r})$, the following is true

$$\iiint_{\mathbb{R}^3} f(\boldsymbol{r}) \partial\Omega(\mathbf{r}) dV = \iint_{\partial\Omega} f(\boldsymbol{r}) dS \tag{2-60}$$

In Maxwell's equations, surface measure is usually used to denote surface quantities like surface currents, surface charge.

To summarize, for any real-valued function F that depends on solutions of the Maxwell's equations, $(\mathbf{E}, \mathbf{H})$, we can write down the first order variation of the objective function in a more compact way

$$\begin{aligned} \delta F = F(\mathbf{E}+\delta\mathbf{E}) - F(\mathbf{E}) &= \mathrm{Re}\left(\left\langle \delta\mathbf{E} \middle| \frac{\delta F}{\delta \mathbf{E}} \right\rangle + \left\langle \delta\mathbf{H} \middle| \frac{\delta F}{\delta \mathbf{H}} \right\rangle\right) \\ &= \mathrm{Re}\left\langle \begin{matrix} \delta\mathbf{E} \\ \delta\mathbf{H} \end{matrix} \middle| \begin{matrix} \frac{\delta F}{\delta \mathbf{E}} \\ \frac{\delta F}{\delta \mathbf{H}} \end{matrix} \right\rangle \end{aligned} \tag{2-61}$$

Here is where the adjoint operator comes in. Suppose we have the adjoint system with currents source specified by $\mathbf{J}_a = \frac{\delta F}{\delta \mathbf{E}}$ and $\mathbf{M}_a = -\frac{\delta F}{\delta \mathbf{H}}$, i.e.,

$$\begin{pmatrix} -i\omega\varepsilon & \nabla\times \\ \nabla\times & i\omega\mu \end{pmatrix}^{\dagger} \begin{pmatrix} \mathbf{E}_a \\ \mathbf{H}_a \end{pmatrix} = \begin{pmatrix} \frac{\delta F}{\delta \mathbf{E}} \\ \frac{\delta F}{\delta \mathbf{H}} \end{pmatrix} \tag{2-62}$$

where $(\mathbf{E}_a, \mathbf{H}_a)$ are the fields generated by $(\mathbf{J}_a, \mathbf{M}_a)$. Substituting the above Equation into Equation 2-61 gives

$$\delta F = \mathrm{Re}\left\langle \begin{matrix} \delta\mathbf{E} \\ \delta\mathbf{H} \end{matrix} \middle| \begin{pmatrix} -i\omega\varepsilon & \nabla\times \\ \nabla\times & i\omega\mu \end{pmatrix}^{\dagger} \begin{pmatrix} \mathbf{E}_a \\ \mathbf{H}_a \end{pmatrix} \right\rangle \tag{2-63}$$

According to the definition of adjoint operator in Equation 2-37, we have

$$\delta F = \mathrm{Re}\left\langle \begin{pmatrix} -i\omega\varepsilon & \nabla\times \\ \nabla\times & i\omega\mu \end{pmatrix} \begin{pmatrix} \delta\mathbf{E} \\ \delta\mathbf{H} \end{pmatrix} \middle| \begin{pmatrix} \mathbf{E}_a \\ \mathbf{H}_a \end{pmatrix} \right\rangle \tag{2-64}$$

Now we introduce the material variation $\delta\varepsilon, \delta\mu$ into the Maxwell's equation and maintain the same current source

$$\begin{pmatrix} -i\omega(\varepsilon+\delta\varepsilon) & \boldsymbol{\nabla}\times \\ \boldsymbol{\nabla}\times & i\omega(\mu+\delta\mu) \end{pmatrix}\begin{pmatrix} \mathbf{E}+\delta\mathbf{E} \\ \mathbf{H}+\delta\mathbf{H} \end{pmatrix} = \begin{pmatrix} \mathbf{J} \\ -\mathbf{M} \end{pmatrix} = \begin{pmatrix} -i\omega\varepsilon & \boldsymbol{\nabla}\times \\ \boldsymbol{\nabla}\times & i\omega\mu \end{pmatrix}\begin{pmatrix} \mathbf{E} \\ \mathbf{H} \end{pmatrix} \tag{2-65}$$

After canceling terms and ignoring second order terms, we have

$$\begin{pmatrix} -i\omega\varepsilon & \boldsymbol{\nabla}\times \\ \boldsymbol{\nabla}\times & i\omega\mu \end{pmatrix}\begin{pmatrix} \delta\mathbf{E} \\ \delta\mathbf{H} \end{pmatrix} = -\begin{pmatrix} -i\omega\delta\varepsilon & \\ & i\omega\delta\mu \end{pmatrix}\begin{pmatrix} \mathbf{E} \\ \mathbf{H} \end{pmatrix} \tag{2-66}$$

Combining Equations 2-64 and 2-66, we arrive at the continuous adjoint sensitivity formula

$$\begin{aligned} \delta F &= \mathrm{Re}\left\langle -\begin{pmatrix} -i\omega\delta\varepsilon & \\ & i\omega\delta\mu \end{pmatrix}\begin{pmatrix} \mathbf{E} \\ \mathbf{H} \end{pmatrix} \middle| \begin{pmatrix} \mathbf{E}_a \\ \mathbf{H}_a \end{pmatrix} \right\rangle \\ &= \mathrm{Re}\left\langle \begin{pmatrix} i\omega\delta\varepsilon\mathbf{E} \\ -i\omega\delta\mu\mathbf{H} \end{pmatrix} \middle| \begin{pmatrix} \mathbf{E}_a \\ \mathbf{H}_a \end{pmatrix} \right\rangle \\ &= \mathrm{Re}\left(\iiint_{\mathbb{R}^3} i\omega\delta\varepsilon\mathbf{E}\cdot\bar{\mathbf{E}}_a dV - \iiint_{\mathbb{R}^3} i\omega\delta\mu\mathbf{H}\cdot\bar{\mathbf{H}}_a dV \right) \end{aligned} \tag{2-67}$$

Let us revisit the simple example. The perturbation of a small inclusion of volume dV at $\boldsymbol{r}_1$ can be approximated by a delta function, i.e.,

$$\delta\varepsilon = dV(\varepsilon_2-\varepsilon_1)\delta(\boldsymbol{r}-\boldsymbol{r}_1) \tag{2-68}$$

Substituting this into Equation 2-67 yields

$$\delta F = \mathrm{Re}\big((\varepsilon_2-\varepsilon_1)\, dV\mathbf{E}_{\mathrm{old}}(\boldsymbol{r}_1)\cdot\bar{\mathbf{E}}_{\mathrm{a}}(\boldsymbol{r}_1)\big) \tag{2-69}$$

Compared with Equation 2-50 which uses Clausius-Mossoti factor, the above formula has two differences: first, $\bar{\mathbf{E}}_{\mathrm{a}}(\boldsymbol{r}_1)$ is used instead of $\mathbf{E}_{\mathrm{a}}(\boldsymbol{r}_1)$; second, there is an extra factor $\frac{3}{\varepsilon_2/\varepsilon_1+2}$ in Equation 2-50. The first difference stems from the fact that Equation 2-69 calculates adjoint fields from adjoint Maxwell's equations while in Equation 2-50 the original Maxwell's equations are

used. When the Lorentz Reciprocity is true, the adjoint fields from Equations 2-50, 2-69 are conjugate of each other and hence are fundamentally the same. The second difference rises from the two different perturbations used in derivations of the two equations. In Equation 2-50 where Clausius-Mossoti factor is used, the geometry is perturbed by an infinitesimal hole, in which case the sensitivity is called the topological derivative [53]. It is valid for high contrast sphere inclusion resulting in high value for $\varepsilon_2 - \varepsilon_1$. Different shapes of inclusion may result in factor different from $\frac{3}{\varepsilon_2/\varepsilon_1+2}$. In contrast Equation 2-69 is called density derivatives and is only valid when $\varepsilon_2 - \varepsilon_1$ is small enough. In a nutshell, topological derivatives predict the change in the objective function with high contrast and spatially small perturbation to the geometry while density derivatives work with low contrast and spatially big perturbation.

In actual implementation, the inclusion shape can be a small rectangular region. Each rectangular region is assigned a pixel value which the permittivity depends on

$$\varepsilon = \varepsilon(\rho), \mu = \mu(\rho), \qquad \rho \in [0,1] \tag{2-70}$$

where $\varepsilon(1) = \varepsilon_2, \varepsilon(0) = \varepsilon_1$ and $\mu(1) = \mu_2, \mu(0) = \mu_1$. This process is referred to as material interpolation [2]. In a typical scenario, $\rho = 1$ indicates that the pixel is occupied by a certain material whereas $\rho = 0$ indicates void. For many applications, the following interpolation scheme is enough [1]

$$\varepsilon(\rho) = \rho\varepsilon_2 + (1-\rho)\varepsilon_1, \qquad \rho \in [0,1] \tag{2-71}$$

The gradient $\frac{\partial F}{\partial \rho}$ is calculated based on Equation 2-69 at each point and a favored non-linear gradient-based optimization algorithm is adopted to solve the optimization problem in Equation 1-1 provided the gradient is given by the continuous adjoint sensitivity analysis. For example, the method of moving asymptotes (MMA) [41], widely used in structural topology optimization, is very efficient in solving optimization problem in the above Equation. This aforementioned approach utilizing conitnuous adjoint sensitivty with a pixelized geometry works reasonably well for dielectric materials where no localized fields are present. However, such optimization scheme

might lead to gray transition regions where ρ lies strictly between 0 and 1. The grey transition regions make it easy to perform an automated post-processing procedure to identify hole shapes and other features by a simple iso-density curve and thresh-holding [36]. Fig. 2.8 illustrates this process. Usually, the post-processed structure has a performance that is very close to the optimized structure. However, in case of plasmonics where localized fields are dominate, simple post-processing based on iso-density and thresh-holding results in a structure with performance that is severely downgraded. Methods to mitigate this issue will be discussed in Chapter 3.

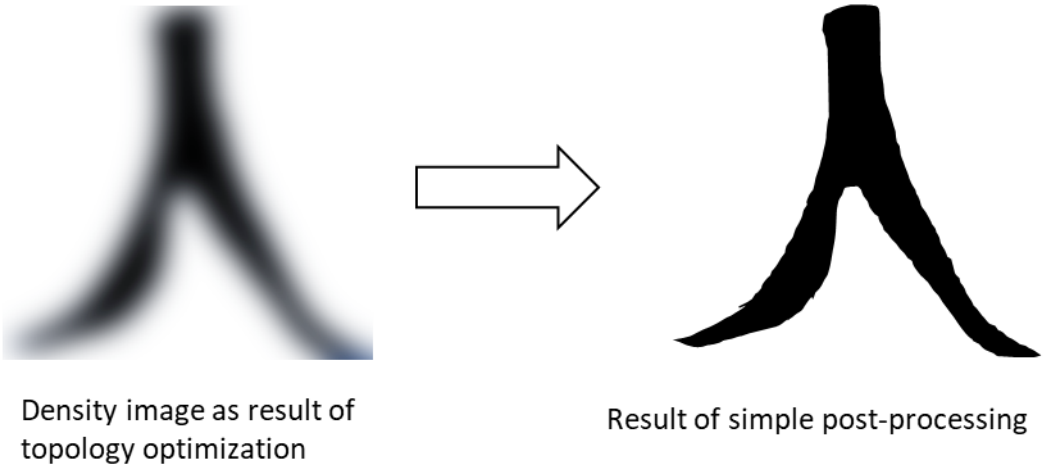

Fig. 2.8 Gray transition regions as a result of density topology optimization. The gray area can be mitigated using iso-density curve which identifies the contours of geometry or thresholding which generates a binary image.

Another issue associated with the continuous sensitivity in highly resonance structure is that some numerical methods tend to be highly inaccurate in regions of localized fields. Especially in the FDTD method, stair-cased material boundary severely hampers the possibility to capture precise surface wave patterns. It was demonstrated that a 0.5nm grid size is necessary to accruately calculate scattering coefficients of Gold sphere of radius 60nm [54]. Hence, finite element method (FEM) is usually the favored tool in topology optimization for their conformal boundary representation and accurate capture of localized fields.

The third issue points at the material interpolation scheme. It was demonstrated that a simple linear interpolation scheme in Equation 2-71 generated non-physical field amplification at intermediate values of ρ [39]. A better interpolation is to linearly interpolate reflected index instead of permittivity

$$\varepsilon(\rho) = \left(\sqrt{\varepsilon_2} + (1-\rho)\sqrt{\varepsilon_1}\right)^2, \qquad \rho \in [0,1] \tag{2-72}$$

Note that this scheme is not easy to implement in FDTD method since dispersion relations are usually specified as summation of couple of Lorentz-Drude poles.

2.4 Discrete Sensitivity Analysis with FDTD

Since the term FDTD was first coined in 1980 by Taflov [55], there are over 10000 results in google scholar published with the keyword FDTD in 2018. The FDTD method is widely used in the analysis of plasmonic structures due to its ability to handle complex structures and materials across wide range of frequency. We will demonstrate a new technique with which the accuracy of adjoint sensitivity is guaranteed without resolving to extremely fine mesh. This technique can be easily incorporated into any FDTD implementation due to its simplicity.

We start with the basic formulation of 3 dimensional FDTD method. In 1966, Yee [56] proposed a set of finite-difference equations for the time-dependent Maxwell's equations

$$\frac{\partial \mathbf{B}}{\partial t} = -\nabla \times \mathbf{E} - \mathbf{M} \tag{2-73}$$

$$\frac{\partial \mathbf{D}}{\partial t} = \nabla \times \mathbf{H} - \mathbf{J} \tag{2-74}$$

for the non-dispersive case. As illustrated in Fig. 2.9, The Yee algorithm centers its E and H components in three-dimensional space so that every E component is surrounded by four circulating H components and every H component is surrounded by four circulating E components.

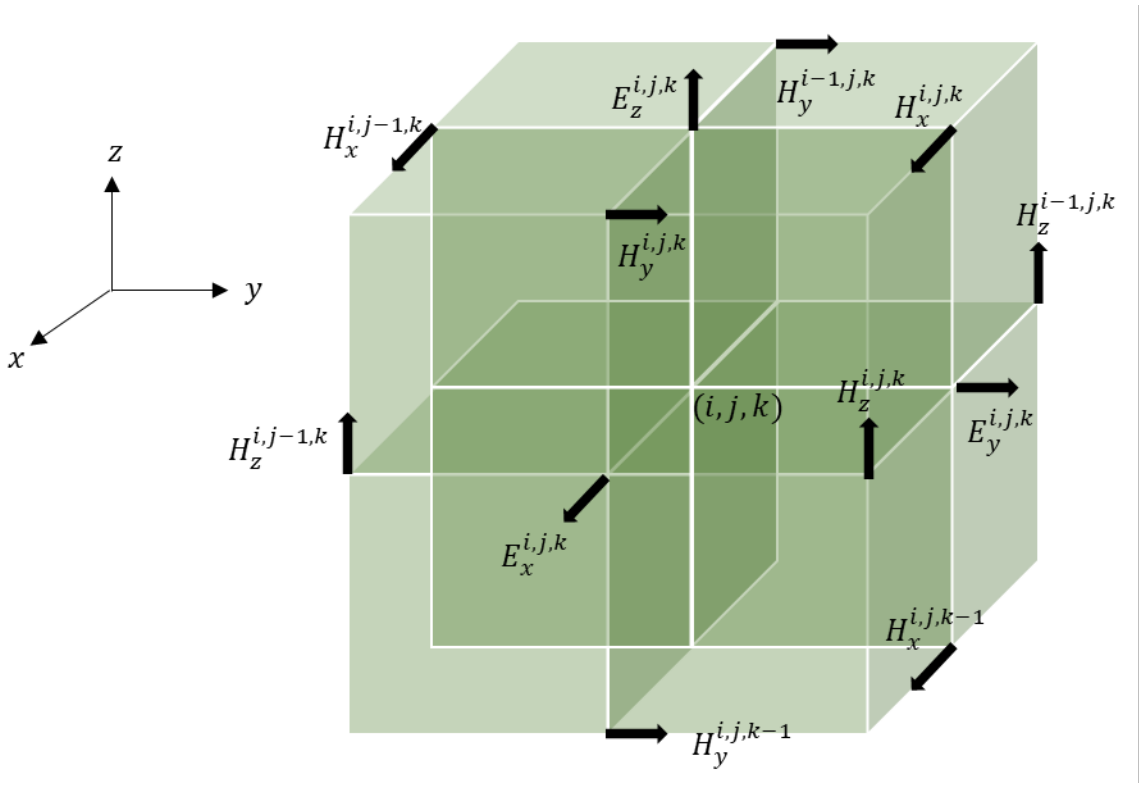

Fig. 2.9 Component arrangement of the Yee cell. Each E component is surrounded by four H components and each H component is surrounded by four E components. There is no component in the corner or center of the cell.

Futhermore, the algorithm centers its E and H components in time, creating a leapfrog arrangement such that E components are evaluated at $n\Delta t$ while H components are evaluated at $(n + 0.5)\Delta t$. For convenience, we index each Yee cell by the position of its lower corner in a rectangular lattice

$$(i,j,k) = (i\Delta x, j\Delta \mathrm{y}, k\Delta \mathrm{z}) \qquad 2\text{-}75$$

and index each electrogmanetic components by index of the cell it belongs to

$$E_x^{i,j,k,n} = E\big((i+0.5)\Delta x, j\Delta y, k\Delta z, n\Delta t\big) \quad 2\text{-}76$$
$$E_y^{i,j,k,n} = E(i\Delta x, (j+0.5)\Delta y, k\Delta z, n\Delta t) \quad 2\text{-}77$$
$$E_z^{i,j,k,n} = E(i\Delta x, j\Delta y, (k+0.5)\Delta z, n\Delta t) \quad 2\text{-}78$$
$$H_x^{i,j,k,n} = E(i\Delta x, (j+0.5)\Delta y, (k+0.5)\Delta z, (n+0.5)\Delta t) \quad 2\text{-}79$$
$$H_y^{i,j,k,n} = E\big((i+0.5)\Delta x, j\Delta y, (k+0.5)\Delta z, (n+0.5)\Delta t\big) \quad 2\text{-}80$$
$$H_z^{i,j,k,n} = E\big((i+0.5)\Delta x, (j+0.5)\Delta y, k\Delta z, (n+0.5)\Delta t\big) \quad 2\text{-}81$$

The Yee's algorithm then evaluates curl and time derivative using central difference scheme. They are given by

$$\frac{B_x^{i,j,k,n} - B_x^{i,j,k,n-1}}{\Delta t} = -\frac{E_z^{i,j+1,k,n} - E_z^{i,j,k,n}}{\Delta y} + \frac{E_y^{i,j,k+1,n} - E_y^{i,j,k,n}}{\Delta \mathrm{z}} - M_x^{i,j,k,n} \quad 2\text{-}82$$
$$\frac{B_y^{i,j,k,n} - B_y^{i,j,k,n-1}}{\Delta t} = -\frac{E_x^{i,j,k+1,n} - E_x^{i,j,k,n}}{\Delta \mathrm{z}} + \frac{E_z^{i+1,j,k,n} - E_z^{i,j,k,n}}{\Delta \mathrm{x}} - M_y^{i,j,k,n} \quad 2\text{-}83$$
$$\frac{B_z^{i,j,k,n} - B_z^{i,j,k,n-1}}{\Delta t} = -\frac{E_y^{i+1,j,k,n} - E_y^{i,j,k,n}}{\Delta \mathrm{x}} + \frac{E_x^{i,j+1,k,n} - E_x^{i,j,k,n}}{\Delta \mathrm{y}} - M_z^{i,j,k,n} \quad 2\text{-}84$$

and

$$\frac{D_x^{i,j,k,n+1} - D_x^{i,j,k,n}}{\Delta t} = \frac{H_z^{i,j,k,n} - H_z^{i,j-1,k,n}}{\Delta y} - \frac{H_y^{i,j,k,n} - H_y^{i,j,k-1,n}}{\Delta \mathrm{z}} - J_x^{i,j,k,n} \quad 2\text{-}85$$
$$\frac{D_y^{i,j,k,n+1} - D_y^{i,j,k,n}}{\Delta t} = \frac{H_x^{i,j,k,n} - H_x^{i,j,k-1,n}}{\Delta \mathrm{z}} - \frac{H_z^{i,j,k,n} - H_z^{i-1,j,k,n}}{\Delta \mathrm{x}} - J_y^{i,j,k,n} \quad 2\text{-}86$$
$$\frac{D_z^{i,j,k,n+1} - D_z^{i,j,k,n}}{\Delta t} = \frac{H_y^{i,j,k,n} - H_y^{i-1,j,k,n}}{\Delta \mathrm{x}} - \frac{H_x^{i,j,k,n} - H_x^{i,j-1,k,n}}{\Delta \mathrm{y}} - J_z^{i,j,k,n} \quad 2\text{-}87$$

Collecting components for each grid cell in column vectors gives

$$\frac{d^{n+1} - d^n}{\Delta t} = \mathbf{C}_h h^n - j^n \quad 2\text{-}88$$
$$\frac{b^n - b^{n-1}}{\Delta t} = -\mathbf{C}_e e^n - m^n \quad 2\text{-}89$$

where

$$d^n = \begin{pmatrix} \vdots \\ D_x^{i,j,k,n} \\ D_y^{i,j,k,n} \\ D_z^{i,j,k,n} \\ \vdots \end{pmatrix}, h^n = \begin{pmatrix} \vdots \\ H_x^{i,j,k,n} \\ H_y^{i,j,k,n} \\ H_z^{i,j,k,n} \\ \vdots \end{pmatrix}, j^n = \begin{pmatrix} \vdots \\ J_x^{i,j,k,n} \\ J_y^{i,j,k,n} \\ J_z^{i,j,k,n} \\ \vdots \end{pmatrix} \quad \text{2-90}$$

and

$$b^n = \begin{pmatrix} \vdots \\ B_x^{i,j,k,n} \\ B_y^{i,j,k,n} \\ B_z^{i,j,k,n} \\ \vdots \end{pmatrix}, e^n = \begin{pmatrix} \vdots \\ H_x^{i,j,k,n} \\ H_y^{i,j,k,n} \\ H_z^{i,j,k,n} \\ \vdots \end{pmatrix}, m^n = \begin{pmatrix} \vdots \\ M_x^{i,j,k,n} \\ M_y^{i,j,k,n} \\ M_z^{i,j,k,n} \\ \vdots \end{pmatrix} \quad \text{2-91}$$

are column vectors representing the relevant fields; $\mathbf{C}_h$, whose nonzero elements are $\pm 1/\Delta x$, $\pm 1/\Delta y$ and $\pm 1/\Delta z$, is a matrix for the curl operator on the *H* components while $\mathbf{C}_e$ is a matrix for the curl operator on the *E* components.

It should be noted each vector has countably many components and belong to the square summable space ℓ^2 due to its continuous counterpart in which fields decay in a square integrable way [48]. A sequence $x = \{x_i\}_{i=1}^{\infty}$ belongs to ℓ^2 if it is square summable

$$\|x\|_2 = \sum_n \|x_n\|^2 < \infty \quad \text{2-92}$$

It is well-known that ℓ^2 is a Hilbert space which enables us to use the tool from the adjoint operator theory. Frequency domain analysis in FDTD is carried out through discrete-time fourier transform (DTFT) of electrogmanetic components

$$\tilde{x}\left(e^{i\omega\Delta t}\right) = \sum_{n=0}^{\infty} x[n] e^{-i\omega n\Delta t} \quad \text{2-93}$$

where ω is frequency of interest and Δt is the discretized time step. For convenience, let $z = e^{i\omega\Delta t}$, then the DTFT becomes a special case of z-transform[2] [26]

$$\tilde{x}(z) = \sum_{n=0}^{\infty} x[n] z^{-n} \tag{2-94}$$

Taking DTFT of both sides of Equation 2-88 and 2-89 yields

$$\frac{z\tilde{d}(z) - \tilde{d}(z)}{\Delta t} = \mathbf{C}_h \tilde{h}(\mathrm{z}) - \tilde{j}(\mathrm{z}) \tag{2-95}$$

$$\frac{\tilde{b}(\mathrm{z}) - z^{-1}\tilde{b}(z)}{\Delta t} = -\mathbf{C}_e \tilde{e}(\mathrm{z}) - \tilde{m}(z) \tag{2-96}$$

For small enough Δt, substituting $z = e^{i\omega\Delta t} \cong 1 + i\omega\Delta t$ and $z^{-1} = e^{-i\omega\Delta t} \cong 1 - i\omega\Delta t$ into the above Equations gives

$$i\omega\tilde{d}(\mathrm{z}) = \mathbf{C}_h \tilde{h}(\mathrm{z}) - \tilde{j}(\mathrm{z}) \tag{2-97}$$

$$i\omega\tilde{b}(\mathrm{z}) = -\mathbf{C}_e \tilde{e}(\mathrm{z}) - \tilde{m}(z) \tag{2-98}$$

The consitute equations in time-domian for isotropic linearly disperisve materials are given by

$$\mathbf{D} = \varepsilon_\infty \mathbf{E} + \sum_i \chi_{e,i} * \mathbf{E} = \varepsilon_\infty \mathbf{E} + \sum_i \mathbf{P}_{e,i} \tag{2-99}$$

$$\mathbf{B} = \mu_\infty \mathbf{H} + \sum_i \chi_{h,i} * \mathbf{H} = \mu_\infty \mathbf{H} + \sum_i \mathbf{P}_{h,i} \tag{2-100}$$

Where $\chi_{e,i}$ and $\chi_{h,i}$ are electric and magnetic susceptibility respectively. To avoid handling the computationally expensive convolution, the FDTD algorithm usually converts convolution into discretized recursive equations which rely on limited number of terms in each update. A popular method based on the auxiliary differential equation (ADE) technique [57] convert the most general form of dispersion, the Lorentzian form

[2] variables with tilde denote DTFT (z-transform) of the corresponding variables

$$P(\omega) = \frac{a}{b + ic\omega - d\omega^2} E(\omega) = \chi(\omega) E(\omega) \tag{2-101}$$

into discretized recursive equation

$$P^n = C_1 P^{n-1} + C_2 P^{n-2} + C_3 E^{n-1} \tag{2-102}$$

Applying DTFT to Equation 2-102 gives

$$\tilde{p}(z) = \frac{z^{-1}}{1 - C_1 z^{-1} + C_2 z^{-2}} \tilde{e} = \tilde{\chi}(z) \tilde{e}(z) \tag{2-103}$$

It is demonstrated through numerical experiments that the digital susceptibility $\tilde{\chi}(z)$ is found to be almost the same as the continuous one $\chi(\omega)$ for typical ranges of Δt used in simulation. At last, the update equation for the electric field intensity is given by

$$E^n = \frac{D^n - \sum_i P_i^n}{\varepsilon_\infty} \tag{2-104}$$

which is again applied with DTFT

$$\tilde{e}(z) = \frac{\tilde{d}(z) - \sum_i \tilde{p}_i(z)}{\varepsilon_\infty} \tag{2-105}$$

Combining Equations 2-103 and 2-105, we have

$$\tilde{d}(z) = \left(\varepsilon_\infty + \sum_i \tilde{\chi}_i(z) \right) \tilde{e}(z) = \tilde{\varepsilon}(z) \tilde{e}(z) \tag{2-106}$$

Similarly for the magnetic field intensity, we have

$$\tilde{b}(z) = \tilde{\mu}(z)\tilde{e}(z) \tag{2-107}$$

No matter what implementation is adopted to model the linear dispersion, the resulted difference equation can always be turned into a function in the z-plane through z-transform. Then the digital permittivity and permeability $\tilde{\varepsilon}(z)$ and $\tilde{\mu}(z)$ can be evaluated by letting $z = e^{i\omega\Delta t}$ for a given frequency and a time step. Rewriting Equations 2-106 and 2-107 using matrix-vector form yields

$$\tilde{d}(\mathrm{z}) = D_e(z)\tilde{e}(z) \tag{2-108}$$
$$\tilde{b}(z) = D_h(z)\tilde{h}(z) \tag{2-109}$$

where $D_e(z)$ and $D_h(z)$ are diagonal matrix for isotropic materials. Combinging Equations 2-108, 2-109, 2-97 and 2-98, we have

$$\begin{pmatrix} -i\omega D_e(z) & \mathbf{C}_h \\ \mathbf{C}_e & i\omega D_h(z) \end{pmatrix} \begin{pmatrix} \tilde{e}(z) \\ \tilde{h}(z) \end{pmatrix} = \begin{pmatrix} \tilde{\jmath}(z) \\ -\tilde{m}(z) \end{pmatrix} \tag{2-110}$$

We claim that for isotropic materials, the operator in the above equation is symmetric. Obviously, $D_e(z)$ and $D_h(z)$ are symmetric since they are diagonal matrices. Therefore, we only need to shown $\mathbf{C}_e^T = \mathbf{C}_h$. The magic comes with the index system we introduce in Equation 2-75. For each electromagnetic component in the Yee lattice, we associate it with an index $n_w^{i,j,k} \in \mathbb{N}$. Components in the same Yee cell with the same direction share the same space index. For instance, $D_x^{i,j,k,n}$ share the same index as $B_x^{i,j,k,n}$. Then we arrange elements in the column vectors $\tilde{e}(z), \tilde{h}(z), \tilde{\jmath}(z), \tilde{m}(z)$ according to this index. The index system is illustrated in Fig. 2.10.

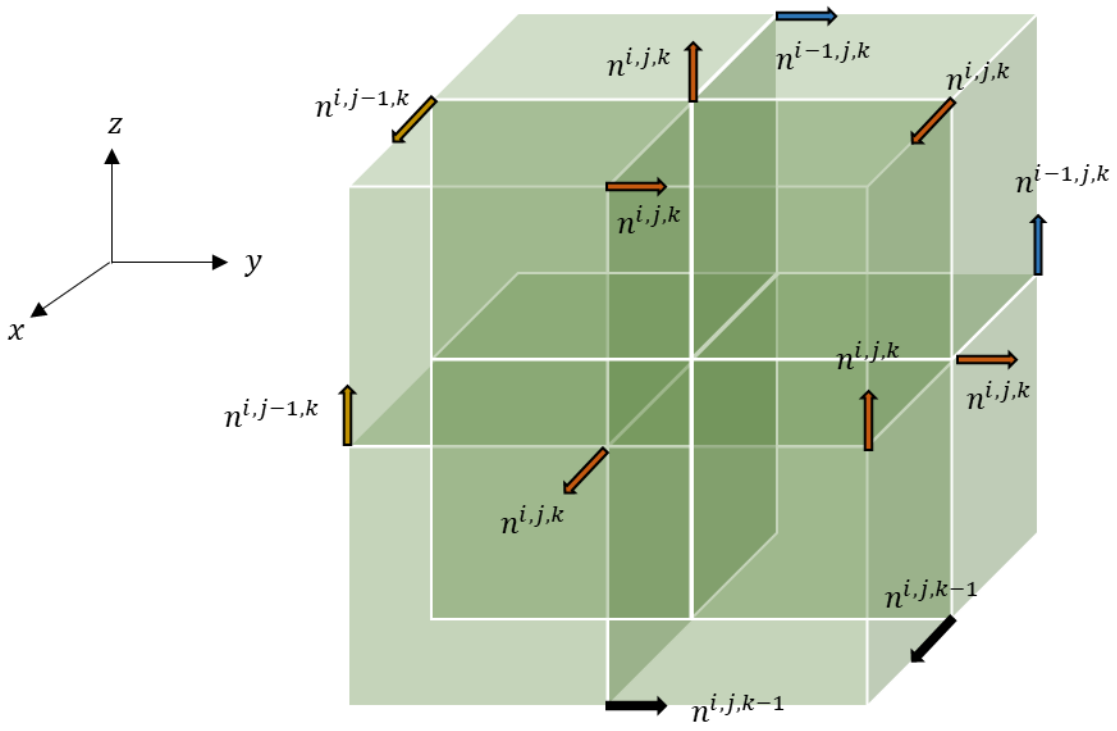

Fig. 2.10 Index system to arrange elements for the column vectors $\tilde{e}(z), \tilde{h}(z), \tilde{j}(z), \tilde{m}(z)$. Each component in the same Yee cell shares the same index. Components in the same color are in the same Yee cell.

In this new index system, each entry of matrix is specified by a pair of tuples of 4 numbers, (x_1, i_1, j_1, k_1) and $(x_2, i_2, j_2, k_2)$where x_1, x_2 can take on valules from $\{x, y, z\}$

$$\mathbf{C}_h\left(n_{x_1}^{i_1,j_1,k_1}, n_{x_2}^{i_2,j_2,k_2}\right) \tag{2-111}$$

With this notation, $\mathbf{C}_e^T = \mathbf{C}_h$ is equivalent to

$$\mathbf{C}_e\left(n_{x_2}^{i_2,j_2,k_2}, n_{x_1}^{i_1,j_1,k_1}\right) = \mathbf{C}_h\left(n_{x_1}^{i_1,j_1,k_1}, n_{x_2}^{i_2,j_2,k_2}\right) \tag{2-112}$$
$$\forall (x_1, i_1, j_1, k_1), (x_2, i_2, j_2, k_2) \in \{x, y, z\} \times \mathbb{Z}^3$$

which is a direct rearrangement of Equations 2-82 to 2-87. We write down entries equal to $1/\Delta y$ to illustrate this behavior

$$1/\Delta y = \mathbf{C}_e\left(n_x^{i_1,j_1,k_1}, n_z^{i_1,j_1+1,k_1}\right) = \mathbf{C}_h\left(n_z^{i_2,j_2,k_2}, n_x^{i_2,j_2-1,k_2}\right) \quad 2\text{-}113$$

$$= -\mathbf{C}_e\left(n_x^{i_1,j_1,k_1}, n_z^{i_1,j_1,k_1}\right) = -\mathbf{C}_h\left(n_z^{i_2,j_2,k_2}, n_x^{i_2,j_2,k_2}\right) \quad 2\text{-}114$$

$$= -\mathbf{C}_e\left(n_z^{i_1,j_1,k_1}, n_x^{i_1,j_1+1,k_1}\right) = -\mathbf{C}_h\left(n_x^{i_2,j_2,k_2}, n_z^{i_2,j_2-1,k_2}\right) \quad 2\text{-}115$$

$$= \mathbf{C}_e\left(n_z^{i_1,j_1,k_1}, n_x^{i_1,j_1,k_1}\right) = \mathbf{C}_h\left(n_x^{i_2,j_2,k_2}, n_z^{i_2,j_2,k_2}\right) \quad 2\text{-}116$$

$$\forall (i_1, j_1, k_1), (i_2, j_2, k_2) \in \mathbb{Z}^3$$

The operator in discretized FDTD system in frequency domain being symmetric is the discrete version of the Lorentz recirpocity. It should be noted that the FDTD system we introduced has an infinite domain while in practice an absorber is placed around a finite region to absorb any outgoing waves or a homogeneous boundary condition like PEC is used to terminate the domain.

The objective function $F(\mathbf{E}, \mathbf{H})$ needs to be discretized with a favored numerical interpolation and integration scheme. Denote the discretized objective function by $f\left(\tilde{e}, \tilde{h}\right) \in \mathbb{R}$. Then the variation of f is given by

$$\delta f = \delta\tilde{e}(z) \cdot \overline{\nabla_e f} + \delta\tilde{h}(z) \cdot \overline{\nabla_h f} \quad 2\text{-}117$$

We can follow the exact same procedures from Equation 2-61 to 2-67 and arrivate at a formula similar to Equation 2-64

$$\delta f = \mathrm{Re}\left\langle -\begin{pmatrix} -i\omega\delta D_e(z) & \\ & i\omega\delta D_h(z) \end{pmatrix}\begin{pmatrix}\tilde{e}(z)\\ \tilde{h}(z)\end{pmatrix} \middle| \begin{pmatrix}\tilde{e}_a(z)\\ \tilde{h}_a(z)\end{pmatrix}\right\rangle \quad 2\text{-}118$$

where $\left(\tilde{e}_a(z), \tilde{h}_a(z)\right)$ are the adjoint currents satisfying

$$\begin{pmatrix} -i\omega D_e(z) & \mathbf{C}_h \\ \mathbf{C}_e & i\omega D_h(z) \end{pmatrix}^{\dagger}\begin{pmatrix}\tilde{e}_a(z)\\ \tilde{h}_a(z)\end{pmatrix} = \begin{pmatrix}\nabla_e F\\ \nabla_h F\end{pmatrix} \quad 2\text{-}119$$

Noticing that $\delta D_e(z)$ and $\delta D_h(z)$ are diagonal matrix, we expand Equation 2-118 into

$$\delta f = \mathrm{Re}\left(\sum_{w,i,j,k} i\omega \tilde{E}_w^{i,j,k}(z) \bar{\tilde{E}}_{a_w}^{\,i,j,k}(z) \delta\varepsilon_w^{i,j,k} - i\omega \tilde{H}_w^{i,j,k}(z) \bar{\tilde{H}}_{a_w}^{\,i,j,k}(z) \delta\mu_w^{i,j,k} \right) \quad 2\text{-}120$$

A striking similarity can be spotted right away between the discrete version of adjoint sensitivty in the above Equation and the continuous version in Equation 2-67. This comes as no surprise since both are originally inner products of its revelent Hilbert space. Obviously, this Equation is also suited for diagonal permittivities and permeabilities. A more sophisticated adjoint sensitivity is possible for general anisotropic materials and is dependent on numerical implementation of anisotropic materials.

We have shown the discrete adjoint sensitivity formula for a open region problem with isotropic materials and uniform grid. The formula is also suited for any finite region problem with lossless homogeneous boundary conditions. Extensions can be made to include anisotropic materials, non-uniform grid and lossy boundary conditions.

2.5 Numerical Implementation

Implementaiton of adjoint sensitivity analysis requires the setup of the adjoint Maxwell's equations. It was already shown that for symmetric permittivities and permeabilities the adjoint system is the same as the original system with the complement sinuosuidal dependence. A close look at the discrete sensitivity Equation 2-120 and the continuos sensitivity Equation 2-67 reveals that we only need to know the complex conjugate of the adjoint fields, i.e., $(\bar{\mathbf{E}}_a, \bar{\mathbf{H}}_a)$ and $\left(\bar{\tilde{E}}_{a_w}^{\,i,j,k}, \bar{\tilde{H}}_{a_w}^{\,i,j,k}\right)$. Instead of using the complement sinuosuidal dependence, we can keep the original dependence and directly solve the conjugate of adjoint fields. Taking conjugates of both sides of Equation 2-120 leads to

$$\begin{pmatrix} -i\omega D_e(z) & \mathbf{C}_h \\ \mathbf{C}_e & i\omega D_h(z) \end{pmatrix} \begin{pmatrix} \bar{\tilde{e}}_a(z) \\ \bar{\tilde{h}}_a(z) \end{pmatrix} = \begin{pmatrix} \overline{\nabla_e f} \\ \overline{\nabla_h f} \end{pmatrix} \quad 2\text{-}121$$

In this formula, the Maxwell's operator remains the same while the adjoint currents are conjugated. Therefore, we can apply the conjugated adjoint currents to the same Maxwell's equtions and derive the conjugated adjoint fields. The same is true with the continuous formula.

Next, to solve the adjoint currents, the objective function needs to be written explicitly with arguments from vectors $\tilde{e}(z)$ and $\tilde{h}(z)$ with respect to which the derivatives can be calculated. In practice, the objective function is always calculated based on fields interpolated from the original electromagnetic fields at the Yee cell. To simplify notation, let's assume that the objective function only depends on electric field $\tilde{e}(z)$. Denote the interpolated electric fields by

$$\hat{\tilde{e}}(\mathrm{z}) = \begin{pmatrix} \hat{\tilde{E}}_1(z) \\ \hat{\tilde{E}}_2(z) \\ \vdots \\ \hat{\tilde{E}}_n(z) \end{pmatrix} \tag{2-122}$$

Assuming linear interpolation, each interpolated electric field is given by[3]

$$\hat{\tilde{E}}_i = \sum_{j \in N_i} w_{ij} \tilde{E}_j \tag{2-123}$$

where N_i is the neighboring element for each interpolated electric field and w_{ij} is the linear interpolation weight for the ith point from its jth neighbor [58]. By chain rule, we have the derivative of objective function given by

$$\frac{\partial f}{\partial \tilde{E}_i(z)} = \sum_{i \in N_j} \frac{\partial f}{\partial \hat{\tilde{E}}_j(z)} w_{ji} \tag{2-124}$$

where $\frac{\partial f}{\partial \hat{\tilde{E}}_j(z)}$ on the right-hand side can be given an analytic form depending on the user-defined formula of objective function. Mathematically, the above Equation exhibits a well-known conecpt

[3] We discard the original index system $E_x^{i,j,k,n}$ to avoid cluttered scripts

originating in multi-grid methods – the transpose of interpolation – and is directly implemented in the Meep FDTD package [59]. This is illustrated in a 2D example in Fig. 2.11.

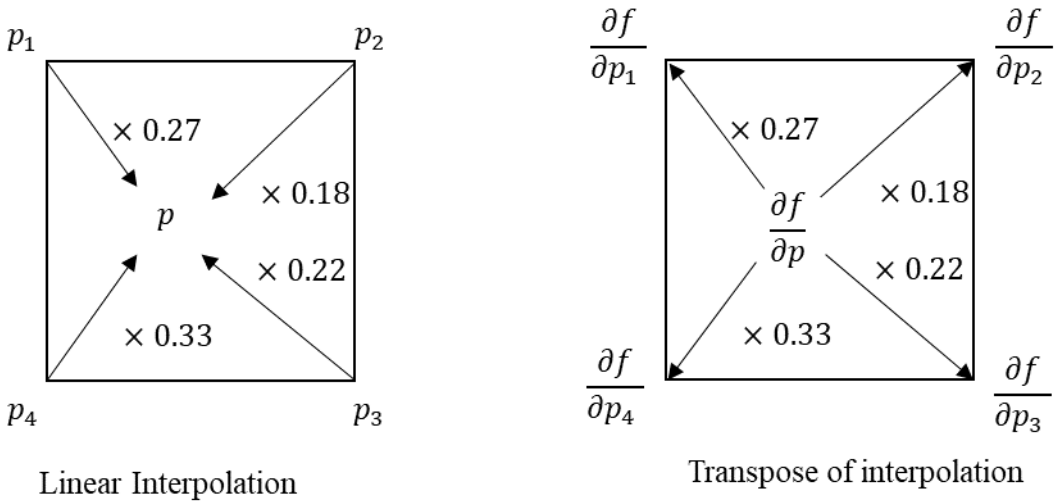

Fig. 2.11 Transpose of bilinear interpolation. The transpose of interpolation assigns values backwards to the points in the lattice. For any function $f(x)$ where $x = Ay$, a direct application of chain rule shows that $\frac{\partial f}{\partial y} = A^T \frac{\partial f}{\partial x}$. Therefore, it is called transpose of interpolation.

After obtaining the adjoint currents, adjoint fields are obtained and sensitivity can be calculated according to Equation 2-120. However, Equation 2-120 is not directly usable for optimization and we need a real-valued variable to represent the material properties. We can assign each material component in the Yee cell two density parameters, $p_w^{i,j,k}$ and $q_w^{i,j,k}$, to interpolate permittivities and permeabilities respectively

$$\varepsilon_w^{i,j,k} = \varepsilon\left(p_w^{i,j,k}\right), \qquad \mu_w^{i,j,k} = \mu\left(q_w^{i,j,k}\right) \tag{2-125}$$

For our purpose, we use either the linear material interpolation in Equation 2-71 or the non-linear material interpolation in Equation 2-72. The sensitivities with respect to the density parameters $p_w^{i,j,k}$ and $q_w^{i,j,k}$ are given by

$$\frac{\partial f}{\partial p_w^{i,j,k}} = \mathrm{Re}\left(i\omega \tilde{E}_w^{i,j,k}(z) \tilde{\bar{E}}_{a_w}^{\,i,j,k}(z) \frac{\partial \varepsilon_w^{i,j,k}}{\partial p_w^{i,j,k}} \right) \quad 2\text{-}126$$

$$\frac{\partial f}{\partial q_w^{i,j,k}} = \mathrm{Re}\left(-i\omega \tilde{H}_w^{i,j,k}(z) \tilde{\bar{H}}_{a_w}^{\,i,j,k}(z) \frac{\partial \mu_w^{i,j,k}}{\partial p_w^{i,j,k}} \right) \quad 2\text{-}127$$

In a density-based optimization [2] approach, $p_w^{i,j,k}$ and $q_w^{i,j,k}$ are further interpolated from density variables ρ's at a rectangular lattice. Assuming a linear interpolation for $p_w^{i,j,k}$ and $q_w^{i,j,k}$, we can transpose $\frac{\partial f}{\partial p_w^{i,j,k}}$ and $\frac{\partial f}{\partial q_w^{i,j,k}}$ to $\frac{\partial f}{\partial \rho}$ following a similar fasion in Equation 2-124. Even for level-set based optimization [60], we can still employ a density variable for each point in the Yee lattice if density mapping is used. To ensure accurate evaluation of adjoint sensitivity from Equations 2-126 and 2-127, both forward and adjoint simulations run until DTFT of fields inside the design region change less than 0.5% over a fixed span of time t_{check} after the input sources turned off. If the change is more than 0.5%, check again in the next t_{check} time. Iterate this until the change is within the limit. Our experiments show that a good estimate for t_{check} is given by

$$t_{check} = \frac{4}{f_{source}} \quad 2\text{-}128$$

where f_{source} is the center frequency of the input source which can be chosen from the Gaussian function or the derivatives of the Gaussian function.

To implement the non-linear material interpolation in the FDTD method, we need to match the permittivity at each individual density ρ. Take gold at 800 nm for example. Since a complex number is in fact a two-dimensional vector, we pick two susceptibility out of the LD4 model [61] and modify their intensity to yield an accurate value for permittivity. Supposing the two susceptibility are given by $\chi_1' - i\chi_2'', \chi_2' - i\chi_2'' \in \mathbb{C}$ and their intensities are $\sigma_1, \sigma_2 \in \mathbb{R}$ respectively, we can calculate the intensities by solving the linear Equations below:

$$\varepsilon'(\rho) = \varepsilon_\infty + \sigma_1\chi_1' + \sigma_2\chi_2' \quad 2\text{-}129$$

$$\varepsilon''(\rho) = \sigma_1\chi_2'' + \sigma_2\chi_2'' \quad 2\text{-}130$$

$$\varepsilon(\rho) = \varepsilon'(\rho) - i\varepsilon''(\rho) \quad 2\text{-}131$$

where ε_∞ is the instantaneous dielectric constant (must be positive). We fix ε_∞ to be 1 and calculate σ_1, σ_2 versus ρ using the non-linear interpolation scheme for gold at 800 nm (Fig. 2.12). Notice that this method only works for single frequency and does not generally guarantee to work for every material. It works for gold at 800nm, which is enough for our own purpose.

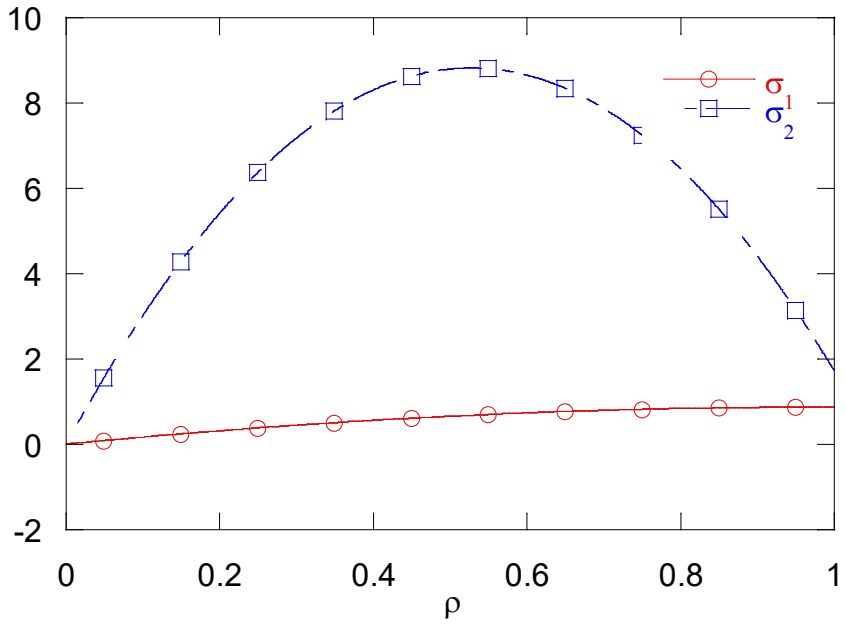

Fig. 2.12 Susceptibility intensity for non-linear material interpolation scheme. Non-linear dependence of the intensity can be observed.

We end up writing our own FDTD solver because we need to control what interpolation scheme goes into the algorithm and to access each individual field component in the Yee lattice. Nevertheless, it is not hard to incorporate the discrete adjoint sensitivity scheme into any existing FDTD software for it only requires the developers to implement transpose of interpolation which is almost the same as the interpolation.

2.6 Example: Absorption of a Block with Varying Permittivity

First, we demonstrate the accuracy of sensitivity for a function measuring the absorption of a scatterer. The measure of absorption is usullay the integral of Poynting flux over a specified region

$$f = \int_S \mathrm{Re}(\mathbf{E} \times \bar{\mathbf{H}}) \cdot \hat{n} dS \tag{2-132}$$

Numerically integrating the above Equation yields

$$f = \sum_i \mathrm{Re}\left(a_i E_x(r_i)\bar{H}_y(r_i) + b_i E_y(r_i)\bar{H}_z(r_i) + c_i E_z(r_i)\bar{H}_x(r_i)\right) \tag{2-133}$$

where constants (a_i, b_i, c_i) are weighting parameters used in numerical integration. We use rectangle rule [58] for numerical integration for its simlicity. The derivatives with respect to electric fields are given by

$$\frac{\partial f}{\partial E_x(r_i)} = a_i H_y(r_i) \tag{2-134}$$

$$\frac{\partial f}{\partial E_y(r_i)} = b_i H_z(r_i) \tag{2-135}$$

$$\frac{\partial f}{\partial E_z(r_i)} = c_i H_x(r_i) \tag{2-136}$$

and derivatievs with respect to magnetic fields are given by

$$\frac{\partial f}{\partial H_x(r_i)} = c_i E_z(r_i) \tag{2-137}$$

$$\frac{\partial f}{\partial H_y(r_i)} = a_i H_x(r_i) \tag{2-138}$$

$$\frac{\partial f}{\partial H_z(r_i)} = b_i H_y(r_i) \tag{2-139}$$

And then they are transposed back into adjoint currents $(\nabla_e f, \nabla_h f)$ using Equation 2-124.

We begin with a simple geometry, a block with a size of $30 \times 30 \times 30$ nm^3. The block has spatially uniform permittivity controlled by a density parameter using linear interpolation

$$\varepsilon(\rho) = \varepsilon_1 \rho + \varepsilon_2 (1 - \rho) \qquad 2\text{-}140$$

where ε_1 is permittivity for gold and ε_2 is permittivity for vacuum. The absorption is calculated by integrating the Poynting flux over a box enclosing the object. A plane wave of wavelength 800nm is incident upon the block. The layout for the example is shown in Fig. 2.13.

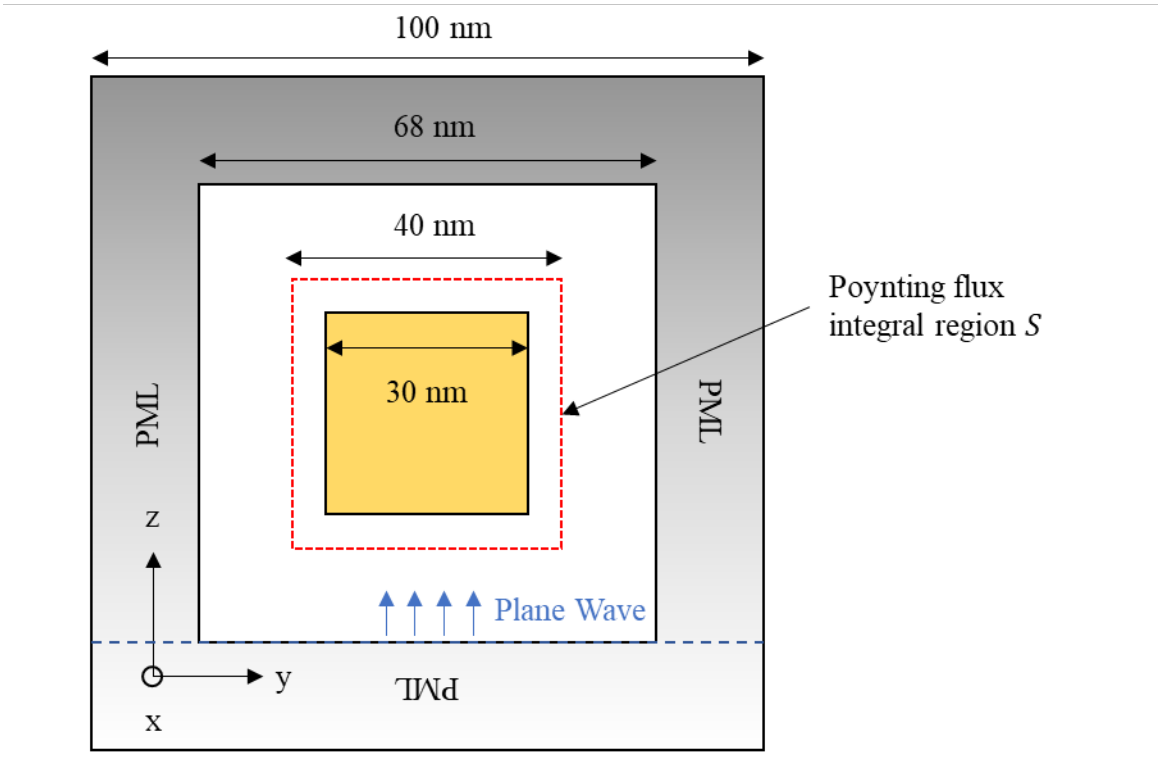

Fig. 2.13 Layout for the first example. A box of size $30 \times 30 \times 30$ nm^3 is seated in an open region with its axis aligned with coordinates. An incident plane wave travels in the z^+ direction. PML layers of 8-cell thickness is used to absorb any outgoing waves. Absorption is calculated on the box surrounding the block.

We took the LD4 model [61] as dispersion model of gold given below

$$\varepsilon_r(\omega) = 1 - \frac{\Omega_p^2}{\omega(\omega - i\Gamma_0)} + \sum_{k=1}^{4} \frac{f_k \omega_p^2}{(\omega_k^2 - \omega^2) + i\omega\Gamma_k} \quad \text{2-141}$$

where ω_p is the plasma frequency, f_k is the strength of the k^{th} oscillator with frequency ω_k and lifetime $1/\Gamma_k$ describing the interband part of the dielectric function, while Ω_p is the plasma frequency associated with intraband transitions with damping constant Γ_0. We linearly scale the intensity of each susceptibility to implement the varying permittivity in Equation 2-140. At 800nm, the permittivity of gold is $\varepsilon_1 = \varepsilon_0(-22.3 - 2.03j)$ calculated from the LD4 model. We use a 2 nm Yee cell length to run forward simulations to calculate the absorption versus the density parameter ρ and run adjoint simulations to get the sensitivity with respect to ρ. Result of the absorption is shown in Fig. 2.14.

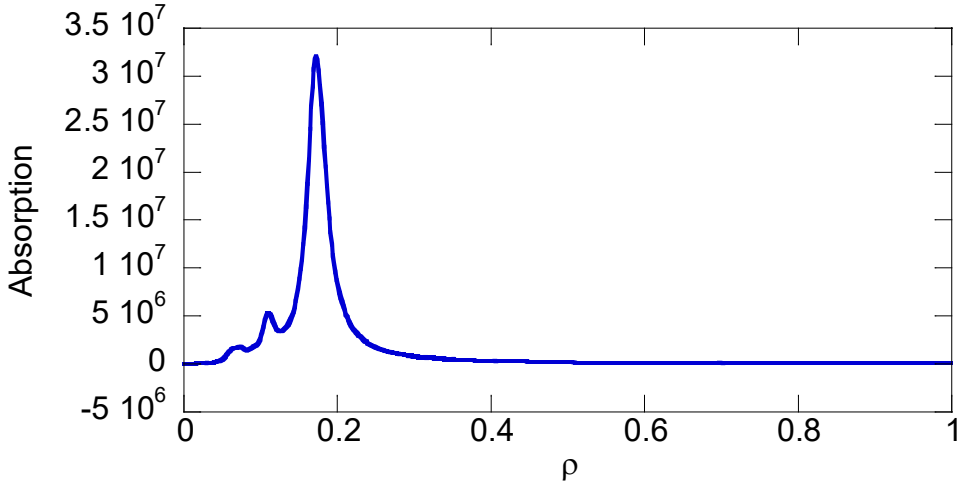

Fig. 2.14 The absorption of the block versus the density parameter ρ. It should be noted that the absolute value of absorption does not reflect actual physical quantity.

Then we compare the adjoint sensitivity with sensitivity calculated from central difference scheme

$$\frac{\partial f}{\partial \rho}(\rho_i) \cong \frac{f(\rho_{i+1}) - f(\rho_{i-1})}{\rho_{i+1} - \rho_{i-1}} \quad \text{2-142}$$

to verify the accuracy of the discrete adjoint sensitivity formula. Fig. 2.15 compares the two.

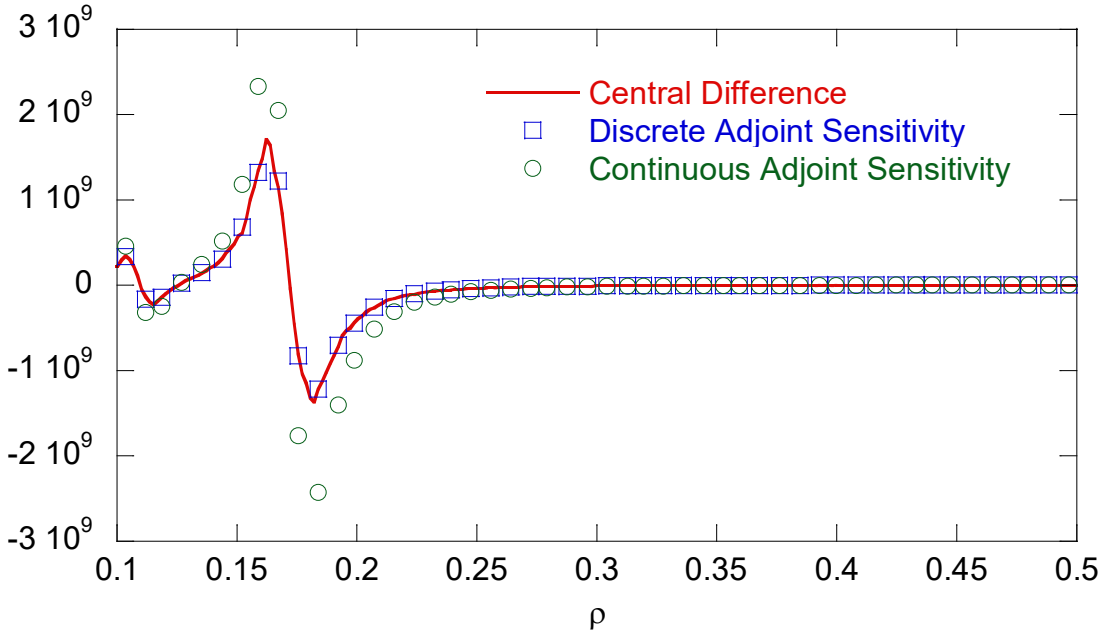

Fig. 2.15 Comparison of the central difference sensitivity, the discrete adjoint sensitivity and the continuous adjoint sensitivity in the range $\rho \in [0.1, 0.5]$. The discrete adjoint sensitivity is superior especially in the range of resonance.

The obvious agreement between the two confirms the validity of the discrete adjoint sensitivity formula. We also included the continuous adjoint sensitivity calculated from using rectangle rule in numerical integration of Equation 2-67. There is a huge disagreement between the continuous formula and the exact sensitivity at the resonance point where $\rho = 0.18$. This is due to the fact that FDTD is unable to capture accurate localized fields existing in resonance structure.

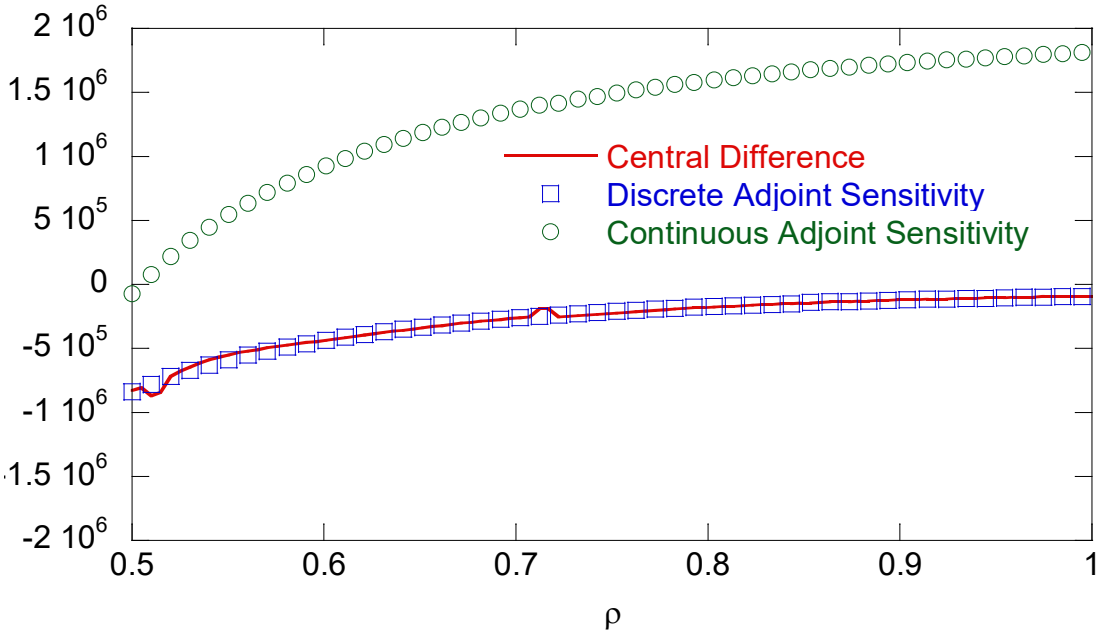

Fig. 2.16 Illustration of large error of continuous adjoint sensitivity in the region where $\rho \in [0.5, 1]$. This is also the region where the block has property close to gold and has strong localized field. The continuous sensitivity has the opposite sign of the true sensitivity.

Fig. 2.16 shows sensitivity in the range $\rho \in [0.5, 1]$. If only relative error is concerned, this range displays an even worse agreement where large portion of the continuous adjoint sensitivity has the wrong sign. In this range, the block has optical property close to gold and strong localized fields exist on the surface. This confirms an earlier statement that getting accurate sensitivity is particularly challenging in plasmonic structure. In the range $\rho \in [0,0.1]$, on the other hand, the two sensitivity are both pleasantly consistent with each other (Fig. 2.17). Because the block has property close to dielectrics in this range, there are no strong localized fields on the surface.

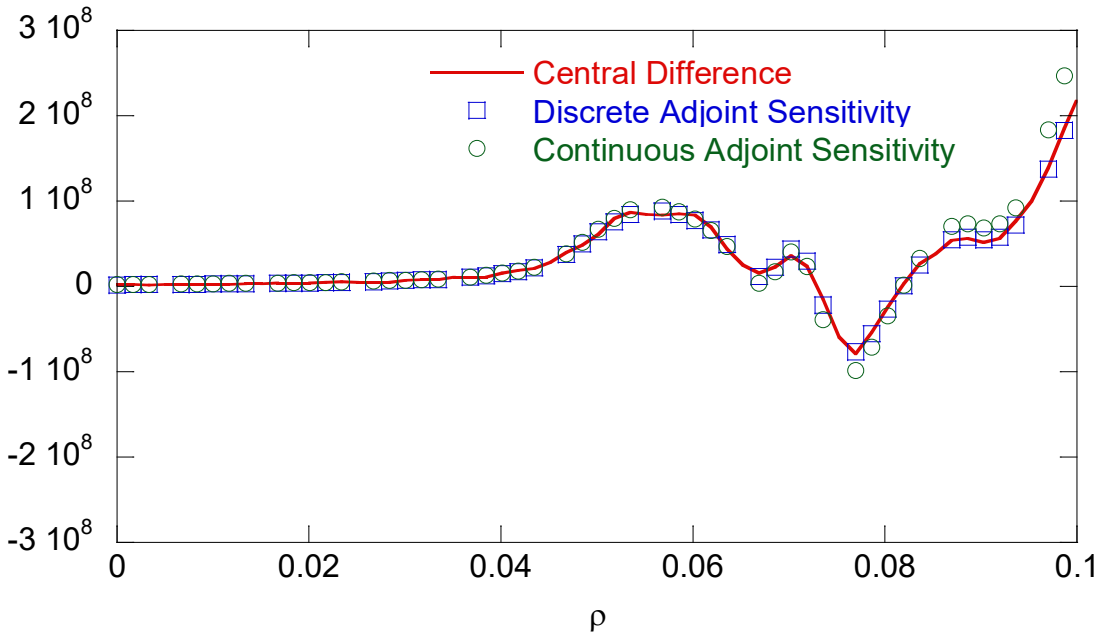

Fig. 2.17 Illustration of negligible error of continuous adjoint sensitivity in the region where $\rho \in [0, 0.1]$. This is also the region where the block has property close to air and no strong localized fields are produced.

In conclusion, this example demonstrates the robustness and accuracy of the discrete adjoint sensitivity and how the traditional continuous adjoint sensitivity fails in plasmonic structure because of highly localized fields.

2.7 Example: A Cylinder with Varying Radius

The next example considers an actual object and the function is the measure of electric field intensity. The measure of electric field intensity is usually the integral of the intensity over a specified region. Denote the field intensity by f, then

$$f = \int_V |\mathbf{E}| dV \tag{2-143}$$

Applying the rectangle rule to numerically integrate the above Equation gives

$$f = \sum_i |\mathbf{E}(\boldsymbol{r}_i)| \Delta V \tag{2-144}$$

The derivatives are then given by

$$\frac{\partial f}{\partial E_x(r_i)} = \Delta V \frac{E_x(r_i)}{|\mathbf{E}(\boldsymbol{r}_i)|} \tag{2-145}$$

$$\frac{\partial f}{\partial E_y(r_i)} = \Delta V \frac{E_y(r_i)}{|\mathbf{E}(\boldsymbol{r}_i)|} \tag{2-146}$$

$$\frac{\partial f}{\partial E_z(r_i)} = \Delta V \frac{E_z(r_i)}{|\mathbf{E}(\boldsymbol{r}_i)|} \tag{2-147}$$

Since only electric field intensity is concerned, the adjoint magnetic current is zero and the adjoint electric adjoint current $\nabla_e f$, defined in Equation 2-117, is calculated from these derivatives based on the transpose of interpolation given in Equation 2-124.

A cylinder of thickness 80 nm is placed in an open region where an incident wave of wavelength 800nm is traveling in the z^+ direction. The cylinder is made of gold and the same LD4 model [61] from previous section is adopted. The layout for the example is shown in Fig. 2.18.

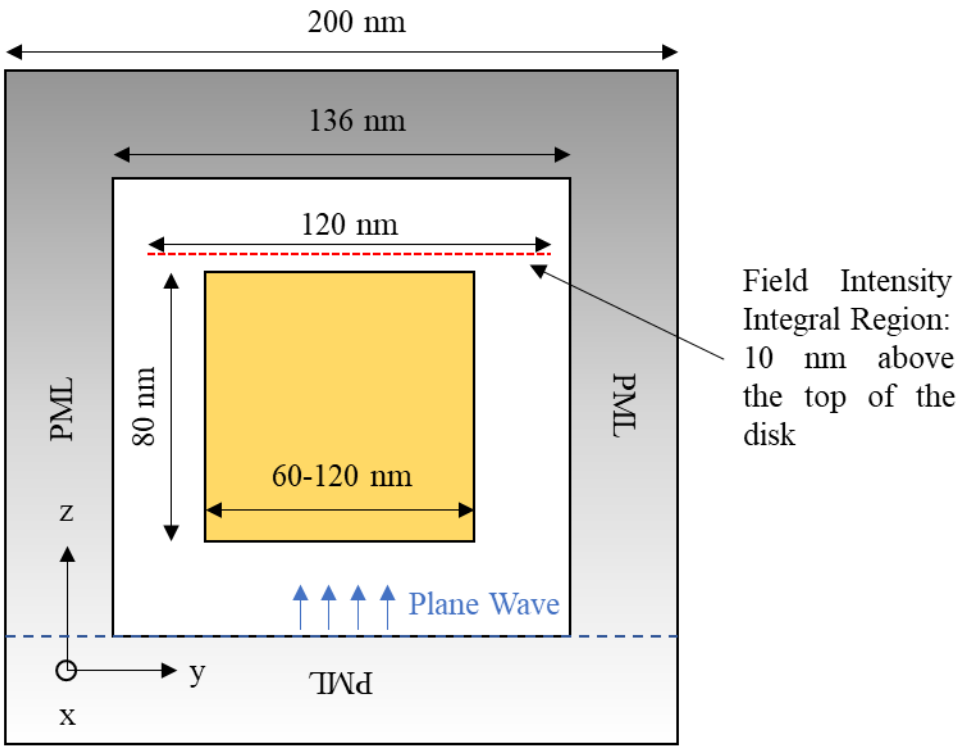

Fig. 2.18 Layout for the second example. A cylinder of radius ranging from 60nm to 120nm is seated in an open region where an incident wave of wavelength 800nm is traveling in the z^+ direction. Cylinder height is 80nm and field intensity in integrated on a 120nm × 120nm surface above the top of the cylinder.

Since we are using density parameters ρ's to assign material property for each component in the Yee cell, we utilized an approximation of Heaviside function to represent the material boundary

$$\rho(x,y,z) = -\frac{1}{\pi} arctan\left(a\left(\sqrt{x^2+y^2} - r_0\right)\right) + 0.5 \qquad 2\text{-}148$$

where r_0 is the radius of the cylinder and a defines the slope at the boundary. A higher value of a represents a shaper boundary representation. This is best illustrated in Fig. 2.19. $a = 2\ \text{nm}^{-1}$ is used in the actual simulation. After assigning density parameter based on Equation 2-148, linear material interpolation in Equation 2-71is applied. We use a 4 nm Yee cell length to run forward simulations to calculate the field intensity versus the radius of the cylinder.

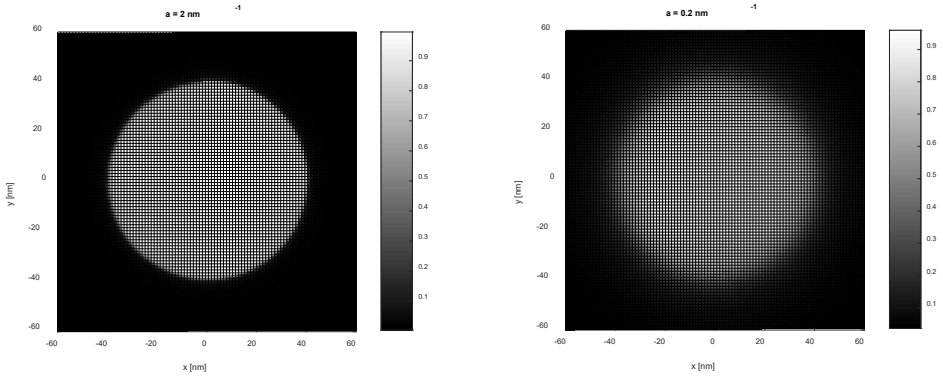

Fig. 2.19 Boundary representation of a cylinder. A higher a value produces sharper boundary of the geometry.

After obtaining adjoint sensitivity $\frac{\partial f}{\partial \rho(x_i,y_i,z_i)}$ with respect to density parameters at each discretized point, we apply chain rule to Equation 2-148 to get the gradient of f with respect to the radius

$$\frac{\partial f}{\partial r_0} = \sum_i \frac{\partial f}{\partial \rho(x_i,y_i,z_i)} \frac{\partial \rho(x_i,y_i,z_i)}{\partial r_0} \qquad 2\text{-}149$$

Result shows that f has a monotone trend and exhibits strong local fluctuations (Fig. 2.20). A similar case was previously reported in [62] where the author tried to calculate sensitivity of the field intensity of a metal slot. Although the author argued that this is due to the periodic smoothing of sharp corners, there is no sharp corner in our geometry which still has the ripple effect. One way to mitigate this non-smoothness is to apply the non-linear material interpolation scheme in Equation 2-72. The result is shown in Fig. 2.20 and compared with the linear interpolation scheme. Superior properties of this non-linear material interpolation scheme [39] was demonstrated for performing density-based topology optimization of metallic particles for electromagnetic design problems in the ultraviolet to low infrared wavelength regime. We shall use this in Chapter 4 for optimization.

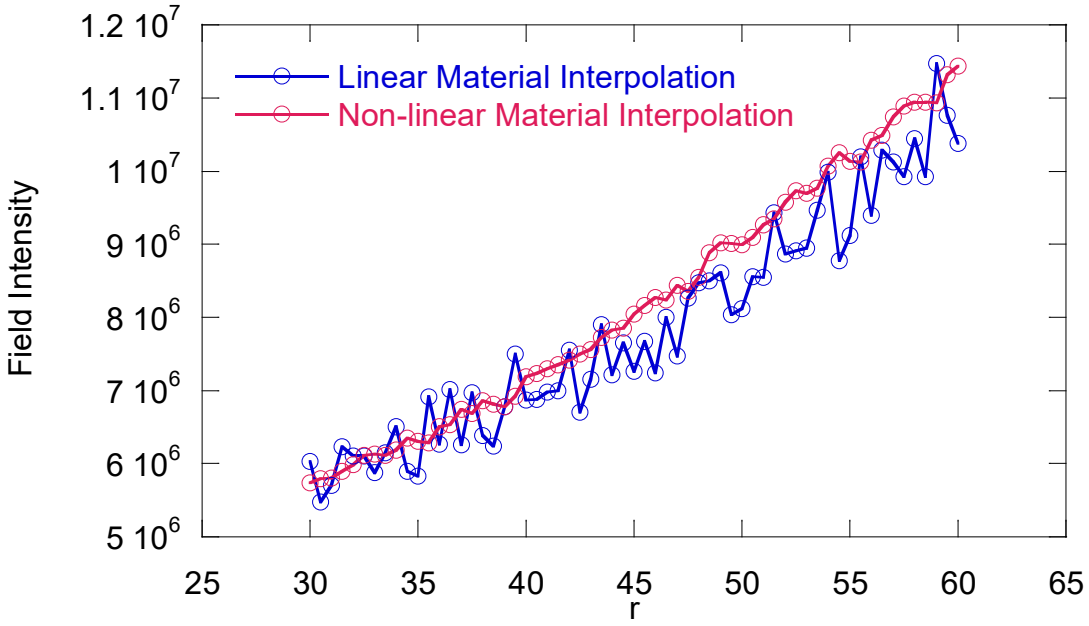

Fig. 2.20 Field intensity versus radius using two material interpolation schemes. It is evident that there is a general trend in increasing field intensity for increasing radius and considerable fluctuations when using linear interpolation.

Zooming in the field intensity profile, we can clearly see how the discrete adjoint sensitivity matches well with the exact sensitivity calculated from central difference scheme (Fig. 2.21) even though the original profile is quite "bumpy". This non-smoothness of field intensity in plasmonic structure destroys any hope of convergence for gradient based optimization. Therefore most of successful plasmonic structure optimization is done using FEM or surface integral formulations (SIE) [63][32][64] where the mesh near material boundary can be made extremely fine to capture accurate near fields.

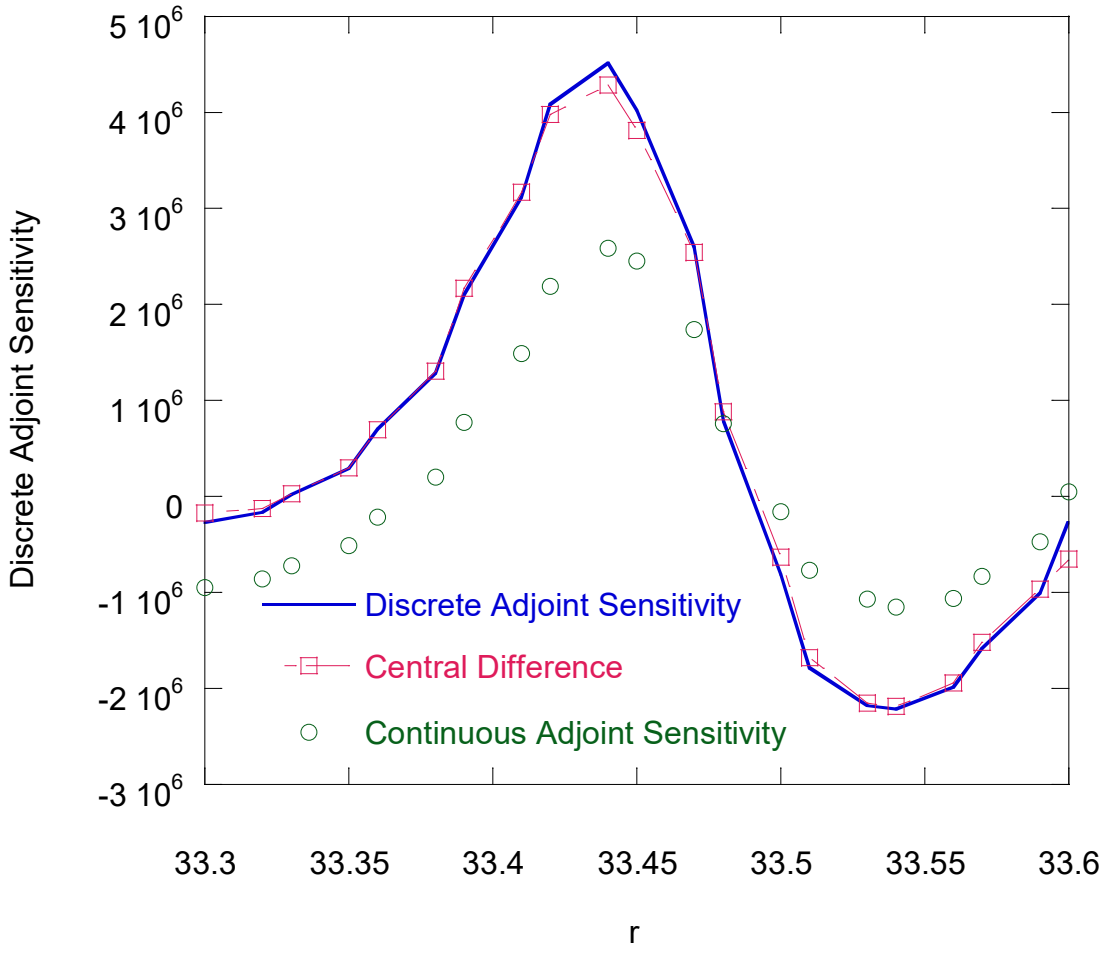

Fig. 2.21 Adjoint sensitivity in the range $r \in [33.4, 33.6]$ using linear material interpolation scheme. The discrete adjoint sensitivity reflects the exact sensitivity.

2.8 Conclusion

In this chapter, we present the derivations of both continuous and discrete adjoint sensitivity for Maxwell's equations in an open region problem. It should be noted although our derivation is limited to open region problems where Sommerfeld radiation conditions are satisfied, any other lossless boundary conditions like Bloch periodic boundary condition, Perfect Magnetic Boundary condition and Perfect Magnetic Boundary condition, are also applicable for the adjoint sensitivity Equations specified in Equations 2-67 and 2-120. Although Equation 2-120 is only suited for diagonal permittivity and permeability, one can easily follow the same procedures to get the formula for general permittivity and permeability implemented by some numerical scheme [65].

We dispense with discussions of lossy boundary conditions as they are not common in wave propagation problems. Several difficulties of obtaining accurate adjoint sensitivity using FDTD method are pointed out in Section 2.3 which inspired us to derive the robust discrete adjoint sensitivity and to adopt the non-linear material interpolation. The discrete adjoint sensitivity solves the problem of the FDTD method being unable capture accurate localized fields near material boundary and the non-linear material interpolation scheme mitigates the un-physical field enhancement during the optimization process. We present the first example to demonstrate the accuracy of the discrete adjoint sensitivity formula and compare it with the continuous adjoint sensitivity formula. Result shows that in plasmonic structure the continuous adjoint sensitivity formula is completely off the rail while in dielectric structure it behaves reasonably well. The second example considers a cylinder geometry and how the field intensity changes relative to the radius. It is discovered that using the linear material interpolation scheme produces lots of fluctuations in the field intensity in a plasmonic cylinder antenna. These fluctuations destroy any hope of convergence for gradient based optimization. Turning to the non-linear material interpolation which greatly reduces the "bumpiness", we can perform topology optimization in Chapter 4. An ad-hoc implementation of the non-linear material interpolation for gold is given at the end of Section 2.5.

3. TOPOLOGY OPTIMIZATION METHODS

The two primary methods in topology optimization are level-set-based and density-based topology optimization. They offer different degrees of freedom – the level-set based topology optimization allows perturbation of boundary while the density-based topology optimization assumes an even bigger solution space – and share some similarity – level-set method is essentially the same as density-based method if density geometry mapping is applied [2]. Level-set method has gained in popularity due to their promise to operate on clearly defined boundaries throughout the optimization process [17]. As we will see, density method tends to act like level-set method in later iterations of optimization process especially in plasmonic structures.

Since one of the goals of the thesis is to present a sensitivity analysis framework for FDTD method which is naturally compatible with density-based optimization, we will only give a brief review on level-set based method. The ill-posedness of the optimization problem may cause the optimization to converge to a local minimum with poor performance. Several regularizations are discussed at the end of the chapter to mitigate the ill-posedness of the problem and the so called standard method [38] is eventually implemented in cases in Chapter 4.

3.1 Level-set-based Topology Optimization

In the level-set approach, geometry is parameterized by a smooth level-set function ϕ which defines the material domain Ω, the void domain $\overline{\Omega}^c$ and the material interface as:

$$\begin{cases} \phi(\boldsymbol{x}) > c \Leftrightarrow \boldsymbol{x} \in \Omega \\ \phi(\boldsymbol{x}) = c \Leftrightarrow \boldsymbol{x} \in \partial\Omega \\ \phi(\boldsymbol{x}) < c \Leftrightarrow \boldsymbol{x} \in \overline{\Omega}^c \end{cases} \qquad 3\text{-}1$$

where c is a constant (usually $c = 0$). There are many ways to parameterize a smooth function using finite number of variables so that a computer program can solve the optimization problem. The most popular way of parameterization uses a set of scaling basis functions $\phi_i(x)$ such that

$$\phi(\boldsymbol{x}) = \sum_i s_i \phi_i(\boldsymbol{x}) \qquad 3\text{-}2$$

where s_i the i[th] design parameter. On two-dimensional domains, possible choices of basis functions include bilinear interpolation basis functions [66] and radial basis functions [67]. They are illustrated in Fig. 3.1.

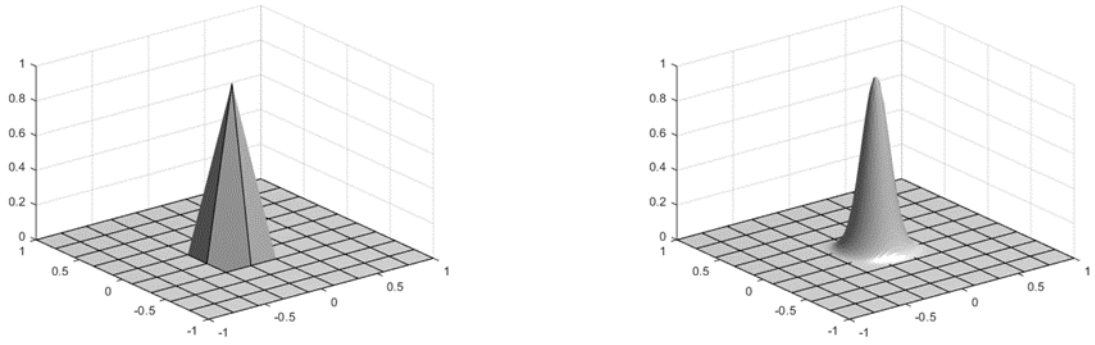

(a) A bilinear basis function (b) An RBF

Fig. 3.1 Two different types of basis functions in two dimensions.

Bilinear basis functions produce non-smooth boundary (sharp corners), which may be disadvantageous for certain applications. On the other hand, radial basis functions are inherently smooth, therefore offering a smooth boundary. Bilinear basis functions have a compact support (zero outside a compact region) and therefore most of the design parameters won't influence the boundary if they are not close to it. This offers a chance of efficient sensitivity computing since only those close to boundary need to be considered updating. On the other hand, radial basis functions extend to the entire domain so that every design variable can influence the boundary.

3.1.1 Geometry Mapping

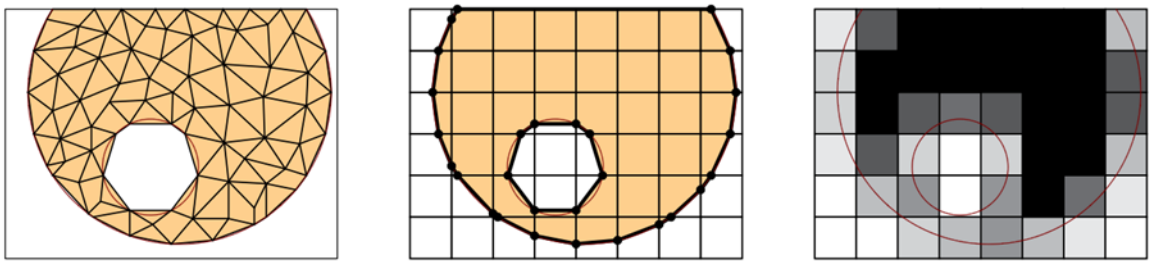

(a) Conforming Meshes

(b) Immersed Boundary Technique

(c) Density-based Mapping

Fig. 3.2 Different types of geometry mapping. Reprinted from [27] with the permission of Springer Nature.

As mentioned earlier in Chapter 1, the level-set method has the advantage of utilizing conforming boundary meshes (Fig. 3.2a) from FEM or BEM, leading to an accurate evaluation of near fields for plasmonic structures. This is particularly important if the continuous sensitivity analysis is applied. Using conforming meshes requires re-meshing in each iteration, resulting in noise to the objective function and an additional computational burden. The Immersed Boundary Techniques (IBTs) are proposed to avoid re-meshing while pertaining an accurate boundary representation. It creates a local discretization of the original structured grid and maintains strictly "black and white" boundaries (Fig. 3.2b). Care must be taken to implement IBTs to avoid bad discretization [68].

There are also other techniques that can map the level-set function to a numerical model without conforming meshes. One popular approach is to translate the LSF into a density distribution similar to density-based optimization methods [27]. This method assumes a density parameter $\rho \in [0,1]$ dependence on the level-set function

$$\rho(\phi) = H(\phi) \qquad 3\text{-}3$$

where $H(\cdot)$ is a Heaviside function satisfying

$$H(\phi) = \begin{cases} 0 \text{ for } \phi < 0 \\ 1 \text{ for } \phi \geq 0 \end{cases} \quad 3\text{-}4$$

In actual implementation, the exact non-differentiable Heaviside function is usually replaced with a smooth approximation of the Heaviside function, resulting in a smeared representation of the geometry and intermediate densities $0 < \rho < 1$. The density is either directly mapped to each gridded point or to each finite element using the average value of the density within the element. The density mapping is shown in Fig. 3.2c.

3.1.2 Shape Derivatives

When density geometry mapping is adopted, sensitivities with respect to design variables and those with respect to density parameters can be directly related through the parameterization of level-set function in Equation 3-2 and the relation between density and the level-set function in Equation 3-3. This effectively casts the level-set-based optimization into a density-based optimization problem which is discussed in Section 3.2.

For other types of geometry mapping, sensitivities with respect to design variables are built from the continuous adjoint sensitivity in Equation 2-67. In the level-set geometry parameterization, permittivity distribution is given by

$$\varepsilon = \varepsilon_1 + (\varepsilon_2 - \varepsilon_1)H(\phi) \quad 3\text{-}5$$

This is equivalent to assigning ε_2 to the material domain $\Omega = \{x \mid \phi(x) > 0\}$ and ε_1 to the void domain $\overline{\Omega}^c = \{x \mid \phi(x) < 0\}$. Suppose ϕ is perturbed by a small variation $\delta\phi$. Let $\delta\boldsymbol{x}$ be the resulting variation at point $\boldsymbol{x}$ (Fig. 3.3). Let $\partial\Omega' = \{x \mid \phi(x) + \delta\phi(x) = 0\}$ be the perturbed boundary. Taking the variation of the equation $\phi(\boldsymbol{x}) = 0$ [69]:

$$\delta\phi(\boldsymbol{x}) + \boldsymbol{\nabla}\phi(\mathbf{x}) \cdot \delta\boldsymbol{x} = 0 \quad 3\text{-}6$$

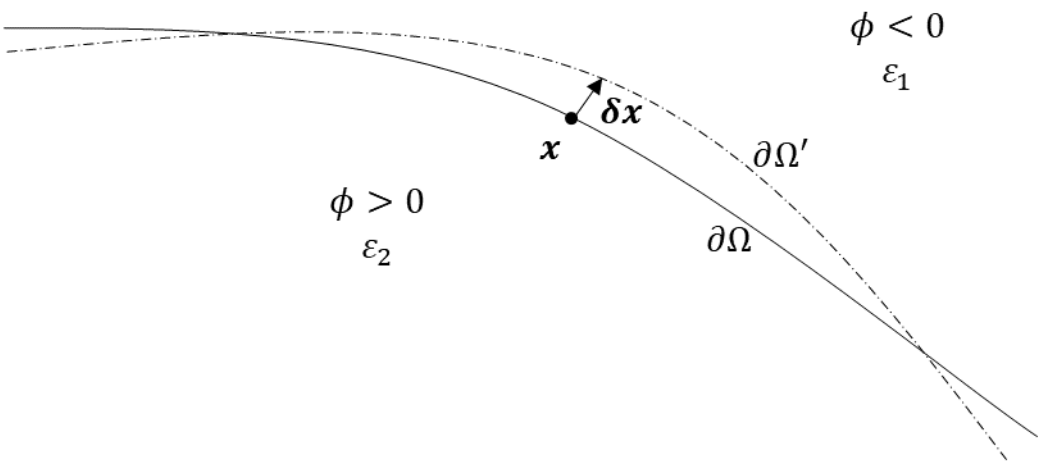

Fig. 3.3 Perturbation of the boundary by a small variation of the level-set function $\delta\phi$. This results in a normal movement of each point in the boundary.

Observe that $\delta\boldsymbol{x}$ and $\boldsymbol{\nabla}\phi(\boldsymbol{x})$ lies in the same direction, resulting in the normal movement of the boundary. Assuming expansion of the material domain is positive movement and contraction is negative, we have the magnitude of the movement δx given by

$$\delta x = \frac{\delta\phi}{\|\boldsymbol{\nabla}\phi(\mathbf{x})\|} \tag{3-7}$$

This implies that an increase in level-set function expands the material domain. Next we consider the variation of permittivity given in Equation 3-5

$$\delta\varepsilon = (\varepsilon_2 - \varepsilon_1)H'(\phi)\delta\phi \tag{3-8}$$

where $H'(\phi)$ is the first derivative of the Heaviside function. Substituting the above equation into the continuous sensitivity formula in Equation 2-67 yields

$$\delta F = \mathrm{Re}\left(\iiint_{\mathbb{R}^3} i\omega(\varepsilon_2 - \varepsilon_1)H'(\phi)\delta\phi\mathbf{E}\cdot\bar{\mathbf{E}}_a dV\right) \tag{3-9}$$

Notice that the first derivative of the Heaviside function $H'(\phi)$ is in fact the Dirac delta function, which is zero everywhere except at $\phi = 0$. The distribution theory [70] states that integral of the composition of Dirac delta function with a smooth function is equivalent to surface integral of the zero level-set function, i.e.

$$\iiint_{\mathbb{R}^3} gH'(\phi)dV = \iint_{\{\phi=0\}} \frac{g}{\|\nabla\phi\|} dS \tag{3-10}$$

where $\{\phi = 0\}$ is the zero level-set surface (the boundary) and g is any continuous function. Combining Equation 2-67 with Equation 3-10 gives

$$\delta F = \mathrm{Re}\left(\iint_{\{\phi=0\}} i\omega(\varepsilon_2 - \varepsilon_1) \frac{\delta\phi}{\|\nabla\phi\|} \mathbf{E} \cdot \bar{\mathbf{E}}_a dS \right) \tag{3-11}$$

and substituting the Equation 3-7 into the above equation gives

$$\delta F = \mathrm{Re}\left(\iint_{\{\phi=0\}} i\omega(\varepsilon_2 - \varepsilon_1) \mathbf{E} \cdot \bar{\mathbf{E}}_a \delta x dS \right) \tag{3-12}$$

It might seem we are done here since the above equation provides sensitivities with respect to boundary perturbation. However, $\mathbf{E} \cdot \bar{\mathbf{E}}_a$ is not continuous across the material interface, in which case the Equation 3-10 is not applicable. This prompts us to ask the question: how to convert $\mathbf{E} \cdot \bar{\mathbf{E}}_a$ to something that can make use of Equation 3-10? It is well-known that at the boundary the parallel electric fields $(\mathbf{E}^{\parallel}, \mathbf{E}_a^{\parallel})$ and the perpendicular electric displacements $(\mathbf{D}^{\perp}, \mathbf{D}_a^{\perp})$ are continuous. Recall that the adjoint system has permittivity $\varepsilon^{\dagger} = -\bar{\varepsilon}^T$. Assuming scalar permittivity, we can rewrite the discontinuous dot product in the integral as

$$\mathbf{E} \cdot \bar{\mathbf{E}}_a = \mathbf{E}^{\parallel} \cdot \bar{\mathbf{E}}_a^{\parallel} + \varepsilon^{-1}\mathbf{D}^{\perp} \cdot \overline{\varepsilon^{\dagger -1}\mathbf{D}_a^{\perp}} = \mathbf{E}^{\parallel} \cdot \bar{\mathbf{E}}_a^{\parallel} - \varepsilon^{-2}\mathbf{D}^{\perp} \cdot \bar{\mathbf{D}}_a^{\perp} \tag{3-13}$$

where $\mathbf{D}_a = \varepsilon^{\dagger}\mathbf{E}_a$. Now the first term $\mathbf{E}^{\parallel} \cdot \bar{\mathbf{E}}_a^{\parallel}$ at the right-hand side is continuous, while the second term $\varepsilon^{-2}\mathbf{D}^{\perp} \cdot \bar{\mathbf{D}}_a^{\perp}$ still has a jump due to the term ε^{-2}. We can safely invoke Equation 3-10 to evaluate the variation of objective function contributed from the first term:

$$\delta F^{\parallel} = \mathrm{Re}\left(\iint_{\{\phi=0\}} i\omega(\varepsilon_2 - \varepsilon_1)\mathbf{E}^{\parallel} \cdot \bar{\mathbf{E}}_a^{\parallel} \delta x dS \right) \tag{3-14}$$

For the second term, we substitute $\mathbf{E} \cdot \bar{\mathbf{E}}_a$ with $-\frac{1}{\varepsilon^2}\mathbf{D}^{\perp} \cdot \bar{\mathbf{D}}_a^{\perp}$ to the original sensitivity formula in Equation 2-67

$$\begin{aligned} \delta F^{\perp} &= \mathrm{Re}\left(\iiint_{\mathbb{R}^3} -i\omega\delta\varepsilon\varepsilon^{-2}\mathbf{D}^{\perp} \cdot \bar{\mathbf{D}}_a^{\perp} dV \right) \\ &= \mathrm{Re}\left(\iiint_{\mathbb{R}^3} i\omega\, \mathbf{D}^{\perp} \cdot \bar{\mathbf{D}}_a^{\perp} \delta(\varepsilon^{-1}) dV \right) \end{aligned} \tag{3-15}$$

where we make use of the chain rule in calculus of variation [44]. Similar to assigning permittivity distribution in Equation 3-5, the inverse of permittivity is given by

$$\varepsilon^{-1} = \varepsilon_1^{-1} + (\varepsilon_2^{-1} - \varepsilon_1^{-1})H(\phi) \tag{3-16}$$

Therefore, the variation of the inverse of permittivity is formulated as below

$$\delta(\varepsilon^{-1}) = (\varepsilon_2^{-1} - \varepsilon_1^{-1})H'(\phi)\delta\phi \tag{3-17}$$

Substituting the above Equation into Equation 3-15 and invoking the Equation 3-10 gives

$$\begin{aligned} \delta F^{\perp} &= \mathrm{Re}\left(\iiint_{\mathbb{R}^3} i\omega\, \mathbf{D}^{\perp} \cdot \bar{\mathbf{D}}_a^{\perp} \delta(\varepsilon^{-1}) dV \right) \\ &= \mathrm{Re}\left(\iiint_{\mathbb{R}^3} i\omega\, \mathbf{D}^{\perp} \cdot \bar{\mathbf{D}}_a^{\perp} (\varepsilon_2^{-1} - \varepsilon_1^{-1}) H'(\phi)\delta\phi dV \right) \\ &= \mathrm{Re}\left(\iint_{\{\phi=0\}} i\omega(\varepsilon_2^{-1} - \varepsilon_1^{-1})\mathbf{D}^{\perp} \cdot \bar{\mathbf{D}}_a^{\perp} \delta x dS \right) \end{aligned} \tag{3-18}$$

As a result, the total variation of objective function is given by

$$\begin{aligned}\delta F &= \delta F^{\parallel} + \delta F^{\perp} \\ &= \mathrm{Re}\left(\iint_{\{\phi=0\}} (i\omega(\varepsilon_2^{-1} - \varepsilon_1^{-1})\mathbf{D}^{\perp} \cdot \bar{\mathbf{D}}_a^{\perp} + i\omega(\varepsilon_2 - \varepsilon_1)\mathbf{E}^{\parallel} \cdot \bar{\mathbf{E}}_a^{\parallel})\delta x dS\right) \\ &= \iint_{\{\phi=0\}} \mathrm{Re}(i\omega(\varepsilon_2^{-1} - \varepsilon_1^{-1})\mathbf{D}^{\perp} \cdot \bar{\mathbf{D}}_a^{\perp} + i\omega(\varepsilon_2 - \varepsilon_1)\mathbf{E}^{\parallel} \cdot \bar{\mathbf{E}}_a^{\parallel})\delta x dS\end{aligned} \tag{3-19}$$

The left term $\mathrm{Re}(i\omega(\varepsilon_2^{-1} - \varepsilon_1^{-1})\mathbf{D}^{\perp} \cdot \bar{\mathbf{D}}_a^{\perp} + i\omega(\varepsilon_2 - \varepsilon_1)\mathbf{E}^{\parallel} \cdot \bar{\mathbf{E}}_a^{\parallel})$ inside the integral is called shape derivatives because it is the derivative of the objective function with respect to shape variation. Recalling that the boundary normal movement δx is dependent on $\delta\phi$ (Equation 3-7), we can derive the sensitivity with respect to design variables s_i

$$\begin{aligned}\frac{\partial F}{\partial s_i} &= \iint_{\{\phi=0\}} \mathrm{Re}(i\omega(\varepsilon_2^{-1} - \varepsilon_1^{-1})\mathbf{D}^{\perp} \cdot \bar{\mathbf{D}}_a^{\perp} + i\omega(\varepsilon_2 - \varepsilon_1)\mathbf{E}^{\parallel} \cdot \bar{\mathbf{E}}_a^{\parallel})\frac{\partial x}{\partial s_i} dS \\ &= \iint_{\{\phi=0\}} \mathrm{Re}(i\omega(\varepsilon_2^{-1} - \varepsilon_1^{-1})\mathbf{D}^{\perp} \cdot \bar{\mathbf{D}}_a^{\perp} + i\omega(\varepsilon_2 - \varepsilon_1)\mathbf{E}^{\parallel} \cdot \bar{\mathbf{E}}_a^{\parallel})\frac{\partial \phi}{\partial s_i}\frac{dS}{\|\nabla\phi(\mathbf{x})\|}\end{aligned} \tag{3-20}$$

As mentioned earlier in Section 2.5, we can directly solve the complex conjugate of the adjoint fields, resulting in another version of the above formula

$$\frac{\partial F}{\partial s_i} = \iint_{\{\phi=0\}} \mathrm{Re}(-i\omega(\varepsilon_2^{-1} - \varepsilon_1^{-1})\mathbf{D}^{\perp} \cdot \mathbf{D}_{ca}^{\perp} + i\omega(\varepsilon_2 - \varepsilon_1)\mathbf{E}^{\parallel} \cdot \mathbf{E}_{ca}^{\parallel})\frac{\partial \phi}{\partial s_i}\frac{dS}{\|\nabla\phi(\mathbf{x})\|} \tag{3-21}$$

where $\mathbf{D}_{ca} = \varepsilon\mathbf{D}_{ca}$ and $(\mathbf{E}_{ca}, \mathbf{H}_{ca})$ is governed by

$$\begin{pmatrix} -i\omega\varepsilon & \nabla\times \\ \nabla\times & i\omega\mu \end{pmatrix}\begin{pmatrix} \mathbf{E}_{ca} \\ \mathbf{H}_{ca} \end{pmatrix} = \begin{pmatrix} \overline{\frac{\delta F}{\delta \mathbf{E}}} \\ \overline{\frac{\delta F}{\delta \mathbf{H}}} \end{pmatrix} \tag{3-22}$$

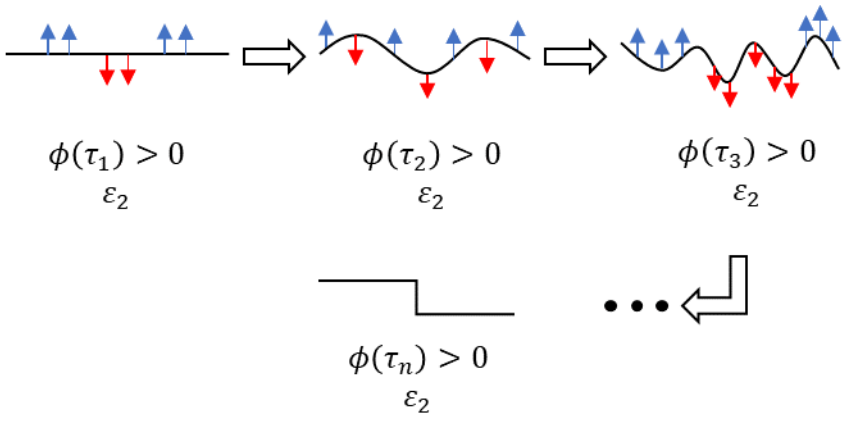

Fig. 3.4 Halmilton-Jacobi System. Blue arrows indicate positive velocity while red arrows indicate negative velocity. The boundary evolves over time and eventually settles at a stagnation point when the velocity field vanishes.

The integral in 3-20 is numerically evaluated along the boundary for each design variable in each iteration and a mathematical programming method can be applied to evolve the solution to a local optimum. Alternatively, the evolution of the level-set function can be formulated as a Hamilton-Jacobi (HJ) equation [30], in which we can assign a pseudo time τ and a normal velocity field $\boldsymbol{v}$ along the boundary so that the boundary moves continuously towards descent of the objective function (Fig. 3.4). Replacing the normal boundary movement δx with the normal velocity field in Equation 3-19 gives the rate of change in the objective function

$$\frac{\partial \mathrm{F}}{\partial \tau} = \iint_{\{\phi=0\}} \mathrm{Re}(i\omega(\varepsilon_2^{-1} - \varepsilon_1^{-1})\mathbf{D}^{\perp} \cdot \bar{\mathbf{D}}_a^{\perp} + i\omega(\varepsilon_2 - \varepsilon_1)\mathbf{E}^{\parallel} \cdot \bar{\mathbf{E}}_a^{\parallel})\boldsymbol{v} \cdot \boldsymbol{n} dS \qquad 3\text{-}23$$

To ensure a decreasing objective function over time, the velocity is usually assigned to be the negative of shape derivatives. For general procedures to solve the HJ equation, refer to [27].

3.1.3 Topological Derivatives

While shape derivatives only provide information to alter the boundary of the material domain, topological derivatives provide information on changes of response functions due to perforation of the material domain by an infinitesimal hole [53]. A topological derivative depends on the shape of the hole. Previously a topological derivative of a spherical hole is given by the Clausius-Mossoti factor in Equation 2-50. Let $F(\Omega)$ be the objective function implicitly depending on the material domain Ω, and $B(\boldsymbol{x}, r)$ be a small hole centered in $x \in \Omega$ with radius r (Fig. 3.5).

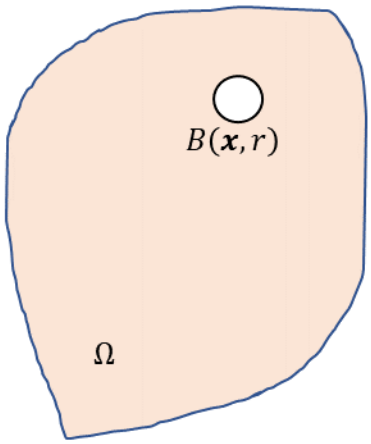

Fig. 3.5 A material domain Ω with one hole $B(x, r)$

The topological derivative is defined as

$$G(x) = \lim_{r \to 0} \frac{F\big(\Omega \backslash B(\boldsymbol{x}, r)\big) - F(\Omega)}{V\big(B(\boldsymbol{x}, r)\big)} \qquad 3\text{-}24$$

where $V\big(B(\boldsymbol{x}, r)\big)$ is the volume of the hole. Topological derivatives can be used to introduce new holes in the interior of the domain or outside the domain in a level-set optimization. Alternatively, it can be directly used in element-based update schemes where each element is a candidate of a new hole, in which case the scheme is called the bubble-method [71]. The bubble method was applied in the design of a waveguide to reduce the self-heating of the near-field transducer by 50%

in a heat-assisted magnetic recording system [14]. The author derives a topological derivative based on spherical holes and uses the FDTD method as the numerical model. Perhaps a cubic hole is better suited for the cartesian grid of the FDTD method.

Topological derivatives are derived for infinitesimal holes but in practice finite size holes are introduced in numerical implementations [17]. It is yet unclear whether the bubble method is better than the topological derivative aided level-set method in topology optimization in photonics.

3.2 Density-based Topology Optimization

Density-based topology optimization uses a material interpolation scheme to relate material property to density parameters ρ's. For example, we can assign the permittivity ε using linear interpolation

$$\varepsilon(x,\rho) = \varepsilon_1\rho(x) + \varepsilon_2\big(1-\rho(x)\big), \qquad \rho \in [0,1] \tag{3-25}$$

where ε_1 is the permittivity for the material domain and ε_2 is the permittivity for the void domain (usually $\varepsilon_2 = \varepsilon_0$). Under a specific numerical model of the Maxwell's equations, each node (line segment, pixel or voxel) is assigned a density parameter and the problem of finding the optimal design amounts to determining the value of ρ for each node. To utilize gradient-based optimization techniques, the density parameter is allowed to take intermediate values, resulting in gray transition regions. Such gray transition regions do not represent any realistic geometry and might lead to unphysical device design. Hence, regularizations must be applied to restrict the design space and to ensure manufacturability of the design.

In density-based optimization, meshes are often fixed during the optimization process (Eulerian approach) so that the design variables can be directly assigned as density parameters. In the Lagrangian approach, meshes are allowed to change during the process, requiring a mapping from design variables to density parameters similar to that of the level-set method. We will only discuss the Eulerian approach as it offers a much simpler implementation.

Density derivatives can be calculated from differentiation of the PDE followed by a numerical discretization. Differentiation of the PDE, resulting in the continuous adjoint sensitivity, offers the convenience to treat the numerical model as a black box. However, we have already shown that the continuous adjoint sensitivity is not accurate enough for design of plasmonic structures. Density derivatives calculated directly from differentiation of the numerical model are exact and exhibit a much better chance at convergence. This is one of the reasons why optimization of plasmonic structures is almost exclusively done with discrete adjoint sensitivity [64][39][72] or with level-set method [29][32] and conformal geometry mapping. Discrete matrix representation of the system is directly accessible with frequency domain solvers like FEM and enables easy implementation of discrete adjoint sensitivity analysis. However, FDTD does not have a discrete matrix representation in frequency domain. We recognize this complexity and present discrete adjoint sensitivity analysis in Chapter 2. This Section will address some regularization techniques to efficiently utilize the sensitivity information to ensure smooth convergence of the optimization and manufacturability of the design.

3.2.1 Density Derivatives

Density derivatives are the usual notion of derivatives of the objective function with respect to the density parameters. Contrary to topological derivatives which can predict the change in objective function when the geometry is altered with high contrast and spatially small holes, density derivatives work for low contrast and spatially big perturbation. Recall that under a specific numerical model, the Maxwell's equations and certain boundary conditions can be written as a matrix product

$$\mathbf{K}(\rho)x = b \tag{3-26}$$

where matrix $\mathbf{K}(\rho)$ is the discretized representation of the original PDE. Usually the dependence of $\mathbf{K}(\rho)$ to ρ is directly accessible from the numerical model, for instance, FEM or BEM. The adjoint sensitivity for matrix equation given in Equation 1-5 can then be applied to derive density derivatives. Alternatively, we can evaluate the continuous adjoint sensitivity given in Equation 2-67 within each finite element using numerical integration.

It is demonstrated in Chapter 2 that the continuous adjoint sensitivity does not work well with FDTD method. Therefore, we will use the discrete adjoint sensitivity in Equation 2-120 exclusively in later chapters.

In our approach, a rectangular design domain is constructed with a regular grid (cartesian lattice). Each point in the grid is assigned a density parameter ρ and linear interpolation is used to map the grid density parameter into the Yee lattice density parameter $p_w^{i,j,k}$. A 2D example of the interpolation is illustrated in Fig. 3.6.

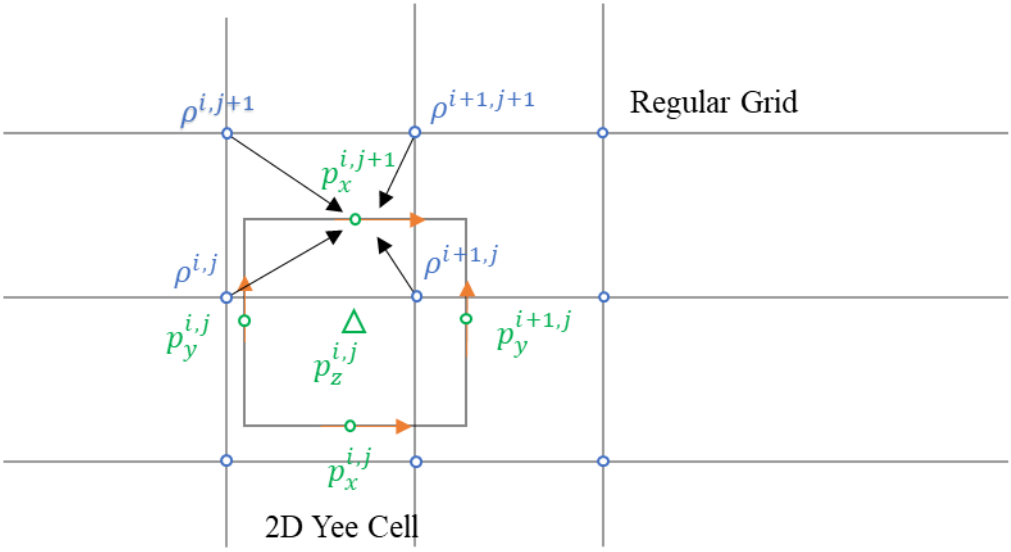

Fig. 3.6 Linearly interpolated density parameters in a 2D Yee lattice. Each Yee lattice density parameter (in green) is interpolated from the grid density parameter (in blue). The Yee cell size does not have to be equal to the grid size.

The interpolation effectively decouples the geometry from the Yee lattice such that the design region can be arbitrarily sized and positioned. However, the grid size for the design domain cannot be arbitrarily small. It cannot be 2 times smaller than the grid size of the Yee lattice otherwise it leaves some grid points unused during the interpolation. Calculation of sensitivities with respect to Yee lattice density parameter is done first according to equations 2-126, 2-127 and then follows the transpose of interpolation given in Equation 2-124 to propagate sensitivities back to the regular grid of the design domain. Note that the transpose of interpolation is carried out 6 six times for each component of the Yee cell (3 times if only dielectrics are considered).

3.2.2 The Standard Method

The so called standard method [38](or three-field density representation [33]) is adopted as the regularization technique in our method. The standard method uses a density filter followed by a projection. As pointed out several times in [17], this method becomes more and more similar to the level-set methods.

Viewing discretized density parameters ρ's as a 3D image, we can reassign each density value ρ_i as a weighted sum of its neighbors

$$\hat{\rho}_i = \frac{\sum_{j \in N_i} w_{ij} \rho_j}{\sum_{j \in N_i} w_{ij}} \tag{3-27}$$

Possible choices for the filter function w_{ij} include a linearly decaying function:

$$w_{ij} = R - \left\| x_i - x_j \right\| \tag{3-28}$$

as suggested in [35] and a Gaussian distribution function

$$w_{ij} = e^{-0.5\left(\frac{\left\| x_i - x_j \right\|}{R/2}\right)^2} \tag{3-29}$$

as suggested in [73]. R denotes the filter radius which is used to truncate the filter. It was tested that no significant difference is encountered between the two weighting functions [36]. We use the Gaussian distribution in our code. It should be noted that the original design variables ρ have no physical meaning and are used only as intermediate mathematical variables.

Density filters can effectively remove small features during the optimization process but end up creating more gray transition regions. Therefore, a projection operator is used to project the filtered density to 0/1. Suggested in [74], the following projection operator is used in our code:

$$\bar{\hat{\rho}}_i = \frac{\tanh(\beta\eta) + \tanh\left(\beta(\hat{\rho}_i - \eta)\right)}{\tanh(\beta\eta) + \tanh\left(\beta(1-\eta)\right)} \tag{3-30}$$

where β is a parameter used to control the sharpness of the projection and $\eta \in [0,1]$ defines the projection level (Fig. 3.7). Eventually, the projected density parameters $\bar{\hat{\rho}}_i$ is linearly interpolated into the Yee lattice density parameters ρ_w^{ijk}.

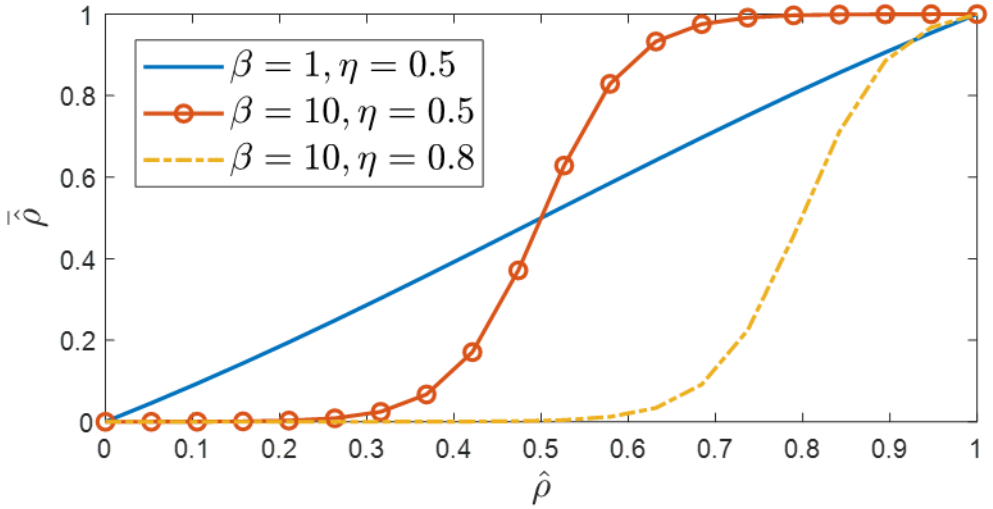

Fig. 3.7 Projection operators with different projection levels and sharpness.

Applying filtering (Equation 3-27) and projection (Equation 3-30) requires back propagation of sensitivities to the design variables, which is given below

$$\frac{\partial f}{\partial \hat{\rho}_i} = \frac{\partial f}{\partial \bar{\hat{\rho}}_i} \frac{\beta \operatorname{sech}^2\big(\beta(\hat{\rho}_i - \eta)\big)}{\tanh(\beta\eta) + \tanh\big(\beta(1-\eta)\big)} \tag{3-31}$$

$$\frac{\partial f}{\partial \rho_i} = \frac{\sum_{j \in N_i} w_{ij} \frac{\partial f}{\partial \hat{\rho}_j}}{\sum_{j \in N_i} w_{ij}} \tag{3-32}$$

The propagation of sensitivities along with the forward transformations of density parameters are summarized in Fig. 3.8. In fact, this is very similar to the back propagation in artificial neural networks because both are in essential exploitation of the chain rule.

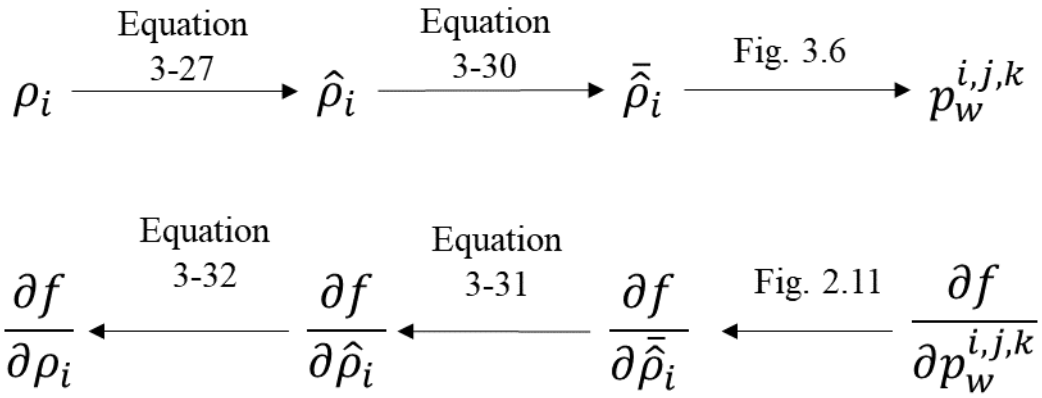

Fig. 3.8 Transformation of density parameters and back propagation of sensitivities.

The projection is usually used together with a continuation scheme for β, which gradually increases the projection sharpness during the optimization. This prevents the optimization from getting stuck in local minimum earlier in the process due to the density being projected to 0/1 immediately. We adopted the algorithm suggested in [38] to increase β only after the objective function has not changed much since the last increase in β.

3.3 Conclusion

Two primary methods used in topology optimization are described. The level-set method is better at providing a crisp and well-defined boundary representation while the density method searches answers in a much larger solution space. It is pointed that the use of FEM (BEM), level-set approach and conforming meshes together is often practiced in topology optimization in plasmonic structures. Due to the popularity of using FDTD method in simulation of plasmonic structures, we provide the other possibility of combining FDTD method, density approach and some regularization techniques to carry out the topology optimization in plasmonic structures. The discrete adjoint sensitivity with FDTD (Section 2.4) assures reliable access to gradients while the standard method (Section 3.2.2) improves convergence and manufacturability of the design.

4. CASE STUDIES

We present two examples, one with localized fields and one without localized fields, to demonstrate the possibility of using topology optimization to construct field patterns. In these two examples, we first calculate electric field patterns from a known structure and then deploy the inverse calculation algorithms to reconstruct the fields.

4.1 Bowtie Aperture

Bowtie apertures are known to produce highly localized fields and have potential applications in optical lithography [75], high density data storage [76], etc. The enhanced electric fields are confined within only a tiny region of the nanometer length scale near the surface of the nanostructures and decay significantly thereafter [72]. In this example, reconstruction of electric fields of a bowtie aperture is carried out using the proposed discrete sensitivity analysis in Section 2.4 and density-based topology optimization with the standard regularization techniques in Section 3.2.2.

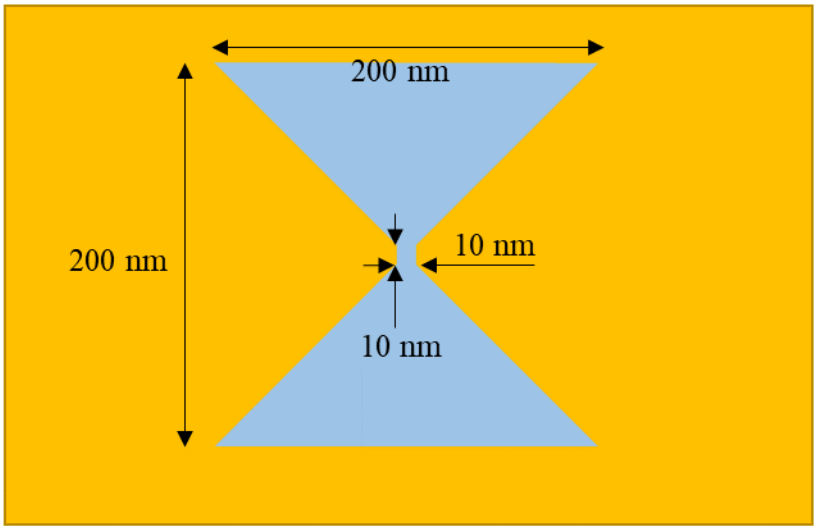

Fig. 4.1 Dimensions of the bowtie aperture for generating the objective electric field.

A bowtie aperture carved out of a gold layer of thickness 60 nm is placed in an open region where an incident wave of wavelength 800 nm is traveling in direction perpendicular to the layer. Fig. 4.1 shows the dimensions of the bowtie aperture. The objective electric field generated by the aperture is calculated using the FDTD method with a Yee cell length of 4 nm. Although in practice a smaller mesh size like 2 nm is needed to accurately capture the near field [54], we did not use a finer size because we are not interested in the actual physics of the system and we have limited amount of computational power. Layout for the simulation is shown below:

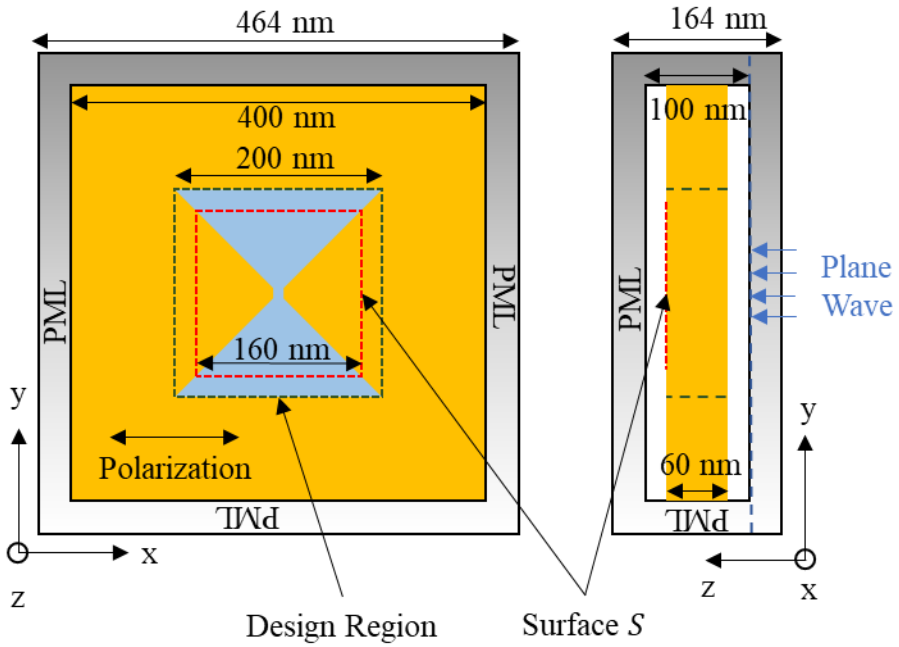

Fig. 4.2 Layout for the simulation (1st example). All rectangles are squres with their centers alighned. Polarization of the plane wave is in x direction.

We use the LD4 model given in Equation 2-141 as dispersion model of gold and its permittivity at 800 nm is evaluated as $\varepsilon_1 = \varepsilon_0(-22.3 - 2.03j)$. To measure the difference between the design electric field $\mathbf{E}$ and the objective electric field $\mathbf{E}_0$, the objective function is defined as

$$F(\mathbf{E}) = \int_S (\|\mathbf{E}\| - \|\mathbf{E}_0\|)^2 dS \qquad 4\text{-}1$$

where S is a rectangular surface at the exit plane of the bowtie aperture (Fig. 4.2). It is obvious that a smaller value of the objective function implies a better agreement with the objective field. The rectangle rule in Equation 2-144 is applied to numerically integrate the objective function on a rectangular grid of dimension $S_x \times S_y$. The reasons that the surface S is chosen at the exit plane are as follows: 1) the magnitude of the electric field is highest at the exit plane so that the objective function becomes highly singular and the robustness of the algorithm can be tested, and 2) it increases the possibility of the algorithm to recover the original geometry because different structures can produce the same field patterns at a large distance.

A Gaussian filter of radius R (Equation 3-29) and a projection operator of sharpness β and level $\eta = 0.5$ (Equation 3-30) are used to regularize the optimization. To prevent the optimization from getting stuck in local minimum earlier in the process due to the density being projected to 0/1 immediately, projection sharpness β are increased after the objective function has not changed much for n_{sc} iterations, mimicking the β-continuation scheme suggested in [74]. At the same time, we also reduce the filter radius to allow sharp corners to emerge, which is critical to generation of localized field. Our continuation scheme can be written in algorithmic form as follows.

Initialize filter radius = r
projection level = β
Run the following for k **times:**
    Objective function at the ith iteration = F^i
    Design parameters at the ith iteration = ρ^i
    while True:
        evolve the solution from ρ^i **to** ρ^{i+1} **using MMA**
        if $\left|F^i - F^{i-1}\right| < \alpha F^i$ **for consecutively** n_{sc} **times then:**
            $r = r/c_r$
            $\beta = \beta \times c_\beta$
            break out of the loop
return the solution

The design region is a 200 nm × 200 nm × 60 nm block centered in the gold layer (Fig. 4.2). The region is big enough so that the original bowtie geometry can be fitted in. The design region is discretized into a $N_x \times N_y \times N_z$ rectangular grid. Following the procedures in Section 3.2.1, each

grid point is assigned a density parameter and linear interpolation is used to map grid density parameters into Yee lattice density parameters. Non-linear material interpolation given in Equation 2-72 is adopted for interpolating permittivity from Yee lattice density parameters. A general rule for setting parameters is that the optimization converges to a local optimum within reasonable amount of time and that the manufacturability is ensured. Of course, this requires some trial and error. Table 4.1 shows parameters used in this example.

Table 4.1 Parameters used in optimization (1st example).

Parameter [unit]	Value
R [Yee cell length]	2.5
β	1
k	5
α	0.01
c_r	1.2
c_β	1.8
N_x, N_y, N_z	51, 51, 16[4]
S_x, S_y	41, 41

Obtaining the objective field is done by setting up the objective density distribution[5] ρ_0 (Fig. 4.3) in the design region and running the simulation once. Viewing the bowtie geometry as a planar polygon, density is to set to 1 if it is at a point inside the polygon. It should be noted the existence of solution for $F(\mathbf{E}) = 0$ is guaranteed in this case. The optimization algorithm starts with $\rho = 1$, representing pure gold layer, and runs for 5 rounds of optimization with different filter radius and projection sharpness, which constitutes a total of 105 iterations and 185 function evaluations. We enforce the density to be constant along z direction so that the optimization produces a planar structure.

[4] N_z discretized points are equivalent to $N_z - 1$ discretized intervals.
[5] The reason that it is called objective density is that it generates the objective electric field.

Fig. 4.3 shows the final design. Although symmetry isn't enforced during the optimization, the final design is symmetric with a smaller bowtie aperture and four holes in the corner. The smaller bowtie aperture generates the same magnitude of localized electric field in the center as the objective bowtie aperture, suggesting that much of the empty space is redundant in the objective design. Four holes emerge because the objective electric field has four smaller spikes in the four corners of S whose values are about 6 times higher than that of the incident field.

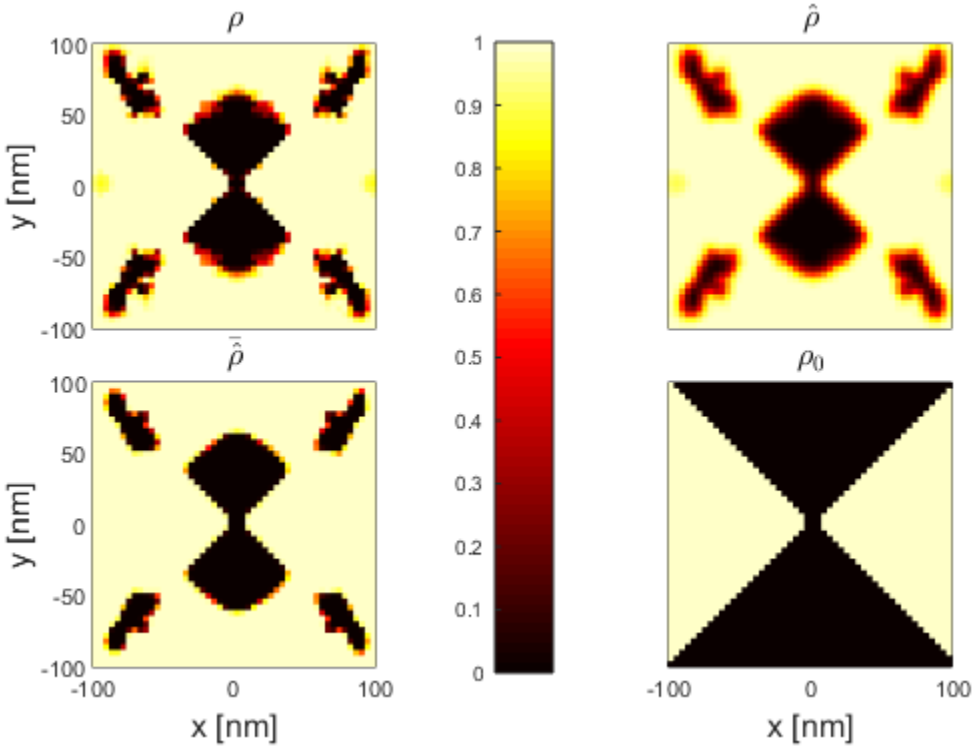

Fig. 4.3 Distributions of the design density ρ, the filtered density $\hat{\rho}$, the projected density $\bar{\hat{\rho}}$ in the final iteration and the objective density ρ_0 (1st example). Note that $\bar{\hat{\rho}}$ represents the actual design while $\rho, \hat{\rho}$ are intermediate variables.

Fig. 4.4 compares the final design electric field magnitude distribution with the objective electric field magnitude distribution on the surface S. The L^2 norm difference $\frac{\int_S (\|\mathbf{E}\| - \|\mathbf{E_0}\|)^2 dS}{\int_S \|\mathbf{E_0}\|^2 dS}$ bewteen them is about 3%, suggesting a successful recovery of the electric field on the surface S.

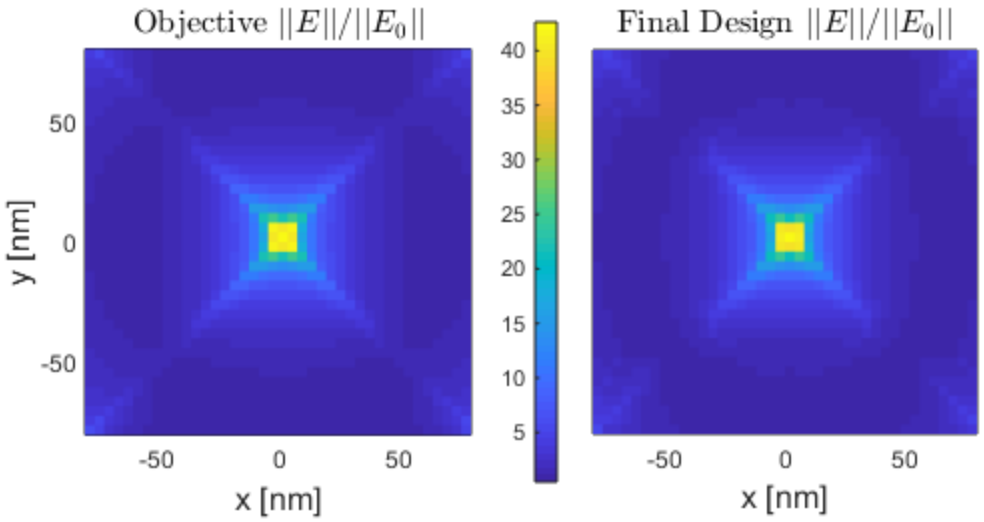

Fig. 4.4 Distributions of the final design electric field magnitude and the objective electric field magnitude on the surface S (1st example). The magnitudes are normalized by the incident magnitude. The maximum magnitude at center is 42.6 for both distributions.

A closer look at intermediate steps (Fig. 4.5) of the optimization reveals that only boundary perturbation is taking place in later iterations. The sharp decrease occurring between iteration 49 and iteration 50 is induced by the change of projection sharpness β from 5.8 to 10.5. Higher value of β brings in higher contrast of air and gold to the boundary, which contributes to the generation of highly localized fields. Furthermore, more density parameters are projected onto 0/1 when β increases, resulting in near vanishing gradients everywhere except at boundaries (Fig. 4.6). The near vanishing gradients are the reason why only boundary perturbation is taking place in later iterations.

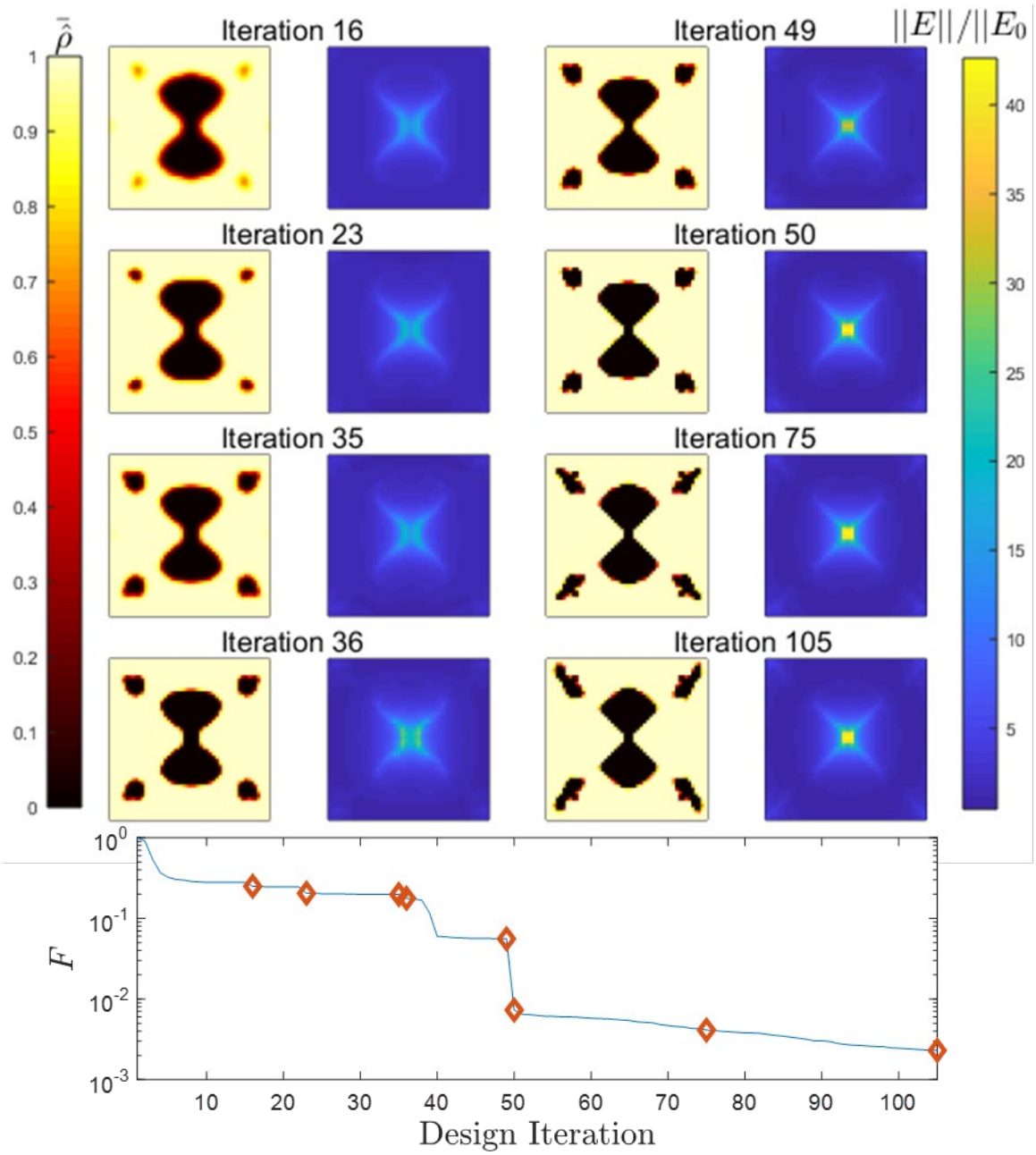

Fig. 4.5 Distributions of the projected density $\bar{\hat{\rho}}$ (left) and the design field magnitude (right) in some intermediate steps showing evolution of the design (1st example). Each iteration is marked with diamond in the objective function graph at the bottom. The objective function is normalized so that it is evaluated as 1 in the 1st iteration.

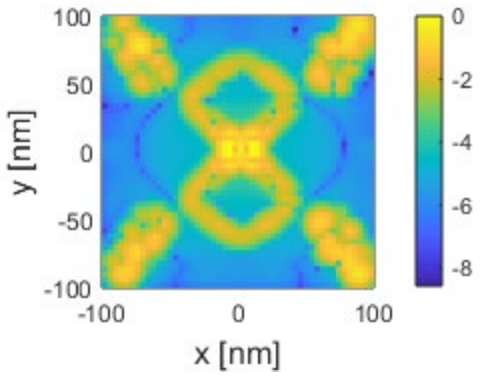

Fig. 4.6. Distribution of sensitivity (normalized) in logarithmic scale at the last iteartion (105).

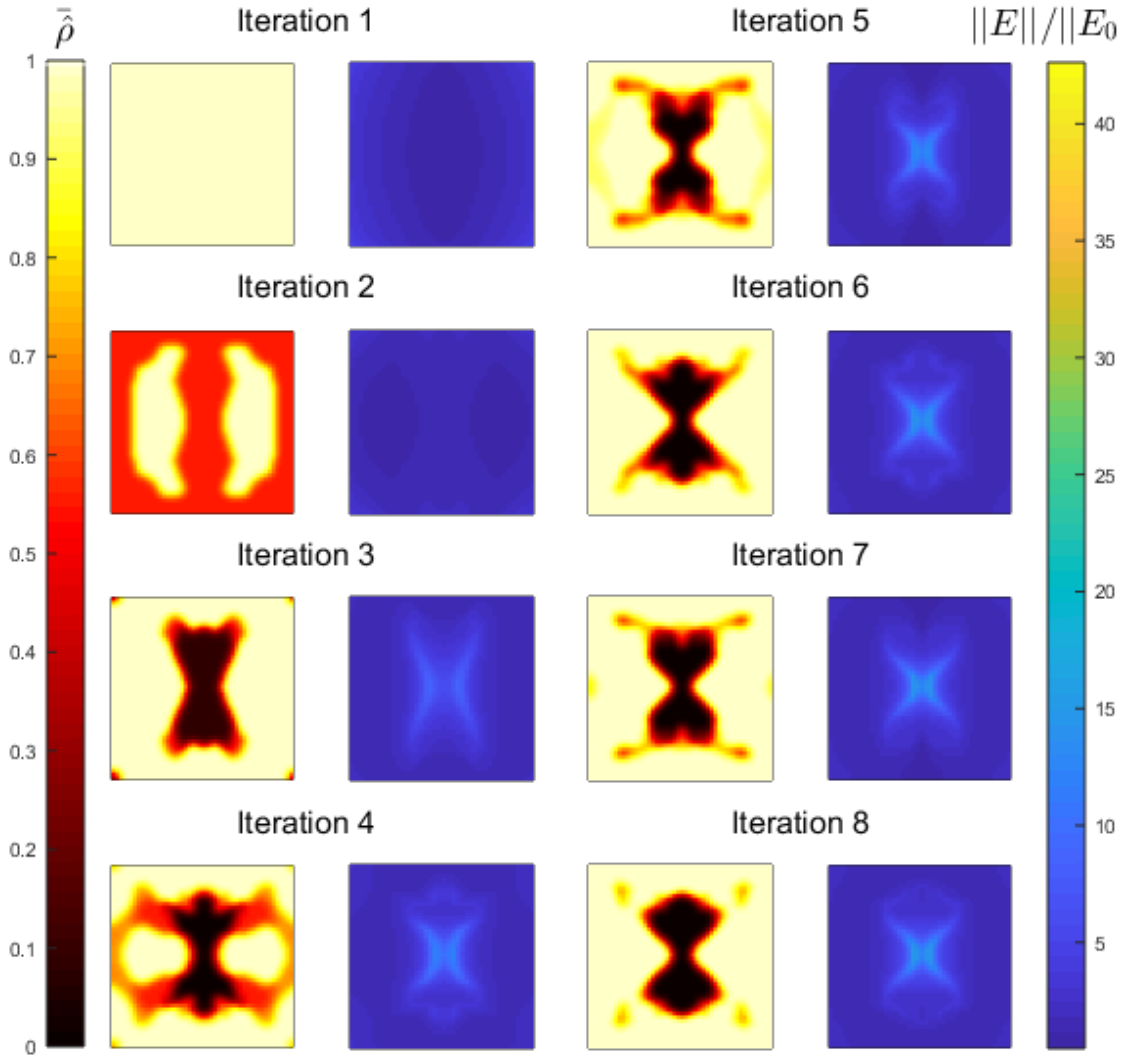

Fig. 4.7 Distributions of the projected density $\bar{\tilde{\rho}}$ (left) and the design field magnitude (right) in the first 8 iterations (1st example).

During the first 8 iterations (Fig. 4.7), the general shape of the final design already emerges. Early emergence of a clearly defined shape is also reported in [72][39] using density-based topology optimization. We believe that this phenomenon is related to objective function being singular. Slow convergence is observed in later iterations (Fig. 4.5). This suggests that to accelerate convergence in later iterations a level-set-based topology optimization can be initiated

4.2 Elongated Bowtie Antenna

The second example uses an elongated bowtie antenna (EBA). Fig. 4.8 shows the dimension of the objective geometry and Fig. 4.9 shows the simulation layout.

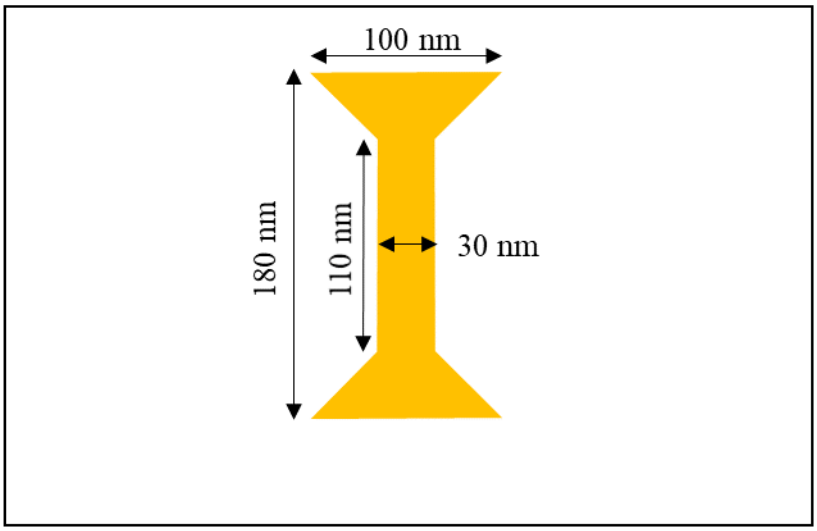

Fig. 4.8 Dimensions of the EBA for generating the objective electric field.

We follow the exact same procedures discussed in the previous section with the following differences: 1) different design region and surface S and 2) different parameters in the continuation scheme (Table 4.2).

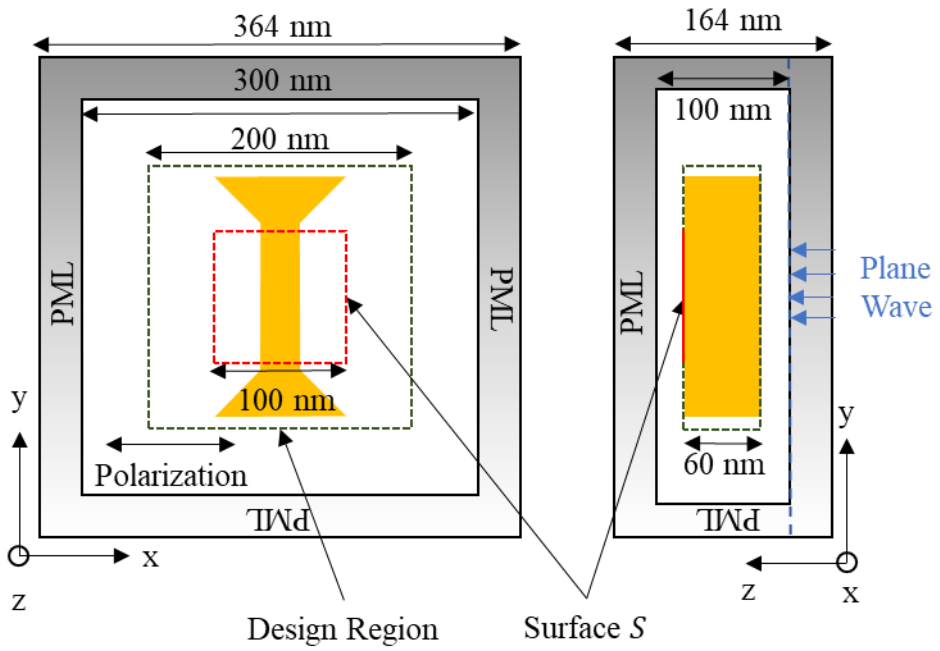

Fig. 4.9 Layout for the simulation (2nd example). All rectangles are squres with their centers alighned. Polarization of the plane wave is in x direction.

Table 4.2 Parameters used in optimization (2nd example).

Parameter [unit]	Value
R [Yee cell length]	2
β	1
k	6
α	0.01
c_r	1
c_β	1.8
n_{sc}	3
N_x, N_y, N_z	51, 51, 16
S_x, S_y	26, 26

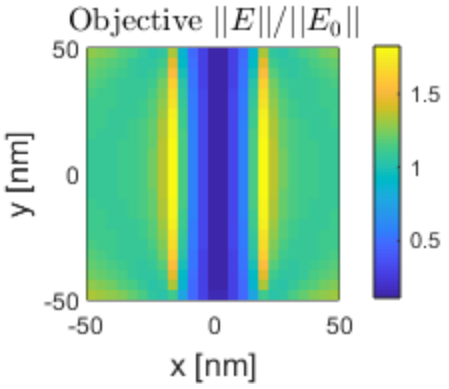

Fig. 4.10 Distribution of electric field magnitude of the objective geometry on surface S (2nd example).

Result of the simulation with the objective geometry shows that no highly localized electric field exists on surface S (Fig. 4.10). Therefore, small feature is not needed, and the filter radius is fixed ($c_r = 1$) throughout the optimization process. It will be later shown that lots of gray transition regions exist throughout the process. To ensure a 0/1 design, we increase the number of rounds k so that the optimization ends up with higher value of projection sharpness β. Unfortunately, this does not eliminate gray transition regions and one extra post-processing step is needed to produce a physically admissible structure. The optimization becomes quite time-consuming due to the addition of extra rounds. So, we reduce n_{sc} to induce a smaller number of iterations in each round. The optimization algorithm starts with $\rho = 0.5$, representing half-gold-half-air layer, and runs for 6 rounds and 166 iterations.

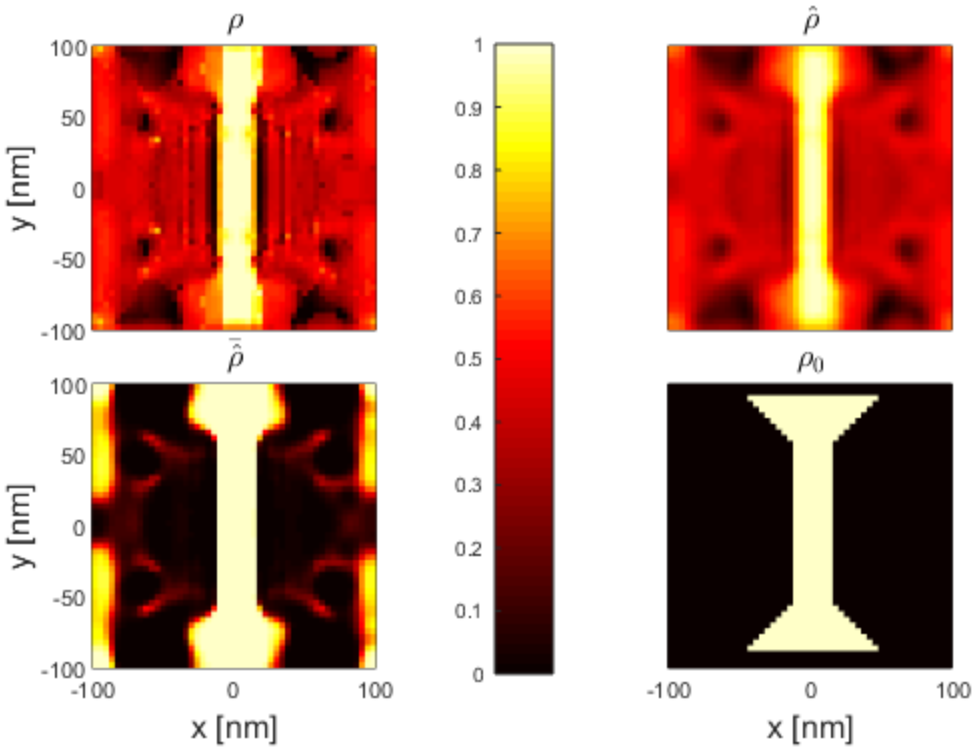

Fig. 4.11 Distributions of the design density ρ, the filtered density $\hat{\rho}$, the projected density $\bar{\hat{\rho}}$ in the last iteration and the objective density ρ_0 (2nd example). Note that $\bar{\hat{\rho}}$ represents the actual design while $\rho, \hat{\rho}$ are intermediate variables.

Fig. 4.11 shows the density distribution in the last iteration. It is observed that some gray transition regions still exist, different to what is observed in the 1st example. Also clearly defined boundaries do not show up in the first couple of iterations (Fig. 4.12). We believe that this is because the objective function of the 2nd example is less convex than that of the 1st example – there are far more structures that can generate a non-localized field (2nd example) than structures that can generate a highly localized field (1st example). Hence it is easier for the algorithm to converge to the global optimum (the objective geometry) in the 1st example than it is in the 2nd example. The final design has a bridge in the center, which is similar to that of the objective geometry.

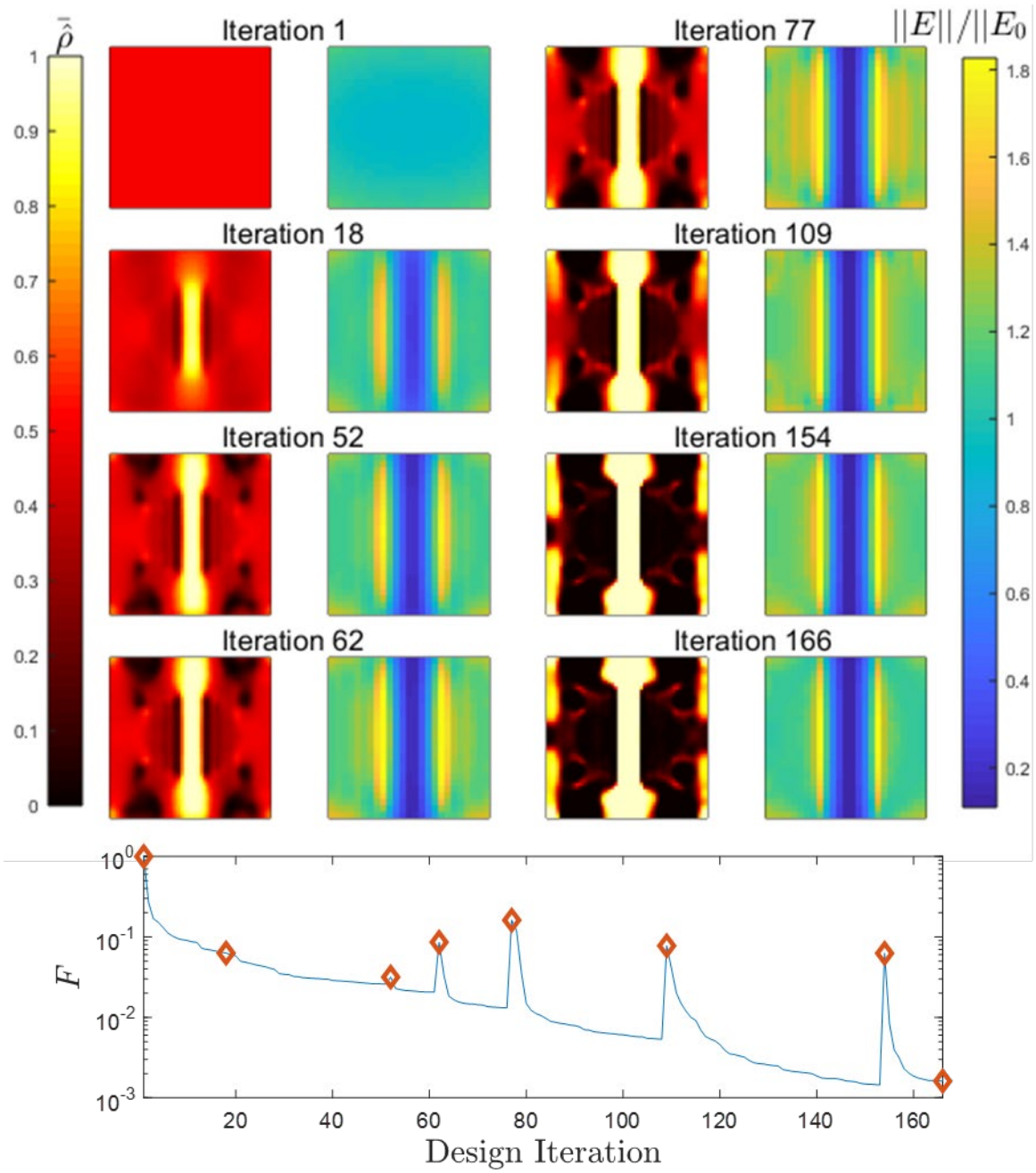

Fig. 4.12 Distributions of the projected density $\bar{\tilde{\rho}}$ (left) and the design field magnitude (right) in some intermediate steps showing evolution of the design (2nd example). Each iteration is marked with diamond in the objective function graph at the bottom. The objective function is normalized so that it is evaluated as 1 in the 1st iteration.

We apply the same filter and projection operator to the projected density from the last iteration and successfully eliminate all gray transition regions. However, this greatly increase the value of the objective function. So we run another round of optimization with the post-processed design

(Fig. 4.13) and end up with the objective function evaluated as 0.009 (normalized) while design from the last iteration has an objective function evaluated as 0.0016 (normalized), indicating a slightly downgraded performance.

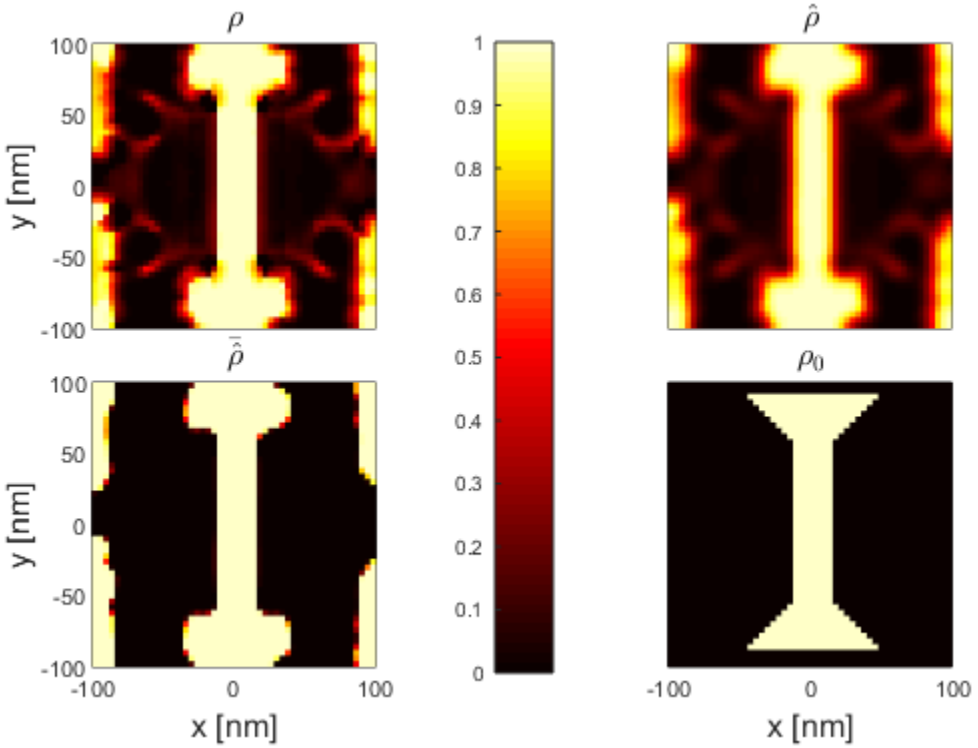

Fig. 4.13 Final design after post-processing and one round of optimization.

4.3 Conclusion

Two cases are presented to carefully examine the robustness and validity of the density-based topology optimization using the discrete adjoint sensitivity analaysis in the FDTD method. It is shown that proper regularizations are important in ensuring smooth convergence and manufacturability of the optimization. The filter-and-projection scheme is proven to work in the two cases, but many real world applications require a more complicated regularization scheme. Hence, successful application of topology optimization usually boils down to searching of proper regularizations.

5. CONSTRUCTING UNIFORM TEMPERTURE PROFILE IN HEAT-ASSISTED MAGNETIC RECORDING

In this Chapter, we inversely generate a uniform temperature profile in one-bit volume of the recording medium of heat-assisted magnetic recording (HARM). Although multiple simplications are made due to the constraint on computational power at hand, the application of topology optimization in solving practical plasmonic design problems is successfully carried out.

5.1 Heat-assisted Magnetic Recording

Recent years have seen HAMR become one of the most promissing technologies to push recording area density much higher than 1 Tb/in^2. As the storage density continues to increase, one of the problems is that the magnetic medium must be made of materials with a very high coercivity, requiring a magnetic field beyond what can be supplied by the hard disk head [77]. HAMR solves this problem by heating magnetic grains over the Curie temperature so that recording of data on those grains by switching the magnetic state can be achievable under small magnetic field. Fig. 5.1 shows this process.

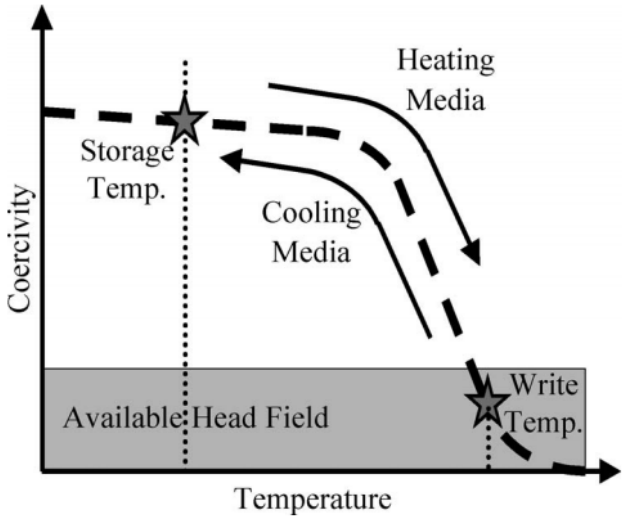

Fig. 5.1 A schematic diagram of the HAMR write process. Taken from [78]. Copyright © 2008, IEEE.

In a HAMR system, the recording medium is heated above its Curie temperature by a thermal spot that is less than 60 nm in the crosstrack direction [79]. Lots of efforts have been made [77][80][14][81] to design nano-plasmonic antennas/apertures, also called near-field transducers (NFTs), to deliver energy to such a small volume. Typical examples [81] of NFT designs include C-apertures, bowtie apertures, Lollipop antennas, etc. Gold is the preferred choice of material for NFTs for its chemical stability, good plasmonic behavior and high thermal conductivity [82]. Chemically ordered FePt has emerged as one of the leading candidates of medium materials mainly because significant progress has been made in fabricating high anisotropy granular FePt media at elevated processing temperature by commercially available sputtering tools [79]. Therefore, gold and FePt are used as the materials of NFT and recording medium respectively in this Chapter. In a typical HAMR system, light is coupled to the medium layer through an NFT (Fig. 5.2). The NFT is either embedded in a glass substrate or a gold layer. An interlayer made of MgO and a heatsink made of Cu are stacked below the medium layer.

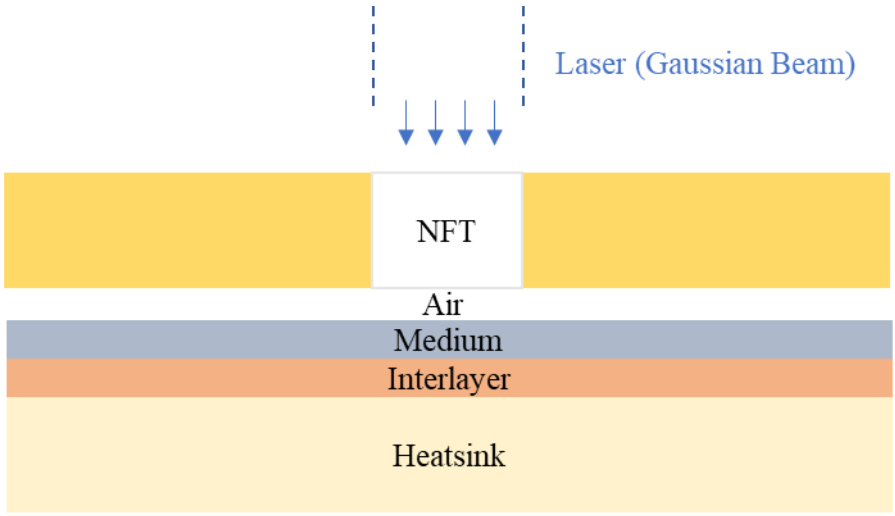

Fig. 5.2 Schematic of a NFT and a HAMR recording medium.

5.2 Problem Definition

Industry has recently shown interests in creating an uniform temperature profile inside one-bit volume in the recording medium. With tools from topology optimization, we attempt to design an NFT that generates the said uniform temperature profile. However, due to the limitation of

computational power (a typical server with 20 cores), we are unable to carry out a full-scale optimization. Hence we make the following simplications:

1. The interlayer and the heatsink are not considered.
2. Plane wave is assumed as the light source instead of a real Gaussian beam.
3. Thin-layer approximation is applied in modeling the heat conduction in the recording medium using an effective 2-dimensional absorption profile.
4. Heat generation in the NFT layer is ignored.

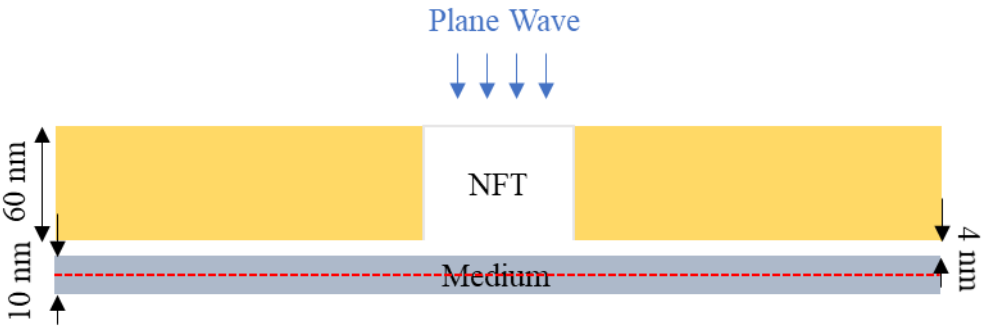

Fig. 5.3 Simplified HAMR system for optimization. Optical absorption at the midplane of the medium is taken as the effective absorption.

These simplications reduce the time for one EM simulation to ~20 minitues using a mesh size of 2 nm. The optimization problem is tackled in two stages: 1) searching for optical absorption profile to generate such uniform temperature profile and 2) constructing electric field magnitudes to generate the optical absorption profile. The LD4 model given in Equation 2-141 is used as the dispersion model of gold while the optical property of FePt is obtained from [83]. Table 5.1 lists optical properties of materials in our model along with thermal properties obtained from [84].

Table 5.1 Thickness, optical properties and thermal properties of the recording medium and the NFT.

Material	**Thickness [nm]**	**Refractive Index at 800 nm**	**Vertical thermal conductivity (W/mK)**	**Lateral thermal conductivity (W/mK)**	**Density × Specific Heat ($\rho \times c_p$) (J/m^3-K)**
Storage medium	10	n=3.2, k=2.6	7	1.5	3.2e6
NFT – Au	60	n=0.21, k=4.73	314	314	2.5e6
NFT – Air	60	n=1, k=0	0.02	0.02	0.001225

Heating is required to increase the temperature of one-bit volume ($60 \times 30 \times 10$ nm^3) to the Curie point $T_c = 750$ K of FePt [78] within 1 ns. Assuming an ambient temperature of 300 K, a temperature rise of 450 K is needed. While 450 K is the targeted temperature rise in our design, flexibility in the laser power allows easy scaling of temperature rise. For simplication, the NFT head is assumed to be still so that time independent heating is supplied in the recording medium.

5.3 Inverse Design

5.3.1 Thermal design

Careful study on energy transfer in HAMR system is conducted in [85] and a summary of the relavant energy transfer mechanisms is illustrated in Fig. 5.4, suggesting that the major energy mechanism is heat conduction and optical absorption. Furthermore, thin-layer approximation is applied because of the small thickness of the film and large vertical thermal conductivity relative to the lateral one. Therefore, a 2-dimensional heat conduction equation is used to describe heat transfer within the semi-infinite recording medium

$$\rho c \frac{\partial T}{\partial t} = \frac{\partial}{\partial x}\left(k_x \frac{\partial T}{\partial x}\right) + \frac{\partial}{\partial y}\left(k_y \frac{\partial T}{\partial y}\right) + \dot{q} \qquad 5\text{-}1$$

where the effective optical absorption $\dot{q}$ is the in-plane absorption profile at midplane of the recording medium.

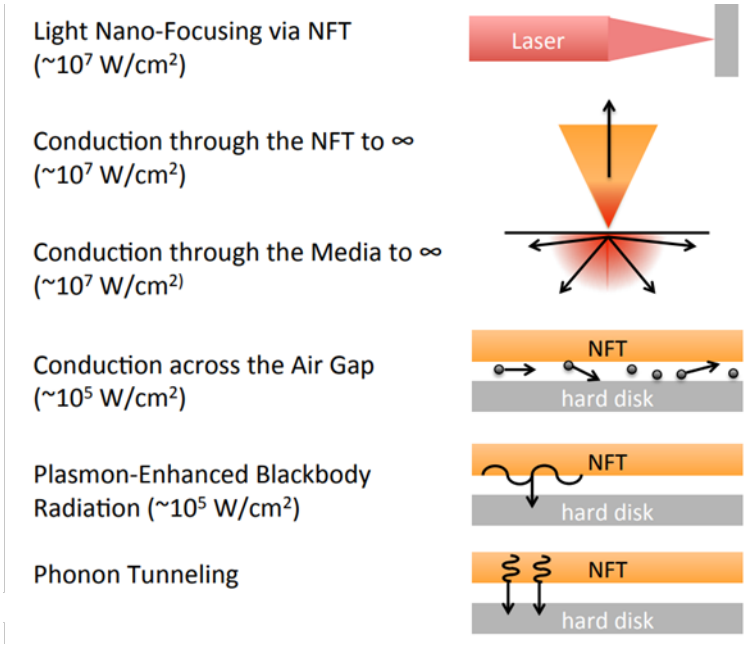

Fig. 5.4 A summary of the various energy transfer mechanisms in the HARM system. The most dominant energy transfers are via near-field light coupling from NFT to disk, heat conduction through the NFT and recording medium. Taken from [85].

Optical absorption inside the medium by a monochromatic light source is given by:

$$\dot{q} = \frac{1}{2}\omega \mathrm{Im}(\varepsilon_{\mathrm{FePt}})|\mathbf{E}|^2 \qquad 5\text{-}2$$

where ω is the frequency of the excitation light, ε_{FePt} is the permittivity of FePt and $|\mathbf{E}|^2$ is the light intensity. Gauging of the incident field magnitdue is done by borrowing the field magnitude from real lasers. For practical and economic reasons, the inexpensive diode lasers, with power ranging from 1 mW to 10 mW, are used as the optical source in commerical HAMR products. The laser propagates in space as a Gaussian beam focused on the NFT. The total transmitted power by a Gaussian beam is given by

$$P_0 = \frac{1}{2}\pi r_0^2 \frac{|\mathbf{E}_0|^2}{2\eta} \qquad 5\text{-}3$$

where r_0 is the beam waist radius, η is the wave impedence of the lossless medium in which the beam is traveling and $|\mathbf{E}_0|$ is the peak electric field amplitdue. The impedence of air is given by

$$\eta_{\text{Air}} = \sqrt{\frac{\mu_{\text{Air}}}{\varepsilon_{\text{Air}}}} = 377\ \Omega \tag{5-4}$$

Assuming a focused Gaussian beam of waist radius 300 nm and wavelength 800 nm is traveling in air and is incident on the NFT, the nominal absorption q_0 in the recording medium, calculated using Equation 5-2 with the incident field intensity, is $9.25 \times 10^{17}\ \frac{W}{m^3}$ per mW laser power. Note that the nominal absorption linearly scales with laser power.

For heat conduction problems in infinite 2-dimensional space, the temperature rise can be given by the convolution product of the heat generation and the Green's function

$$\Delta T(\boldsymbol{r}, t) = \frac{\alpha}{k}\int_0^t \int_{R^2} G(\boldsymbol{r} - \boldsymbol{r}', \tau) q(\boldsymbol{r}') d^2\boldsymbol{r}'\, d\tau \tag{5-5}$$

where $\boldsymbol{r} \in \mathbb{R}^2$ is the coordinate vector and $G(\boldsymbol{r}, \tau)$ is the Green's function given by

$$G(\boldsymbol{r}, \tau) = \frac{1}{4\pi\alpha t} e^{-\frac{|\boldsymbol{r}|^2}{4\alpha t}} \tag{5-6}$$

To approximate the convolution, we first numerically integrate Equation 5-5 in time using the rectangle rule

$$\Delta T(\boldsymbol{r}, t_M) \approx \sum_{i=0}^{M} \Delta t \int_{R^2} G(\boldsymbol{r} - \boldsymbol{r}', \tau_i) q(\boldsymbol{r}') d^2\boldsymbol{r}' \tag{5-7}$$

where $\tau_i = i\Delta t$. Notice that $G(\boldsymbol{r}, \tau_0 = 0)$ is ill-defined in the classical sense, so it should be treated rather as a limit

$$\int_{R^2} G(\boldsymbol{r}-\boldsymbol{r}',0)q(\boldsymbol{r}')d^2\boldsymbol{r}' = \lim_{\tau\to 0}\int_{R^2} G(\boldsymbol{r}-\boldsymbol{r}',\tau)q(\boldsymbol{r}')d^2\boldsymbol{r}' \tag{5-8}$$

Since the Green's function is a Gaussian function, we can invoke the approximation of identity theorem [49] to evaluate the above equation, which gives us

$$\lim_{\tau\to 0}\int_{R^2} G(\boldsymbol{r}-\boldsymbol{r}',\tau)q(\boldsymbol{r}')d^2\boldsymbol{r}' = q(\boldsymbol{r}) \tag{5-9}$$

Combining Equations 5-7, 5-8 and 5-9, we have

$$\Delta T(\boldsymbol{r},t_M) \approx \Delta t q(\boldsymbol{r}) + \sum_{i=1}^{M}\Delta t\int_{R^2} G(\boldsymbol{r}-\boldsymbol{r}',\tau_i)q(\boldsymbol{r}')d^2\boldsymbol{r}' \tag{5-10}$$

Further discretization in space gives

$$\Delta T(\boldsymbol{r}_{N,L},t_M) \approx \Delta t q(\boldsymbol{r}) + \Delta t\Delta x\Delta y\left(\sum_{i=1}^{M}\sum_{j,k\in\mathbb{Z}} G(\boldsymbol{r}_{N,L}-\boldsymbol{r}_{j,k},\tau_i)q(\boldsymbol{r}_{j,k})\right) \tag{5-11}$$

where $\boldsymbol{r}_{N,L} = (N\Delta x, L\Delta y)$ is the discretized coordinate vector. Noticing that the summation in Equation 5-11 is in fact the discretized convolution product, we can rewrite it in a more compact way[6]

$$\Delta T(\cdot,t_M) \approx \left(\sum_{i=1}^{M} G(\cdot,\tau_i)\Delta t\Delta x\Delta y + \Delta t\,\delta_d\right) * q = S * q \tag{5-12}$$

where $(\cdot,t_M)$ is used to emphasize that the first argument is a variable and the second argument is fixed. Note that δ_d is the discretized Dirac function [26]. We truncate each $G(\cdot,\tau_i)$ to a square area with side length $a = 6\sqrt{2\alpha t_M}$, equivalent to truncating the domain of a Gaussian function with

[6] $*$ is previously used to denote continuous convolution. Here it denotes the discretized convolution.

standard deviation σ to a square area with side length $a = 6\sigma$. Note that to get an accurate evaluation of temperature rise within an area of size $c \times d$, the optical absorption must be evaluated at least in an area of size $(a + c) \times (a + d)$. Therefore, for evaluating temperature at 1 ns the side length must be at least $a = 183$ nm. Now the problem of finding the optical absorption distribution that generates a uniform temperature profile inside one-bit volume in the recording medium amounts to the following optimization problem

$$\begin{aligned} &\min_{q} \; 0.5 \sum_{\boldsymbol{r}_{i,j} \in A} \left(\Delta T\left(\boldsymbol{r}_{i,j}, t_M\right) - 450\right)^2 \\ &\text{subject to:} \quad \Delta T(\cdot, t_M) = S * q \\ &\qquad\qquad\quad q_l \le q \le q_u \end{aligned} \tag{5-13}$$

where A is a rectangular area occupied by a single bit centered at the origin and q_l, q_u are the lower bound and the upper bound of the optical absorption imposed by limited laser power and limited field enhancement inside the recording medium. The lower bound of the absorption is obtained by simulating the physical structure without NFT, corresponding to absorption at points far away from the NFT. It is calculated to be $q_l = 0.005 q_0$. In our experience, the upper bound is of great importance in the optimization as it indicates the maximum field enhancement that can occur in the recording medium. We assign the upper bound to be $q_u = 5 q_0$, which corresponds to the maximum field enhancement in the recording medium produced from the objective bowtie aperture in Section 4.1.

A direct solution of the optimization problem in Equation 5-13 produces unreasonably sharp optical absorption profile with ~4 nm wide peaks, albeit generating perfectly uniform temperature profile (Fig. 5.5).

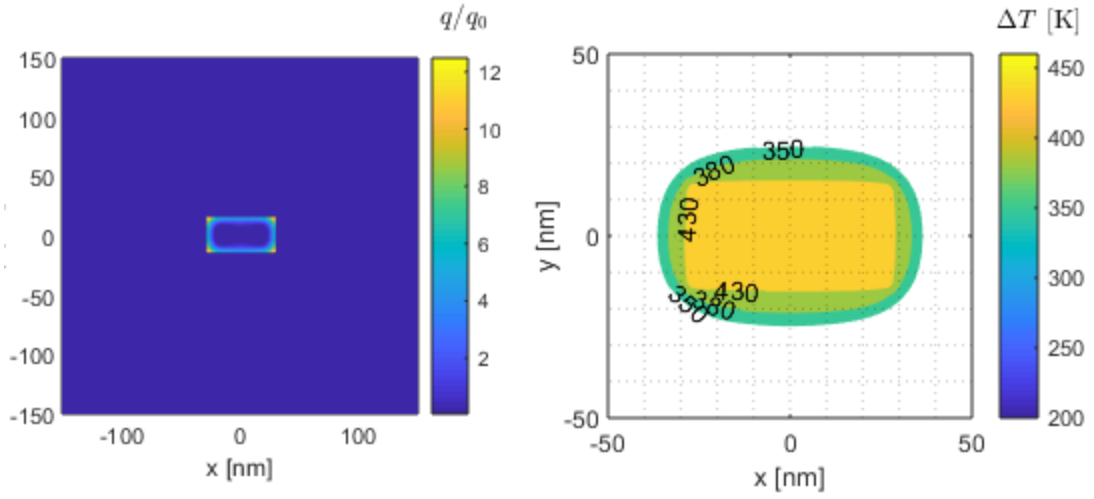

Fig. 5.5 The distribution of the optimized absorption (left) and contours of temperature rise distribution (right) produced from optimization without filtering. The absorption is normalized by the nominal absorption q_0.

These peaks are not physically admissible and cause the electromagnetic optimization to fail. Therefore, we impose a filter on the absorption distribution similar to the filter used in topology optimization in Equation 3-27 to increase widths of peaks. The optimization problem after applying filter becomes

$$\min_{q} \; 0.5 \sum_{\boldsymbol{r}_{i,j} \in A} \left(\Delta T(\boldsymbol{r}_{i,j}, t_M) - 450\right)^2 \qquad 5\text{-}14$$

$$\text{subject to:} \quad \Delta T(\cdot, t_M) = S * q_f$$

$$q_f = q * w$$

$$q_l \le q_f \le q_u$$

where w is a gaussian filter given in Equation 3-29 and q_f is the filtered absorption. We run the L-BFGS-B algorithm [43] to solve the optimization problem using the following parameters: 1) laser power is $P_0 = 1$ mW, 2) the temperature and absorption is evaluated on a rectangular grid spanning 300×300 nm^2 with 2 nm cell length, 3) gaussian filter radius is 40 nm. Evaluation of absorption on a 300×300 nm^2 area is reliable for evaluation of temperature on a 127×127 nm^2 area according to previous discussion. Fig. 5.6 displays the results. The 430 K contour line occupies an area of 60×30 nm^2 equivalent to that of one-bit volume in the recording volume.

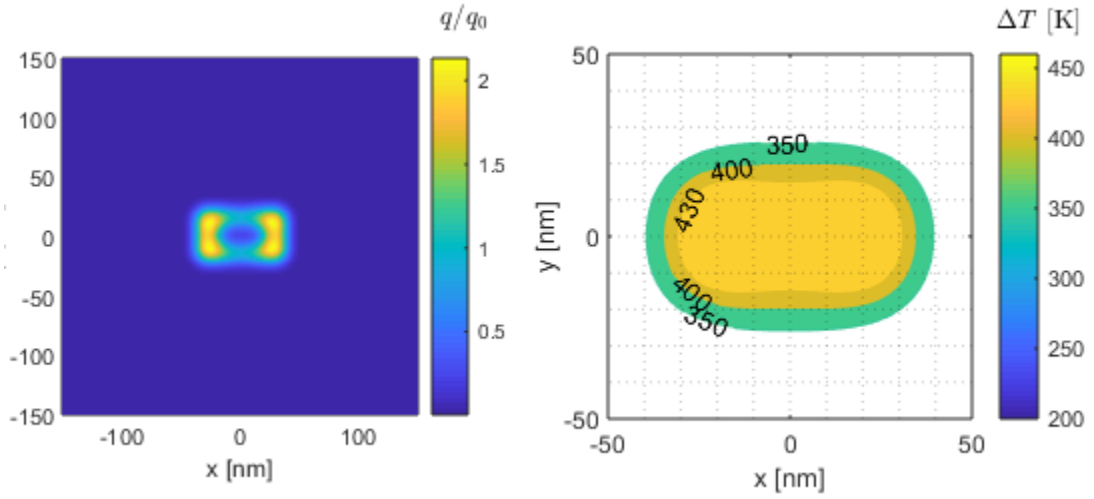

Fig. 5.6 The distribution of the optimized absorption (left) and contours of temperature rise distribution (right) produced from optimization with filtering. The absorption is normalized by the nominal absorption q_0.

One important figure of merit in HAMR is the thermal gradient along cross-track and down-track directions. Based on the temperature distribution along these directions (Fig. 5.7), the down-track gradient is calculated to be 4.8 K/nm and the cross-track gradient is calculated to be 6.9 K/nm at the 430 K contour line. A higher thermal gradient is favored; however, the optimization does not explicitly optimize the thermal gradient. Multi-objective optimization using a weighted sum of two objective functions can be carried out to simultaneously increase thermal gradient while generating uniform temperature distribution.

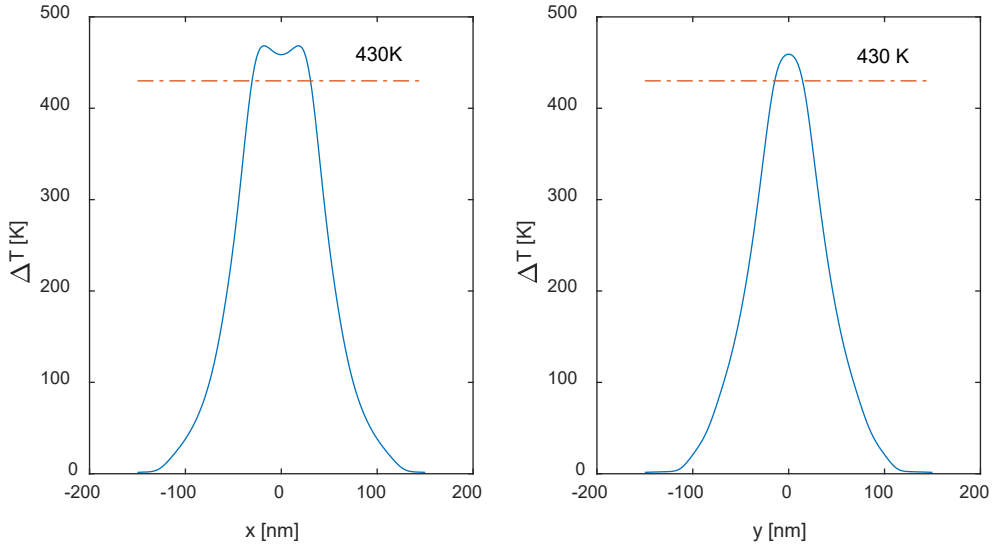

Fig. 5.7 Cross-track temperature distribution (left) and down-track temperature distribution (right) produced from the optimized absorption.

5.3.2 Electromagnetic Design

We follow the same procedures in Section 4.1 to reconstruct optical absorption patterns generated from the thermal design, with parameters listed in Table 5.2.

Table 5.2 Parameters used in optimization (HAMR).

Parameter [unit]	Value
R [Yee cell length]	2.5
β	1
k	6
α	0.01
c_r	1
c_β	1.8
N_x, N_y, N_z	101, 101, 31
S_x, S_y	151, 151

Layout for the simulation is shown below.

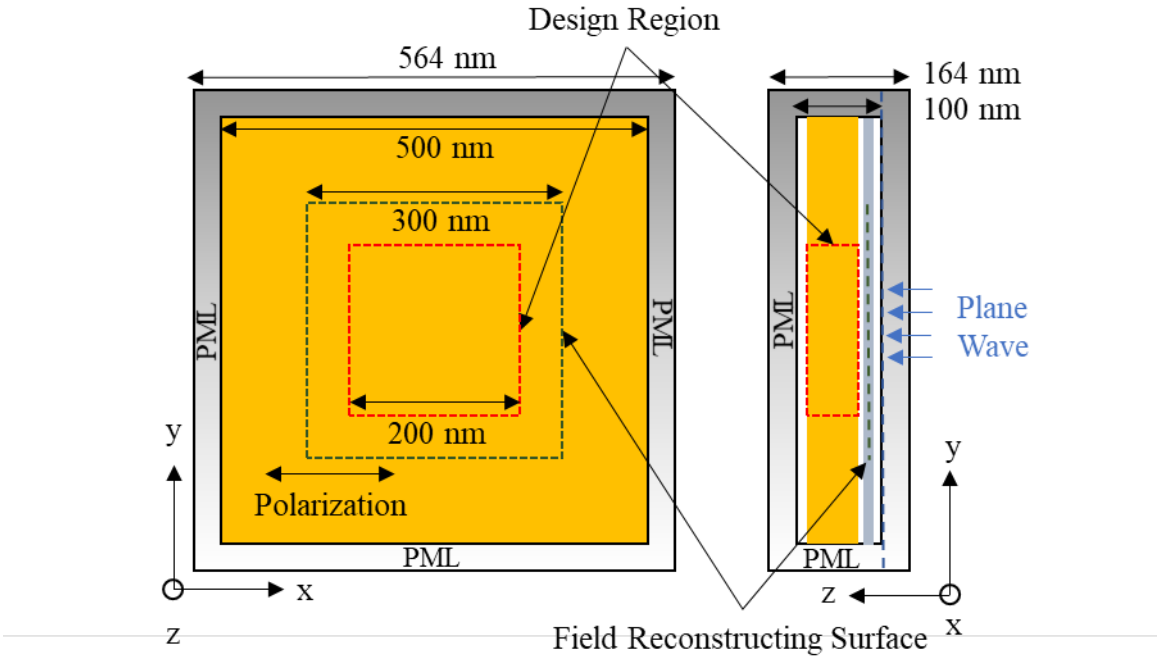

Fig. 5.8 Layout for the simulation (HAMR). All rectangles are squres with their centers alighned. Polarization of the plane wave is in x direction. The gold layer is 60 nm in thickness and the recording medium layer is 10 nm in thickness, while the field reconstructing surface is at the midplane of the recording medium.

After 60 iterations of optimization consuming ~60 hours on a 20-core server, the final design produces a maximum temperature rise of 245 K. Therefore, we increase the laser power to $P_0 = \frac{450}{245} = 1.83$ mW corresponding to a maximum temperature rise of 450 K. The final design is shown in Fig. 5.9, and the induced optical absorption and temperature are shown in Fig. 5.10.

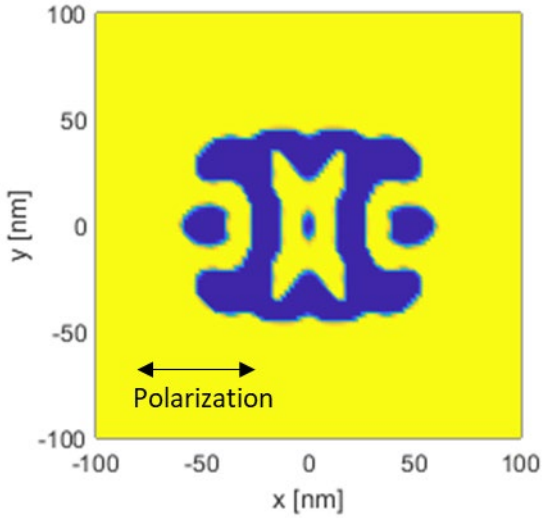

Fig. 5.9 The final design density distribution.

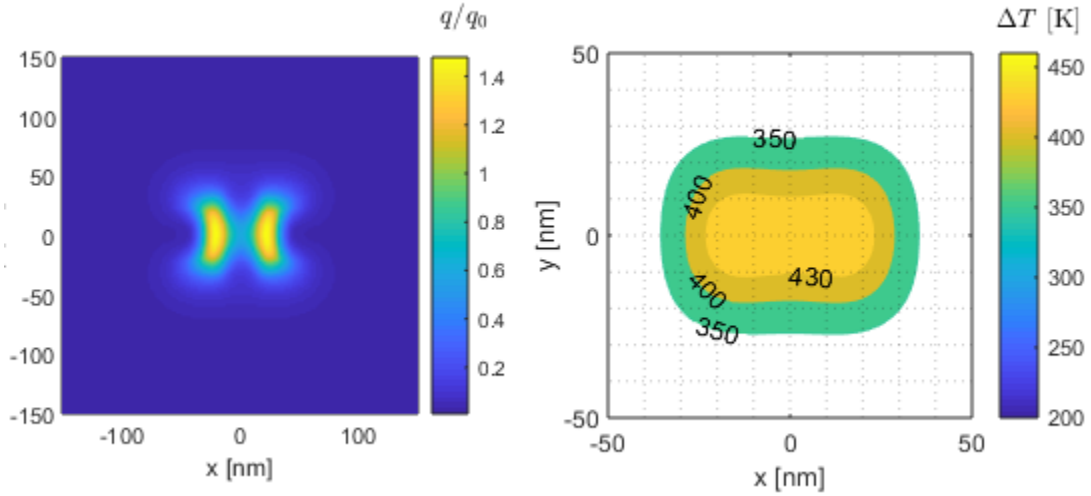

Fig. 5.10 The distribution of the absorption (left) and contours of temperature rise distribution (right) produced by the final design. The absorption is normalized by the nominal absorption q_0.

Some intermediate steps are shown in Fig. 5.11. The final design has an objective function evaluated to be 0.3. The isolated material island in the final design can cause a potential problem in self-heating of the NFT. Because it is isolated, heat can not be effectively dissipated to the surrounding, causing temperature to rise in the NFT.

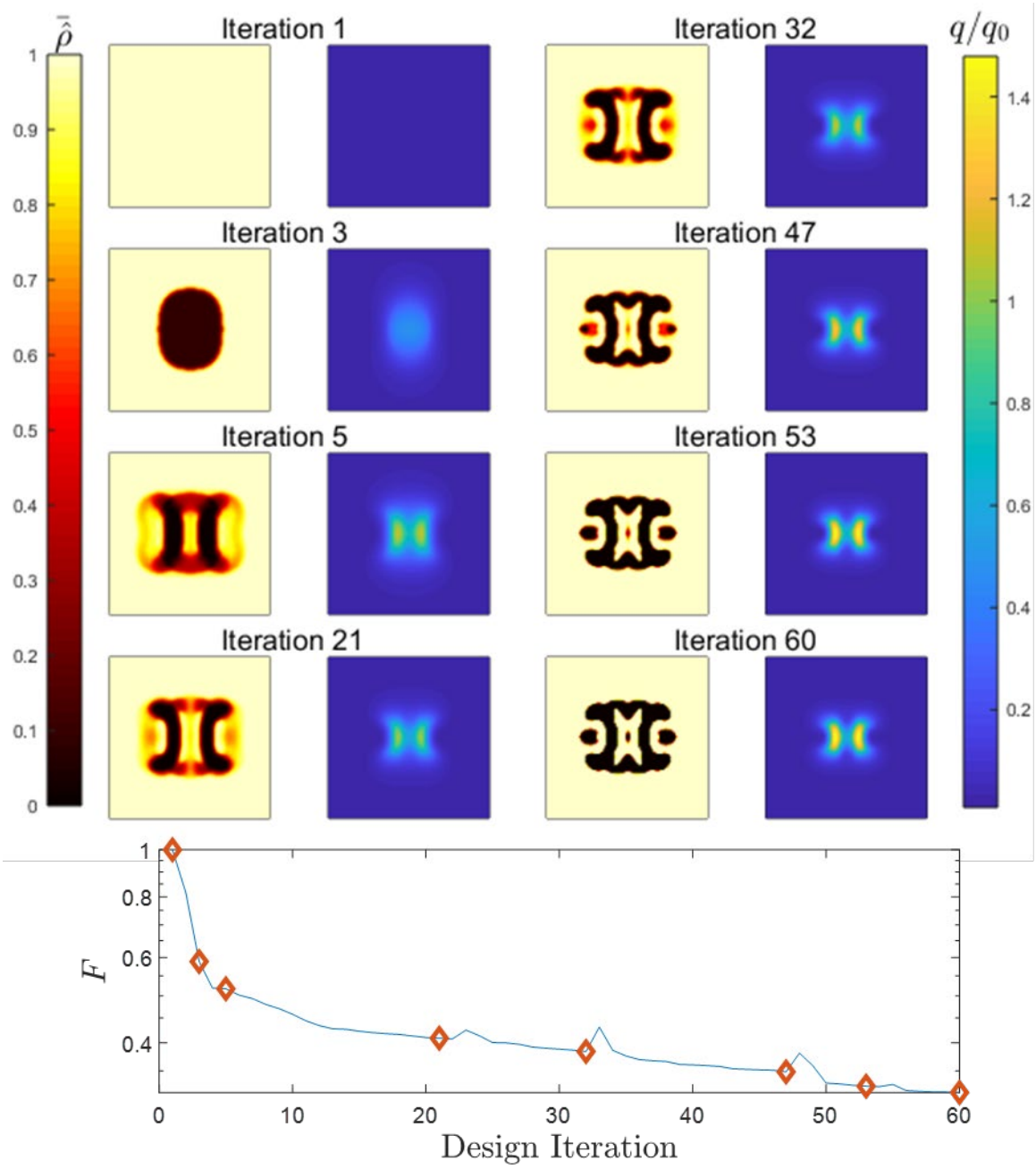

Fig. 5.11 Distributions of the projected density $\bar{\hat{\rho}}$ (left) and the normalized optical absorption (right) in some intermediate steps showing evolution of the design (HAMR). Each iteration is marked with diamond in the objective function graph at the bottom. The objective function is normalized so that it is evaluated as 1 in the 1st iteration.

It is observed that there are two hot spots with magnitudes less than that of the objectve absorption distribution in Fig. 5.6. These hot spots are created by the two protrusions via the lightning rod

effect. The 430 K contour line occupies an area of 40×20 nm^2, smaller than that of the objective temperature distribution.

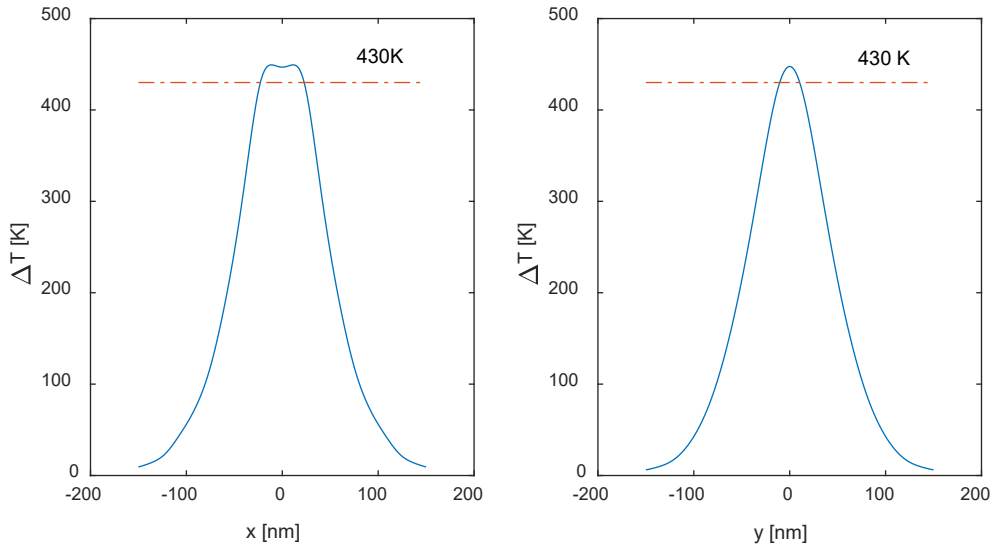

Fig. 5.12 Cross-track temperature distribution (left) and down-track temperature distribution (right) produced from the optical absorption generated by the final design.

The down-track gradient is calculated to be 3.3 K/nm and the cross-track gradient is calculated to be 4.4 K/nm at the 430 K contour line. Comparing the temperature distributions in down-track and cross-track directions in Fig. 5.12 with ones in Fig. 5.7, we observe that the cross-track profile remains slightly changed while the down-track profile has a shaper peak. The reason for this is that in the objective absorption profile there are two horizontal ridges connecting the two peaks (Fig. 5.6), while in the design absorption profile there are no ridges (Fig. 5.10). The inability of the optimization to create the two horizontal ridges in the absorption profile stems from the fact that polarization is horizontal. Plasmonic waves reside on the material interface perpendicular to the direction of polarization. Therefore, a horizontal polarization is unable to induce horizontal plasmonic waves.

5.4 Conclusion

Topology optimization is successfully implemented to design a plasmonic aperture that can generate a uniform temperature profile in one-bit volume of HAMR. Although we tackle the design

problem in two stages – thermal and electromagnetic designs – a one-stage method is possible by directly relating field magnitudes to temperature distribution. Although it may seem like the resulted design is only able to produce uniform temperature in the cross-track direction, it is less important to produce uniform temperature profile in the down-track direction because the down-track distance is much smaller.

6. SUMMARY AND FUTURE WORK

6.1 Summary

In this thesis, we present a framework for applying topology optimization in plasmonics using the FDTD method as the direct solver. In particular, detailed derivations of discrete and continuous adjoint sensitivity analysis are provided. We also present two case studies and one application to verify the robustness of the framework.

At first, we generalize the sensitivity analysis from a function analytic point of view. It is explained and demonstrated that the first and foremost challenge in applying topology optimization in plasmonics is to obtain accurate sensitivity, which is particularly compelling if the direct solver is the FDTD method. We develop a method to solve this issue based on the underlying numerical model and argue that it applies to problems with isotropic materials, uniform grid and lossless boundary conditions. Validity of the solution is tested in the two examples where the predicted gradients match the exact gradients. We believe this key improvement would enable the widespread use of topology optimization with the FDTD method. Next, we discuss general procedures to carry out topology optimization. A density approach with the FDTD method and filtering-and-projection regularizations is presented and implemented to successfully recover near field patterns of a bowtie aperture and an elongated bowtie antenna. It is pointed out that regularizations are particularly important in plasmonic structures as the objective function is highly sensitivity to material variation. At last, we carry out topology optimization on a real application involving a coupled thermal-electromagnetic system. With restricted computational power, our method successfully generates a plasmonic aperture to produce uniform temperature profile within a nano-scale volume. Although we end up writing our own FDTD solver, the simplicity of the discrete sensitivity formula we present can be easily incorporated into any existing FDTD package as long as field components can be accessed at each individual Yee cell.

6.2 Future Work

The discrete sensitivity analysis can be extended to include anisotropic materials, which broadens applications. To save time in simulations, the formula can be extended to non-uniform FDTD grid. To fully explore the capability of FDTD method, broad-band objective functions can be considered. Beside these extensions, the rough landscape of topology optimization in plasmonics may be countered by using line fitting model or Machine learning algorithms. We can apply the discrete sensitivity formula in a level-set-based method and use it as a fine-tuning stage after obtaining results from the density-based method to improve convergence. The topological derivatives introduced in Section 3.1.3 have only been derived in the continuous sense and can be extended to a discrete formula for FDTD method.

There is a lot of room for improvement in the HAMR application provided we have a higher computational power. First, we can start tuning the parameters in the optimization to get better results. The tuning can be less time consuming if we can run the optimization in a cluster of machines with hundreds of cores. Second, a more complicated objective function can be used to simultaneously optimize thermal gradient and maintain uniform temperature profile. Third, more complicated regularizations can be applied to achieve smoother and faster convergence. Fourth, general 3D NFTs can be considered provided a reasonable regularization on the manufacturability is imposed. Finally, a level-set-based optimization can be used to fine-tune the geometry to achieve an even better result.

REFERENCES

[1] J. S. Jensen and O. Sigmund, "Topology optimization for nano-photonics," *Laser and Photonics Reviews*, vol. 5, no. 2. John Wiley & Sons, Ltd, pp. 308–321, 08-Mar-2011.

[2] M. P. Bendsøe and O. Sigmund, *Topology Optimization: Theory, Methods and Applications*. Springer Berlin Heidelberg, 2003.

[3] A. Taflove and S. C. Hagness, *Computational Electrodynamics : the Finite-Difference Time-Domain Method*. Artech House, 2005.

[4] J.-M. Jin, *The Finite Element Method in Electromagnetics*. John Wiley & Sons, 2015.

[5] D. C. Dobson and S. J. Cox, "Maximizing band gaps in two-dimensional photonic crystals," *SIAM J. Appl. Math.*, vol. 59, no. 6, pp. 2108–2120, Jan. 2003.

[6] J. S. Jensen and O. Sigmund, "Systematic design of photonic crystal structures using topology optimization: Low-loss waveguide bends," *Appl. Phys. Lett.*, vol. 84, no. 12, pp. 2022–2024, Mar. 2004.

[7] H. Men, N. C. Nguyen, R. M. Freund, P. A. Parrilo, and J. Peraire, "Bandgap optimization of two-dimensional photonic crystals using semidefinite programming and subspace methods," *J. Comput. Phys.*, vol. 229, no. 10, pp. 3706–3725, 2010.

[8] Y. Elesin, B. S. Lazarov, J. S. Jensen, and O. Sigmund, "Time domain topology optimization of 3D nanophotonic devices," *Photonics Nanostructures - Fundam. Appl.*, vol. 12, no. 1, pp. 23–33, 2014.

[9] N. K. Nikolova, H. W. Tam, and M. H. Bakr, "Sensitivity analysis with the FDTD method on structured grids," *IEEE Trans. Microw. Theory Tech.*, vol. 52, no. 4, pp. 1207–1216, 2004.

[10] S. Schäffler, *Global Optimization*, vol. 350. Springer, 2012.

[11] M. M. Spühler, B. J. Offrein, G. L. Bona, R. Germann, I. Massarek, and D. Erni, "A very short planar silica spot-size converter using a nonperiodic segmented waveguide," *J. Light. Technol.*, vol. 16, no. 9, pp. 1680–1685, 1998.

[12] S. Boyd and L. Vandenberghe, *Convex Optimization*. Cambridge university press, 2004.

[13] V. Ganapati, O. D. Miller, and E. Yablonovitch, "Light trapping textures designed by electromagnetic optimization for subwavelength thick solar cells," *IEEE J. Photovoltaics*, vol. 4, no. 1, pp. 175–182, 2013.

[14] S. Bhargava and E. Yablonovitch, "Lowering HAMR near-field transducer temperature via inverse electromagnetic design," *IEEE Trans. Magn.*, vol. 51, no. 4, 2015.

[15] M. A. Swillam, M. H. Bakr, N. K. Nikolova, and X. Li, "Adjoint sensitivity analysis of dielectric discontinuities using FDTD," *Electromagnetics*, vol. 27, no. 2–3, pp. 123–140, Mar. 2007.

[16] D. E. Kirk, *Optimal Control Theory: An Introduction*. Courier Corporation, 2012.

[17] O. Sigmund and K. Maute, "Topology optimization approaches: A comparative review," *Structural and Multidisciplinary Optimization*, vol. 48, no. 6. Springer Berlin Heidelberg, pp. 1031–1055, 21-Dec-2013.

[18] D. Dyck, D. A. Lowther, and E. M. Freeman, "A method of computing the sensitivity of electromagnetic quantities to changes in materials and sources," *IEEE Trans. Magn.*, vol. 30, no. 5, pp. 3415–3418, 2002.

[19] J. Andkjær and O. Sigmund, "Topology optimized low-contrast all-dielectric optical cloak," *Appl. Phys. Lett.*, vol. 98, no. 2, p. 021112, Jan. 2011.

[20] J. Andkjr, N. Asger Mortensen, and O. Sigmund, "Towards all-dielectric, polarization-independent optical cloaks," *Appl. Phys. Lett.*, vol. 100, no. 10, p. 101106, Mar. 2012.

[21] G. Fujii, H. Watanabe, T. Yamada, T. Ueta, and M. Mizuno, "Level set based topology optimization for optical cloaks," *Appl. Phys. Lett.*, vol. 102, no. 25, p. 251106, Jun. 2013.

[22] P. Hansen and L. Hesselink, "Accurate adjoint design sensitivities for nano metal optics," *Opt. Express*, vol. 23, no. 18, p. 23899, Sep. 2015.

[23] S. Bhargava, O. Miller, V. Ganapati, and E. Yablonovitch, "Inverse design of optical antennas for sub-wavelength energy delivery," 2013, p. CM2F.2.

[24] O. S. Ahmed, M. H. Bakr, X. Li, and T. Nomura, "Adjoint variable method for two-dimensional plasmonic structures," *Opt. Lett.*, vol. 37, no. 16, p. 3453, Aug. 2012.

[25] Y. Zhang, O. S. Ahmed, and M. H. Bakr, "Adjoint sensitivity analysis of plasmonic structures using the FDTD method," *Opt. Lett.*, vol. 39, no. 10, p. 3002, 2014.

[26] A. V Oppenheim, *Discrete-Time Signal Processing*. Pearson Education India, 1999.

[27] N. P. Van Dijk, K. Maute, M. Langelaar, and F. Van Keulen, "Level-set methods for structural topology optimization: A review," *Structural and Multidisciplinary Optimization*, vol. 48, no. 3. pp. 437–472, 2013.

[28] F. De Gournay, F. Jouve, A.-M. Toader, G. Allaire, and F. De Gournay, "Structural optimization using topological and shape sensitivity via a level set method," *Control Cybern.*, vol. 34, no. 1, p. 59, 2005.

[29] S. Zhou, W. Li, and Q. Li, "Level-set based topology optimization for electromagnetic dipole antenna design," *J. Comput. Phys.*, vol. 229, no. 19, pp. 6915–6930, Sep. 2010.

[30] S. Osher and J. Sethian, "Fronts propagating with curvature-dependent speed: algorithms based on Hamilton-Jacobi formulations," *J. Comput. Phys.*, vol. 79, no. 1988, pp. 12–49, 1988.

[31] S. Molesky, Z. Lin, A. Y. Piggott, W. Jin, J. Vucković, and A. W. Rodriguez, "Inverse design in nanophotonics," *Nature Photonics*, vol. 12, no. 11. Nature Publishing Group, pp. 659–670, 26-Nov-2018.

[32] C. Forestiere, Y. He, R. Wang, R. M. Kirby, and L. Dal Negro, "Inverse design of metal nanoparticles' morphology," *ACS Photonics*, vol. 3, no. 1, pp. 68–78, Jan. 2016.

[33] B. S. Lazarov, F. Wang, and O. Sigmund, "Length scale and manufacturability in density-based topology optimization," *Arch. Appl. Mech.*, vol. 86, no. 1–2, pp. 189–218, Jan. 2016.

[34] G. Allaire, F. Jouve, and A. M. Toader, "Structural optimization using sensitivity analysis and a level-set method," *J. Comput. Phys.*, vol. 194, no. 1, pp. 363–393, Feb. 2004.

[35] T. E. Bruns and D. A. Tortorelli, "Topology optimization of non-linear elastic structures and compliant mechanisms," *Comput. Methods Appl. Mech. Eng.*, vol. 190, no. 26–27, pp. 3443–3459, Mar. 2001.

[36] O. Sigmund, "Morphology-based black and white filters for topology optimization," *Struct. Multidiscip. Optim.*, vol. 33, no. 4–5, pp. 401–424, Feb. 2007.

[37] T. Borrvall and J. Petersson, "Topology optimization using regularized intermediate density control," *Comput. Methods Appl. Mech. Eng.*, vol. 190, no. 37–38, pp. 4911–4928, Jun. 2001.

[38] R. E. Christiansen, B. S. Lazarov, J. S. Jensen, and O. Sigmund, "Creating geometrically robust designs for highly sensitive problems using topology optimization: Acoustic cavity design," *Struct. Multidiscip. Optim.*, vol. 52, no. 4, pp. 737–754, Oct. 2015.

[39] R. E. Christiansen, J. Vester-Petersen, S. P. Madsen, and O. Sigmund, "A non-linear material interpolation for design of metallic nano-particles using topology optimization," *Comput. Methods Appl. Mech. Eng.*, vol. 343, pp. 23–39, 2019.

[40] E. Jones, T. Oliphant, P. Peterson, and others, "SciPy: Open Source Scientific Tools for Python." [Online]. Available: http://www.scipy.org/.

[41] K. Svanberg, "The method of moving asymptotes—a new method for structural optimization," *Int. J. Numer. Methods Eng.*, vol. 24, no. 2, pp. 359–373, Feb. 1987.

[42] S. G. Johnson, "The NLopt nonlinear-optimization package." [Online]. Available: http://github.com/stevengj/nlopt.

[43] R. H. Byrd, P. Lu, J. Nocedal, and C. Zhu, "A limited memory algorithm for bound constrained optimization," *SIAM J. Sci. Comput.*, vol. 16, no. 5, pp. 1190–1208, Sep. 2005.

[44] W. Rudin, *Functional Analysis*. McGraw-Hill, 1991.

[45] C. Altman and K. Suchy, *Reciprocity, Spatial Mapping and Time Reversal in Electromagnetics*. Dordrecht: Springer Science & Business Media, 2011.

[46] J. B. Conway, *A Course in Functional Analysis*, vol. 96. Springer Science & Business Media, 2013.

[47] K. M. Chen, "A mathematical formulation of the equivalence principle," *IEEE Trans. Microw. Theory Tech.*, vol. 37, no. 10, pp. 1576–1581, 1989.

[48] D. Sarkar and N. J. Halas, "General vector basis function solution of Maxwell's equations," *Phys. Rev. E - Stat. Physics, Plasmas, Fluids, Relat. Interdiscip. Top.*, vol. 56, no. 1, pp. 1102–1112, Jul. 1997.

[49] R. L. Wheeden, *Measure and Integral: An introduction to Real Analysis*, Second. Chapman and Hall/CRC, 2015.

[50] O. D. Miller, "Photonic design: from fundamental solar cell physics to computational inverse design," University of California at Berkeley, 2013.

[51] J. D. Jackson, *Classical Electrodynamics*. AAPT, 1999.

[52] E. Zeidler, *Nonlinear Functional Analysis and its Applications -- III: Variational Methods and Optimization*. Springer Science & Business Media, 1985.

[53] S. Garreau, P. Guillaume, and M. Masmoudi, "The topological asymptotic for PDE systems: the elasticity case," *SIAM J. Control Optim.*, vol. 39, no. 6, pp. 1756–1778, 2003.

[54] A. C. Lesina, A. Vaccari, P. Berini, and L. Ramunno, "On the convergence and accuracy of the FDTD method for nanoplasmonics," *Opt. Express*, vol. 23, no. 8, p. 10481, 2015.

[55] A. Taflove, "Application of the finite-difference time-domain method to sinusoidal steady-state electromagnetic-penetration problems," *IEEE Trans. Electromagn. Compat.*, vol. EMC-22, no. 3, pp. 191–202, 1980.

[56] Kane Yee, "Numerical solution of initial boundary value problems involving maxwell's equations in isotropic media," *IEEE Trans. Antennas Propag.*, vol. 14, no. 3, pp. 302–307, 2004.

[57] M. A. Alsunaidi, "A general ADE-FDTD algorithm for the simulation of different dispersive materials," *Electromagnetics*, no. 6, pp. 278–281, 2009.

[58] B. Bradie, *A Friendly Introduction to Numerical Analysis*. Pearson Education India, 2006.

[59] A. F. Oskooi, D. Roundy, M. Ibanescu, P. Bermel, J. D. Joannopoulos, and S. G. Johnson, "Meep: A flexible free-software package for electromagnetic simulations by the FDTD method," *Comput. Phys. Commun.*, vol. 181, no. 3, pp. 687–702, Mar. 2010.

[60] M. Burger, "A framework for the construction of level set methods for shape optimization and reconstruction," *Interfaces Free boundaries*, vol. 5, no. 3, pp. 301–329, 2003.

[61] A. D. Rakic, A. B. Djurisic, J. M. Elazar, and M. L. Majewski, "Optical properties of metallic films for vertical-cavity optoelectronic devices.," *Appl. Opt.*, vol. 37, no. 22, pp. 5271–83, 1998.

[62] P. Hansen, "Adjoint sensitivity analysis for nanophotonic structures," Stanford University, 2014.

[63] Y. Deng *et al.*, "Topology optimization of metal nanostructures for localized surface plasmon resonances," *Struct. Multidiscip. Optim.*, vol. 53, no. 5, pp. 967–972, May 2016.

[64] E. Wadbro and C. Engström, "Topology and shape optimization of plasmonic nano-antennas," *Comput. Methods Appl. Mech. Eng.*, vol. 293, pp. 155–169, 2015.

[65] Yan Zhao, C. Argyropoulos, and Yang Hao, "Full-wave finite-difference time-domain simulation of electromagnetic cloaking structures," *Opt. Express*, vol. 16, no. 9, pp. 6717–6730, 2008.

[66] M. Y. Wang, X. Wang, and D. Guo, "A level set method for structural topology optimization," *Comput. Methods Appl. Mech. Eng.*, vol. 192, no. 1–2, pp. 227–246, Jan. 2003.

[67] M. J. De Ruiter and F. Van Keulen, "Topology optimization using a topology description function," *Struct. Multidiscip. Optim.*, vol. 26, no. 6, pp. 406–416, Apr. 2004.

[68] L. Van Miegroet and P. Duysinx, "Stress concentration minimization of 2D filets using X-FEM and level set description," *Struct. Multidiscip. Optim.*, vol. 33, no. 4–5, pp. 425–438, Feb. 2007.

[69] F. Santosa, "A level-set approach for inverse problems involving obstacles," *ESAIM Control. Optim. Calc. Var.*, vol. 1, pp. 17–33, 1996.

[70] L. Hörmander, *The Analysis of Linear Partial Differential Operators I: Distribution Theory and Fourier analysis*. Springer, 2015.

[71] H. A. Eschenauer, V. V Kobelev, and A. Schumacher, "Bubble method for topology and shape optimization of structures," *Struct. Optim.*, vol. 8, no. 1, pp. 42–51, 1994.

[72] Y. Deng, Z. Liu, C. Song, J. Wu, Y. Liu, and Y. Wu, "Topology optimization-based computational design methodology for surface plasmon polaritons," *Plasmonics*, vol. 10, no. 3, pp. 569–583, Jun. 2015.

[73] T. E. Bruns and D. A. Tortorelli, "An element removal and reintroduction strategy for the topology optimization of structures and compliant mechanisms," *Int. J. Numer. Methods Eng.*, vol. 57, no. 10, pp. 1413–1430, Jul. 2003.

[74] F. Wang, B. S. Lazarov, and O. Sigmund, "On projection methods, convergence and robust formulations in topology optimization," *Struct. Multidiscip. Optim.*, vol. 43, no. 6, pp. 767–784, Jun. 2011.

[75] X. Wen, A. Datta, L. M. Traverso, L. Pan, X. Xu, and E. E. Moon, "High throughput optical lithography by scanning a massive array of bowtie aperture antennas at near-field," *Sci. Rep.*, vol. 5, no. 1, p. 16192, Dec. 2015.

[76] E. Betzig *et al.*, "Near-field magneto-optics and high density data storage," *Appl. Phys. Lett.*, vol. 61, no. 2, pp. 142–144, Jul. 1992.

[77] N. Zhou, E. C. Kinzel, and X. Xu, "Nanoscale ridge aperture as near-field transducer for heat-assisted magnetic recording," *Appl. Opt.*, vol. 50, no. 31, p. G42, 2011.

[78] R. E. Rottmayer *et al.*, "Heat assisted magnetic recording," *IEEE Trans. Magn.*, vol. 42, no. 10, pp. 2417–2421, Nov. 2006.

[79] A. Q. Wu *et al.*, "HAMR areal density demonstration of 1+ tbpsi on spinstand," *IEEE Trans. Magn.*, vol. 49, no. 2, pp. 779–782, Feb. 2013.

[80] W. A. Challener *et al.*, "Heat-assisted magnetic recording by a near-field transducer with efficient optical energy transfer," *Nat. Photonics*, vol. 3, no. 4, pp. 220–224, 2009.

[81] A. Datta and X. Xu, "Comparative study of optical near-field transducers for heat-assisted magnetic recording," *Opt. Eng.*, vol. 56, no. 12, p. 121906, 2017.

[82] N. Zhou *et al.*, "Plasmonic near-field transducer for heat-assisted magnetic recording," *Nanophotonics*, vol. 3, no. 3, pp. 141–155, Jan. 2014.

[83] Z. H. Cen *et al.*, "Optical property study of FePt-C nanocomposite thin film for heat-assisted magnetic recording," *Opt. Express*, vol. 21, no. 8, p. 9906, Apr. 2013.

[84] A. Datta and X. Xu, "Infrared near-field transducer for heat-assisted magnetic recording," *IEEE Trans. Magn.*, vol. 53, no. 12, pp. 1–5, Dec. 2017.

[85] S. Bhargava, "Heat-assisted magnetic recording : fundamental limits to inverse electromagnetic design," University of California, Berkeley, 2015.